THÈSE

En vue de l'obtention du

DOCTORAT DE L'UNIVERSITÉ DE TOULOUSE

Délivré par : *l'Université Toulouse 3 Paul Sabatier (UT3 Paul Sabatier)*

Présentée et soutenue le *21/10/2016* **par :**

ZHOUYE CHEN

Reconstruction of enhanced Ultrasound images from compressed measurements

JURY

FRANÇOISE PEYRIN	Directeur de recherche	Rapporteur
LAURENT SARRY	Professeur d'Université	Rapporteur
MIREILLE GARREAU	Professeur d'Université	Examinateur
JEAN-YVES TOURNERET	Professeur d'Université	Examinateur
DENIS KOUAMÉ	Professeur d'Université	Directeur de Thèse
ADRIAN BASARAB	Maître de Conférences	Co-Directeur de Thèse

École doctorale et spécialité :
MITT : Signal, Image, Acoustique et Optimisation
Unité de Recherche :
Institut de Recherche en Informatique de Toulouse (UMR CNRS 5505)
Directeur(s) de Thèse :
Denis KOUAMÉ et *Adrian BASARAB*
Rapporteurs :
Françoise PEYRIN et *Laurent SARRY*

To Yu and my parents

Acknowledgments

I would like to express my sincere gratitude to my supervisors professor Denis Kouamé and Adrian Basarab. This thesis would not be possible without your guidance, mentoring and encouragement.

I would like to thank professor Denis Kouamé. Thank you for bringing me to the wonderful world of ultrasound imaging. Your patience has helped to establish my confidence, and your rigorous scientific attitude has had a tremendous impact both on this work and on my professional development. Thank you also for supporting me to attend several conferences which have helped a lot for my research.

I would like also to express my special appreciation and thanks to my co-supervisor Adrian Basarab. You are always patient to answer me any question, no matter it is about ultrasound imaging or optimization, bringing me fruitful ideas. Thanks a lot for your every detailed modification to my every paper, which has not only helped to improve my writing skills, but also accelerated my work progress. You advice on my career have also been priceless for me.

I would like to thank to China Scholarship Council (CSC) for supporting the research during my PhD at University of Toulouse. I would like also to give many thanks to my thesis committee members: professor Mireille Garreau, professor Laurent Sarry, professor Françoise Peyrin and professor Jean-Yves Tourneret, for serving as my committee members. Thanks a lot for your insightful comments and encouragement about my work.

My sincere thanks also go to professor Rafael Molina and Leonidas Spinoulas for sharing the codes of their work, without which my first journal paper would not be completed. I would like to thank Creatis lab at Lyon, who has provided me the chance to acquire real data from their ultrasound scanner. I would like to thank professor Alin Achim as well, thank you for your powerful recommendation letter both in English and French. I would like also to give my thanks to professor Yves Wiaux, thank you for offering me the opportunity to give a visit to the BASP group, where I have seen very brilliant and excellent colleagues.

I would like to thank other professors in our TCI group at IRIT, including Alain Crouzil, Christophe Collet and Lotfi Chaari. I would like also to give my sincere thanks to my dear colleagues, Teodora, Rose, Ningning, Thanh, Rémi, Qi, Bérengére, Arturo and Sarah for all your kind help and being accompanied during the last three years. Besides, I would give my great thanks to Chantal Morand for her help with all the

French visa documents. Thanks again to all my friends at office 211 and 213.

I would like to thank all my Chinese friends at UPS as well. I would not forget the road we walked together, the dinner we cooked together and the discussion we had together, all of which have left me precious memory.

None of this would have been possible without the support from my family. A special thanks is given to my mother, father, mother-in-law and father-in-law. Thanks for your emotional support for my every decision. Finally, I would like to thank my husband, Yu. Thank you for your boundless love, unending patience and warm encouragement. I cannot accomplish this without you.

Abstract

The interest of compressive sampling in ultrasound imaging has been recently extensively evaluated by several research teams. Following the different application setups, it has been shown that the RF data may be reconstructed from a small number of measurements and/or using a reduced number of ultrasound pulse emissions. According to the model of compressive sampling, the resolution of reconstructed ultrasound images from compressed measurements mainly depends on three aspects: the acquisition setup, *i.e.* the incoherence of the sampling matrix, the image regularization, *i.e.* the sparsity prior, and the optimization technique. We mainly focused on the last two aspects in this thesis. Nevertheless, RF image spatial resolution, contrast and signal to noise ratio are affected by the limited bandwidth of the imaging transducer and the physical phenomenon related to Ultrasound wave propagation. To overcome these limitations, several deconvolution-based image processing techniques have been proposed to enhance the ultrasound images.

In this thesis, we first propose a novel framework for Ultrasound imaging, named compressive deconvolution, to combine the compressive sampling and deconvolution. Exploiting an unified formulation of the direct acquisition model, combining random projections and 2D convolution with a spatially invariant point spread function, the benefit of this framework is the joint data volume reduction and image quality improvement.

An optimization method based on the Alternating Direction Method of Multipliers is then proposed to invert the linear model, including two regularization terms expressing the sparsity of the RF images in a given basis and the generalized Gaussian statistical assumption on tissue reflectivity functions. It is improved afterwards by the method based on the Simultaneous Direction Method of Multipliers. Both algorithms are evaluated on simulated and *in vivo* data.

With regularization techniques, a novel approach based on Alternating Minimization is finally developed to jointly estimate the tissue reflectivity function and the point spread function. A preliminary investigation is made on simulated data.

Keywords – Ultrasound imaging, signal and image processing, resolution enhancement, inverse problems, compressive sampling, deconvolution, optimization, alternating direction method of multipliers, simultaneous direction method of multipliers.

Résumé

L'intérêt de l'échantillonnage compressé dans l'imagerie ultrasonore a été récemment évalué largement par plusieurs équipes de recherche. Suite aux différentes configurations d'application, il a été démontré que les données RF peuvent être reconstituées à partir d'un faible nombre de mesures et / ou en utilisant un nombre réduit d'émission d'impulsions ultrasonores. Selon le modèle de l'échantillonnage compressé, la résolution des images ultrasonores reconstruites à partir des mesures compressées dépend principalement de trois aspects: la configuration d'acquisition, c.à.d. l'incohérence de la matrice d'échantillonnage, la régularisation de l'image, c.à.d. l'a priori de parcimonie et la technique d'optimisation. Nous nous sommes concentrés principalement sur les deux derniers aspects dans cette thèse. Néanmoins, la résolution spatiale d'image RF, le contraste et le rapport signal sur bruit dépendent de la bande passante limitée du transducteur d'imagerie et du phénomène physique lié à la propagation des ondes ultrasonores. Pour surmonter ces limitations, plusieurs techniques de traitement d'image en fonction de déconvolution ont été proposées pour améliorer les images ultrasonores.

Dans cette thèse, nous proposons d'abord un nouveau cadre de travail pour l'imagerie ultrasonore, nommé déconvolution compressée, pour combiner l'échantillonnage compressé et la déconvolution. Exploitant une formulation unifiée du modèle d'acquisition directe, combinant des projections aléatoires et une convolution 2D avec une réponse impulsionnelle spatialement invariante, l'avantage de ce cadre de travail est la réduction du volume de données et l'amélioration de la qualité de l'image.

Une méthode d'optimisation basée sur l'algorithme des directions alternées est ensuite proposée pour inverser le modèle linéaire, en incluant deux termes de régularisation exprimant la parcimonie des images RF dans une base donnée et l'hypothèse statistique gaussienne généralisée sur les fonctions de réflectivité des tissus. Nous améliorons les résultats ensuite par la méthode basée sur l'algorithme des directions simultanées. Les deux algorithmes sont évalués sur des données simulées et des données in vivo.

Avec les techniques de régularisation, une nouvelle approche basée sur la minimisation alternée est finalement développée pour estimer conjointement les fonctions de réflectivité des tissus et la réponse impulsionnelle. Une investigation préliminaire est effectuée sur des données simulées.

Mots-clés – Imagerie ultrasonore, traitement du signal et de l'image, amélioration de la résolution, problèmes inverses, l'échantillonnage compressé, déconvolution, optimi-

sation, l’algorithme des directions alternées, l’algorithme des directions simultanées.

Contents

Chapter 1

Ultrasound Medical imaging

Contents

The first chapter is devoted to introducing ultrasound imaging, its place in the major medical imaging modalities as well as its specific characteristics, strengths and weaknesses. After explaining the physics of ultrasound, including the generation and the propagation of ultrasound waves, the formation of the ultrasound images will be detailed. Inherent limitations directly related to the characteristics of ultrasound and different imaging modes or acquisitions will be also discussed in this introduction. Finally, we will present the main current issues related to this modality.

1.1 Why ultrasound imaging?

Ultrasound (US), usually referring to the sound waves with frequencies higher than $20,000$ Hz which is the upper audible limit of human hearing, is one of the most widely used imaging technologies in medicine.

Since 1942, when the Austrian neurologist Karl Theo Dussik first applied ultrasound as a medical diagnostic tool to image the brain, ultrasound has been used to image the human body for over half a century [Edler 2004]. Medical doctors today use it to view the heart, blood vessels, kidneys, liver and other organs.

Compared with other imaging modalities, such as magnetic resonance imaging (MRI) and computed tomography (CT) (see Table 1.1), the US imaging has the advantage of being noninvasive, free of radiation risk, portable and relatively inexpensive. Furthermore, since US images are captured in real-time, they can also show the structure and movement of the body's internal organs, as well as blood flowing through blood vessels, thus providing instantaneous visual guidance for many interventional procedures including those for regional anesthesia and pain management [Chan 2011].

Table 1.1: Comparison of imaging modalities [Szabo 2004, p. 23].

Modality	Ultrasound	X-ray	CT	MRI
Physical agent	Ultrasound	X-ray	X-ray	Magnetic field
Principle	Mechanical properties	Mean tissue absorption	Tissue absorption	Biochemistry
Spatial resolution	frequency and axially dependent 0.3-3 mm	∼1 mm	∼1 mm	∼1 mm
Penetration	frequency dependent 3-25cm	Excellent	Excellent	Excellent
Safety	Very good	Ionizing radiation	Ionizing radiation	Very good
Cost	$	$	$$$$	$$$$$$$$
Portability	Excellent	Good	Poor	Poor
Speed	$\leq$ 10 ms	∼1 min	$\geq$1 min	$\leq$ 0.1 s

However, from the table above, we may also remark that US imaging has the disadvantage of spatial resolution (which is related to US frequencies) and penetration, two important challenges addressed in the literature. Before deeply presenting the details of the work realized in this PhD, we will first remind the most common features of ultrasound imaging systems.

1.2 Physics of Ultrasound

US images are created based on the physical interaction between an emitted acoustic wave and the human tissues. To form an US image, sound waves need to be produced, received and interpreted. Let us denote the frequency of the US wave by f, and the corresponding wavelength by λ. The range of f in medical ultrasound imaging is 2 to 60 MHz, and even more in some specific applications such as acoustic microscopy.

1.2.1 The Piezoelectrical transducer

US waves are typically produced by a transducer which is composed of a certain number of piezoelectric elements (Fig. 1.1). The piezoelectric element is an essential part of the transducer able to generate and receive the US waves. According to the Piezoelectric phenomena: a voltage is applied on the two sides of a piezoelectric crystal, the piezoelectric crystal will oscillate by repeatedly expanding and contracting, generating a sound wave, which is also called the "direct piezoelectric effect". In contrast, the "indirect piezoelectric effect" will happen: when the element is externally excited by a vibration (or an ultrasonic wave), it generates a voltage. Thus, the conversion between the electrical energy and the acoustic energy is completed by transmitting and receiving the US waves. This phenomenon is illustrated in Fig. 1.2.

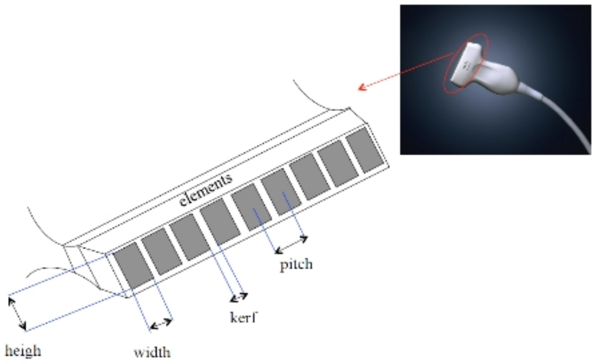

Figure 1.1: Transducer and elements [Kouamé 2015].

An US transducer can contain one or several piezoelectric elements. However, the transducer composed by a single element will usually require mechanical scanning to form an US image. Most current sensors use multi-element arrays (rectangular or annular) allowing electronic scanning (see section 1.3.2). Typically, a rectangular bar is composed

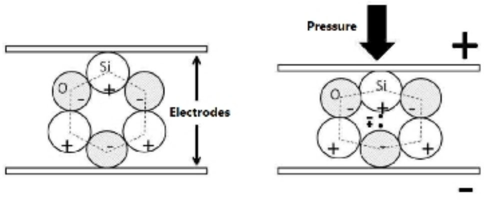

Figure 1.2: Direct and indirect piezoelectric effects [Kouamé 2015].

by 50 to 100 elements for a total of 1 cm (height of each element) to 3 cm. The width of each element is approximately a quarter of the wavelength, *i.e.*, standardly between 0.2 and 0.75 mm.

1.2.2 Wave propagation

US wave brings the information of an object to the imaging system, and provides information at the same time on the nature of the medium it crossed. In general cases, the study of its propagation and its interaction with various elements encountered is relatively complex. Three assumptions are usually used to simplify the analytical derivations. Firstly, we will assimilate the human body to a non-elastic liquid medium in which the US waves propagate. The proportion of water in the human body helps to legitimize this hypothesis and to perform many experimental measurements in water-filled tanks. The second assumption is that the waves obey the principle of linearity. However, we should keep in mind that although this assumption holds, in many imaging context the interaction between the wave and the tissues can be highly nonlinear: it is also the basis for harmonic imaging, a major current technique for improving US image quality. Finally, we will consider here that the support materials for propagation are lossless. This assumption is obviously wrong and will be corrected later.

To establish propagation equations, an US longitudinal wave is considered moving in a homogeneous medium. We should note that, when the particles move forth and back in the same direction as the US wave is travelling, the US wave is called a longitudinal wave. In medical ultrasound, waves mostly propagate in soft tissues. At time t, a particle belonging to the medium located at position (x, y, z) moves forth and back along the axis of propagation z, and thus depends on (x, y, z, t). The movement speed $v(x, y, z, t)$ can then be obtained by differentiating the displacement with respect to time in the ideal incompressible fluid. Similarly, these disturbances generate a local acoustic pressure $p(x, y, z, t)$ and in these conditions, in a homogeneous medium the propagation equation of US waves can be written as

$$\nabla^2 p = \frac{1}{c^2}\frac{\partial^2 p}{\partial t^2} \tag{1.1}$$

where ∇^2 is the Laplacian operator defined as

$$\nabla^2 = \frac{\partial^2}{\partial x^2} + \frac{\partial^2}{\partial y^2} + \frac{\partial^2}{\partial z^2}. \tag{1.2}$$

The wave equation is sometimes involving the Alembertian operator $\Box = \frac{1}{c^2}\frac{\partial^2}{\partial t^2} - \nabla^2$ turning into

$$\Box p = 0. \tag{1.3}$$

The propagation waves come from the solution to (1.2) or (1.3). Although, the analytical solution cannot be easily obtained in the general case, it can be written in a more direct manner depending on the geometry of the wave. Under the assumptions (near or far field, focal area or not), the wave will be considered as a plane or a spherical one. The corresponding wavefronts, that is to say the phase surfaces during propagation, are illustrated in Fig. 1.3.

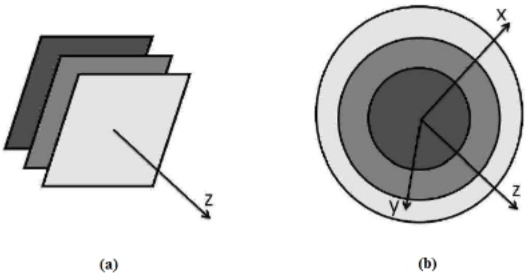

Figure 1.3: (a)Plane Wave, (b)Spherical Wave [Morin 2013a].

Plane Wave

The geometry of a plane wave is the simplest of all: the wave surface is plane and the changes over time in only one spatial direction which is the propagation axis. For example, if $p(x, y, z, t)$ is constant for any x and y for a given z, then $p(x, y, z, t) = p(z, t)$ propagates along z-direction and (1.1) becomes an one dimensional wave equation as

$$\frac{\partial^2 p}{\partial z^2} = \frac{1}{c^2}\frac{\partial^2 p}{\partial t^2} \tag{1.4}$$

Its general solution can be written as

$$p(z, t) = p_+(t - \frac{z}{c}) + p_-(t + \frac{z}{c}). \tag{1.5}$$

Therefore, there are two components in the wave, the forward travelling wave $p_+(z, t)$ propagating toward positive z and the backward travelling wave $p_-(z, t)$ evolving towards negative z.

Spherical Wave

In an isotropic material, a spherical wave can be generated by a small, local disturbance in the pressure. A spherical wave depends only on time and the radius $r = \sqrt{x^2 + y^2 + z^2}$. In this case, the pressure travelling in the radial direction can be shown to verify

$$\frac{1}{r}\frac{\partial^2}{\partial r^2}(rp) = \frac{1}{c^2}\frac{\partial^2 p}{\partial t^2} \tag{1.6}$$

The general solution to this spherical wave equation can be written as

$$p(r,t) = \frac{1}{r}p_+(t - \frac{r}{c}) + \frac{1}{r}p_-(t + \frac{r}{c}) \tag{1.7}$$

Similar to (1.5), there are also two components. $p_+(r,t)$ represents the outward travelling wave propagating toward outward direction and $p_+(r,t)$ represents the inward travelling wave evolving towards inward direction. We observe that the structure is similar to the one of plane wave equation, except for the factor $\frac{1}{r}$ which cause spherical wave to lose amplitude as it propagates radially outward. This is due to the conservation of the total energy and the increased surface of the wave edges as one moves away from the source.

1.2.3 Reflection/Transmission at interfaces

The spread of US waves and their behavior at the interfaces between two different acoustic environments may be considered as reflection and transmission in the context of geometrical optics.

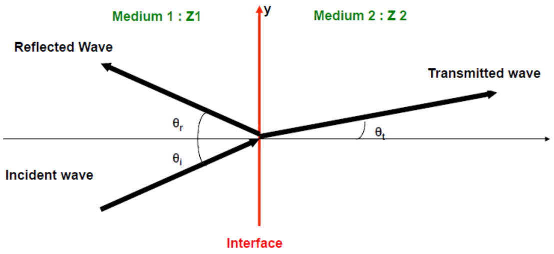

Figure 1.4: Illustration of Descartes law for the optical geometry [Kouamé 2015].

According to the geometrical optics shown in Fig. 1.4, when an US wave (incident wave in the figure) meets the interface between two mediums of different mechanical properties, *i.e.* the speed of sound (see Table 1.2), part of the energy will be transmitted into the second medium while part of it will be reflected as an echo. For the transmission of US waves, the big difference between the two mediums will produce a great energy loss. From the Table 1.2, we may consider that in most biological tissues, the speed of sound is approximately 1500 m/s which is very different from the one in the air. For this reason a gel is usually applied on the skin in order to avoid the interact between the air and the tissue.

In most cases, there are two kinds of US waves reflections during imaging process.

Reflection on a plane surface: specular reflection (mirror effect)
This kind of reflection happens when the transmitted ultrasound wave encounters an interface whose size is much bigger than the US wavelength. In this case, when θ_i is equal to 0, the transducer can receive the maximum reflected US wave, as shown in Fig. 1.5 (a) .

Reflection on a rough surface or on very small targets: diffuse reflection
In contrast, when the dimension of the target is small compared to the US wavelength, the wave will be scattered in all the direction. This kind of reflection is also called scattering, the target is then called a *scatterer*. These scatterers do not reflect but they vibrate as small spherical particles giving rise to spherical wave in all the directions. The amplitude of this spherical wave (called back-scattered wave) is a fraction of the incident wave. The diffuse reflection is the basis of many concepts in medical imaging. In fact, the "noisy" nature or the "speckle" of US images comes from it. Moreover, the tissues are often modelled as an aggregate of tiny point scatterers as the one shown in Fig. 1.5 (b). In the case of US waves at low frequencies, whose wavelengths are usually long, the diffuse reflection is more likely to appear.

Table 1.2: Acoustical characteristics for some materials [Kouamé 2015]

Medium	Density kg/m^3	Speed of sound m/s	Characteristic acoustic impedance kg/m$^2 \cdot$ s
Air	1.2	333	0.4×10^3
Blood	1.06×10^3	1566	1.66×10^6
Bone	$1.38 - 1.81 \times 10^3$	2070 – 5350	$3.75 - 7.38 \times 10^6$
Brain	1.03×10^3	1505 – 1612	$1.55 - 1.66 \times 10^6$
Fat	0.92×10^3	1446	1.33×10^6
Kidney	1.04×10^3	1567	1.62×10^6
Lung	0.40×10^3	650	0.26×10^6
Liver	1.06×10^3	1566	1.66×10^6
Muscle	1.07×10^3	1542 – 1626	$1.65 - 1.74 \times 10^6$
Spleen	1.06×10^3	1566	1.66×10^6
Distilled water	1.00×10^3	1480	1.48×10^6

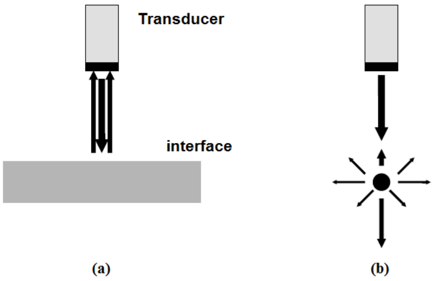

Figure 1.5: Two kinds of reflections. (a) Specular reflection (mirror effect), (b) diffuse reflection [Kouamé 2015].

1.2.4 Attenuation

While propagating, the amplitude of an US wave decreases. This wave amplitude loss is called *attenuation*. US waves are attenuated over time by several mechanisms: absorption (dissipation of energy converted into heat), diffusion (creation of secondary waves) and mode conversion (transverse wave transformation or shear). From section 1.2.2, we know that $p(z,t)$ represents a forward plane wave who is travelling in $+z$ direction. Let us denote $p(0,t)$ by

$$p(0,t) = A_0 s(t) \tag{1.8}$$

where A_0 is the original amplitude of the wave, and $s(t)$ represents the US wave. Consider only the forward traveling wave $p_+(z,t)$ in (1.5) for the moment, in the absence of attenuation, *i.e.* the ideal case,

$$p(z,t) = A_0 s(t - z/c) \tag{1.9}$$

However, because of the attenuation, we actually have

$$p(z,t) = A(z)s(t - z/c) \tag{1.10}$$

where $A(z)$ is the amplitude of the wave depending on the z-position. The amplitude decay is usually modelled as

$$A(z) = A_0 e^{-\alpha_L z} \tag{1.11}$$

where α_L is the amplitude attenuation factor expressed in m^{-1} or Nepers/cm. From (1.11), we have

$$\alpha_L = \frac{1}{z} ln(\frac{A(z)}{A_0}) \tag{1.12}$$

Since generally the gain in amplitude is expressed in dB, the amplitude attenuation factor in dB/cm is defined by

$$\alpha = 20log_{10}(e)\alpha_L \approx 8.69\alpha_L \qquad (1.13)$$

where α is called attenuation coefficient.

Moreover, the attenuation coefficient depends on the frequency f of the wave, the model generally admitted to represent their relation is

$$\alpha(f) = \beta f^m \qquad (1.14)$$

where m is slightly greater than 1 for most biological tissues. In other words, an US wave with higher frequency attenuates faster, thus its depth of penetration is smaller.

Time Gain Compensation (TGC)

Time Gain Compensation (TGC) is a widely known enhancement mechanism to reduce the effect of attenuation in US imaging systems. Its principle is to divide the image into bands which are orthogonal to the direction of propagation and involve a variable gain to each band. The adjustment must be made to achieve a gray level which is approximately globally uniform. Figure 1.6 provides an overview of this approach in the case of 4-zone correction. Each zone has an adjusted gain to compensate locally the average loss. Finally, if the dynamics of an ultrasound imaging device is known, then its maximum exploration depth can be determined, that is to say, the distance beyond which US wave will not have enough energy to be captured by the transducer.

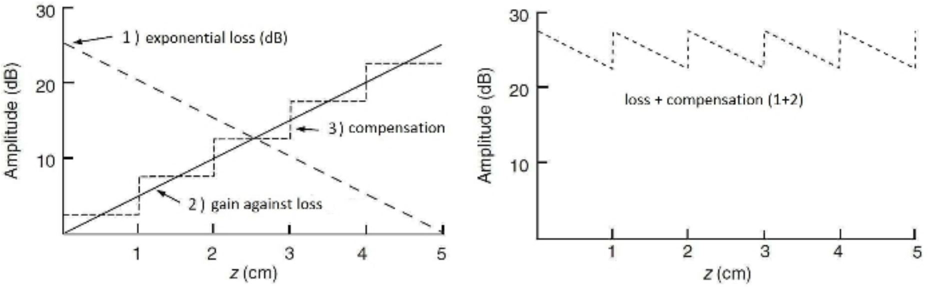

(a) (b)

Figure 1.6: Principle of gain compensation over time. (A) The exponential decay in dB is offset by a gain of the same shape approximated by zones. (B) Effect resulting from loss compensation [Prince 2006].

1.2.5 Doppler Effect

Aside from the reflection/transmission and attenuation, the *Doppler effect* of US waves is also very important allowing the development of Doppler Ultrasound (see section 1.3.1.4). *Doppler effect* describes the change in frequency of a wave for an observer moving relatively to the source of the wave. For example, this change can be commonly

heard when a vehicle sounding a siren approaches, passes, and recedes from an observer. The frequency of the received wave will be higher during approach, identical at instant of passing by and lower during recession.
In Fig. 1.7, we show a simple example of Doppler ultrasound imaging. The transducer emits the US wave at the frequency of f_e which transmits at the speed of c. v is the velocity of blood flow and θ is the angle between the US wave propagation and the blood flow. Because of the *Doppler effect*, the *Doppler shift* will happen. That is, the received US wave will have a different frequency f_d. Since the variation in frequency is due to the movement of the blood while the wave is not modified and its wave length is preserved, we can compute the Doppler frequency f_d as $\frac{2f_e\|v\|cos\theta}{c}$.

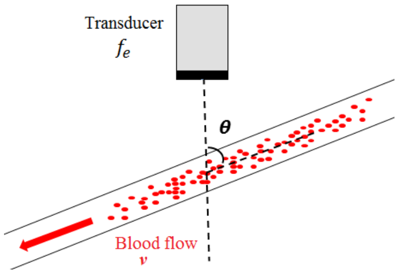

Figure 1.7: Doppler ultrasound effect.

1.3 Ultrasound image formation

As described in the subsection above, US waves are produced by a piezoelectrical transducer and then transmitted, reflected, attenuated. To form an US image, the US echos will still need to be received and interpreted. In this section, we will describe the main principles of US image formation.

1.3.1 Ultrasound images modes : A, B, M, Doppler

Once the US echos are acquired by the US probe, there are many ways to view the results for the user depending on the characteristics of the probe, the scope and the physical properties of the tissues to be imaged.

1.3.1.1 A-Mode

A-mode, denoting the *Amplitude Mode*, is the starting point of US imaging systems since it consists of displaying the amplitude of 1D echoes of a single pulse, after detection of their envelope, as a function of the distance it has traveled (or equivalently the travel time) in the direction of propagation z.

The transducer firstly emits an ultrasonic pulse and then it runs the receiver for the remainder of the cycle time to capture the echoes from the tissue. These pressure waves picked up by the transducer are converted to electrical current by the piezoelectric element and the evolution of this electric current over time forms the Radio Frequency line (RF line). An example of RF line together with the corresponding detected envelope signal is shown in Fig. 1.8.

One can thus observe a typical signal in A-mode with the first detected peak corresponding to the initial echo of the transmitted pulse. All these peaks can bring the user information about the structure of the analyzed medium: penetration into the human body at the skin, the interfaces of the organs, etc.

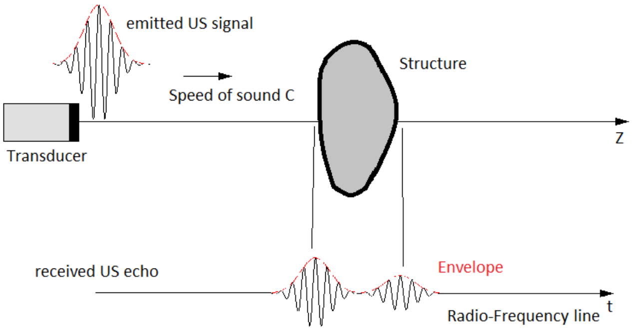

Figure 1.8: Scheme for obtaining the A-Mode.

1.3.1.2 B-Mode

To form a 2D US image, a typical operation is to move (mechanically or electronically) the active area of the transducer according to the lateral axis x. One RF 1D line corresponds to one column of the 2D US image. The scanning can be done in several ways and affects the outlook of the final image. The US image composed by multiple RF lines is also called RF image, see Fig. 1.9(a). We may remark that the RF image is difficult to interpret visually. A common way to improve its visibility is to process envelope detection followed by logarithmic compression to reduce the dynamics of the image. The dynamics of the image is usually reduced from 120 to 60 dB to suit human vision. The relationship between RF and B-mode image is illustrated in a thyroid image in Fig. 1.9.

1.3.1.3 M-Mode

The M-mode, also known as Time Motion or TM-Mode, aims at displaying the juxtaposition of 2D A-mode signals over time. Every A-mode signal is translated in gray scale as a column of the image and its temporal evolution can be followed in the horizontal

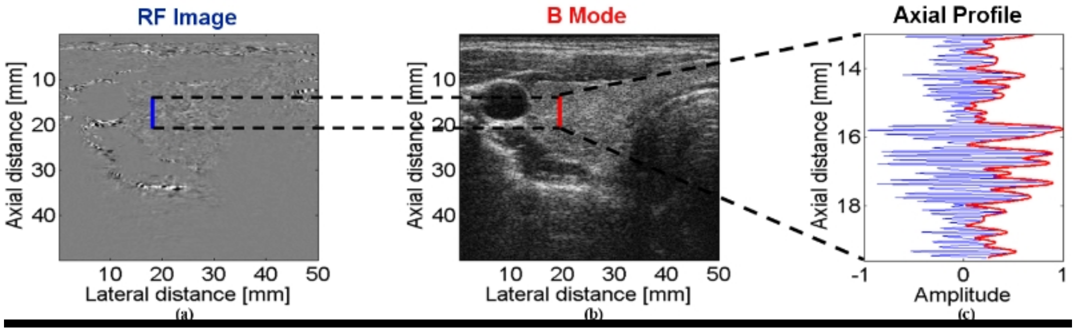

Figure 1.9: Relationship between RF and B-mode image for a thyroid image [Basarab 2008]. (a) RF image, (b) B-Mode image, (c) an extraction of axial profile, RF signal in blue and corresponding envelope in red.

direction, see Fig. 1.10 (a). Thus, the M-mode image can represent moving structures over time. Initially a 2D image is acquired and a single scan line is placed along the area of interest, see Fig. 1.10 (b). The M-mode will then show how the intersected structures move toward or away from the probe over time.

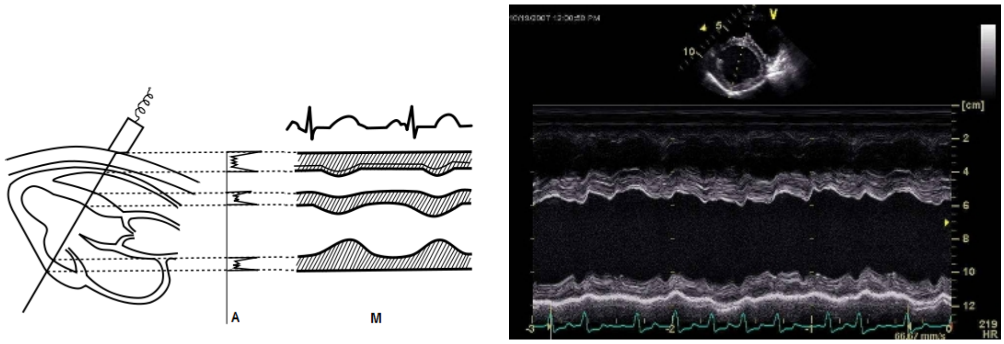

(a)

(b)

Figure 1.10: (a) Scheme for obtaining the M-Mode, (b) an M-Mode example in cardiac imaging [Szabo 2004].

1.3.1.4 Doppler mode

Doppler Ultrasound imaging is based on the *Doppler effect* as described in the previous section 1.2.5. It can be used to detect the flow in a vessel, the direction of the flow and its type (arterial or venous, normal or abnormal). Moreover, it is able to measure the flow velocity. Compared to other modes, the Doppler US requires higher frame rate. However, higher frame rate usually turns into lower resolution which will be discussed

in a later section.
The Doppler US instrument has been developed rapidly from Continuous Wave (CW) Doppler to Pulsed Wave (PW) Doppler, Duplex Doppler, Color Doppler and Power Doppler. We hereby give an example of Duplex Doppler in Fig. 1.11. For Duplex Doppler, both B-mode and Doppler need to be displayed. The scanner has to be able to switch between imaging and Doppler modes at a sufficiently high rate to permit real-time "duplex" imaging at a somewhat reduced frame rate. Although this is sometimes at the expense of signal-to-noise performance of the Doppler system, the facility of simultaneous imaging and Doppler is useful when there are slow movements (such as those of respiration or of a fetus) making the positioning of the Doppler volume difficult.

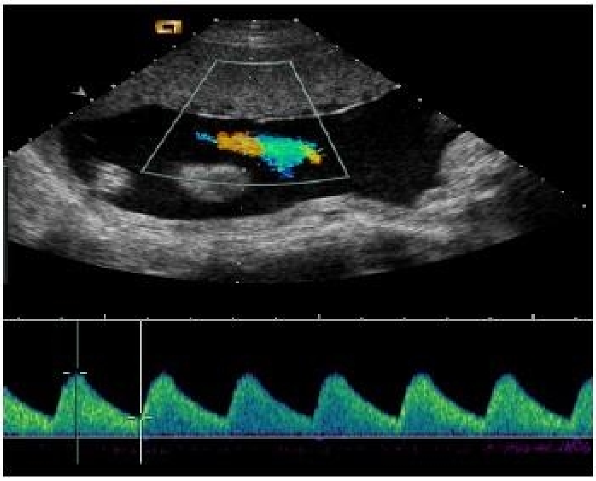

Figure 1.11: Duplex Doppler US image showing both B-mode image and the doppler image [Kouamé 2015].

1.3.2 Ultrasound acquisition schemes

Although in some US imaging modes (such as A and M modes), the 1D signal in the direction of propagation which is called axial direction will be enough, it is necessary to move the transducer assembly in a second direction which is called lateral direction to form 2D images. For 3D imaging, the third dimension (azimuthal direction) will also be necessary. This kind of scanning may be performed mechanically in the case of a single-element probe (Fig. 1.12) or electronically in the case of a multi-element probe.

In practice, the probe used by the physician remains stationary during a short period of time of image acquisition. In the case of a single-element transducer, an electric motor located inside the probe moves physically the element. In the case of a multi-element piezoelectric array, scanning may be performed by stimulating a portion of the elements and moving electronically this active zone via the beamforming techniques explained in the subsection below.

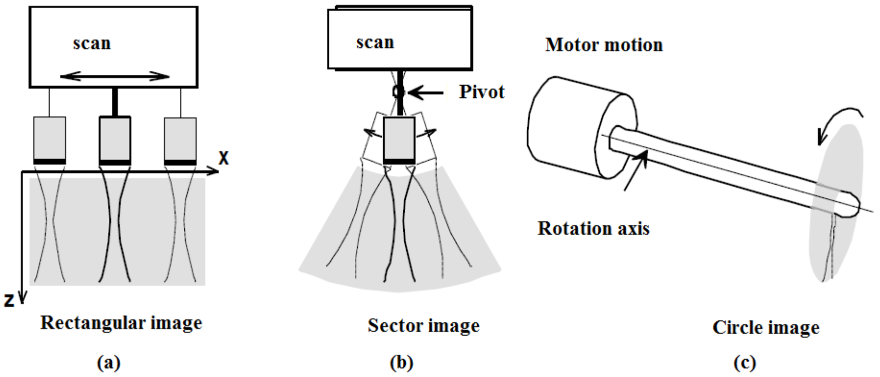

Figure 1.12: Ultrasound acquisitions with a single element transducer. (a) Rectangular image, (b) sector image and (c) circle image [Kouamé 2015].

3D imaging. Since the anatomy is usually 3D, the medical doctors usually need to combine mentally several 2D images in order to obtain a 3D representation of the organ anatomy. In order to overcome this limitation in 2D US imaging, 3D US imaging systems have been developed. There are also various kinds of acquisition of 3D US images. The existing strategies include the use of linear arrays in mechanical and free-hand scanning and the use of 2D matrix arrays. For the former two ways of acquisition, a 2D transducer (shown in Fig. 1.13) is used followed by dedicated post-processing. Usually, a large number of US lines need to be acquired, which brings a trade-off between data volume and/or frame rate and spatial resolution (see section 1.3.4). The matrix array transducer (shown in Fig. 1.13) was designed to overcome the speed limitations and the need to move by hand. The main challenge of this technique is to physically connect all the elements to wires and activate them on transmission/reception modes. Since this kind of technology is complex, few companies provide it and these systems are not yet common in the clinical routine [Lorintiu 2015a].

1.3.3 Focusing and beamforming

The summation of all waves generated by the piezoelectric crystals forms the ultrasound *beam*. The ideal ultrasound beam is usually considered as narrow as possible, similar to a laser, as shown in Fig. 1.14 (a). However, as one can expect, this ideal situation is not possible in practice, thus influencing the lateral resolution of US images (see section 1.3.4). It is necessary to concentrate the energy emitted by the transducer in a given area in order to better identify local echoes, see Fig. 1.14 (c). The *Focal Zone* is the area in the ultrasound beam that has the smallest beam diameter. Through the technique of beamforming, the spatial shape of the pulse can be adjusted to make it as close as possible to a narrow beam. There are two kinds of beamforming, one is called *mechanical beamforming* and the other one is *electronic beamforming*.

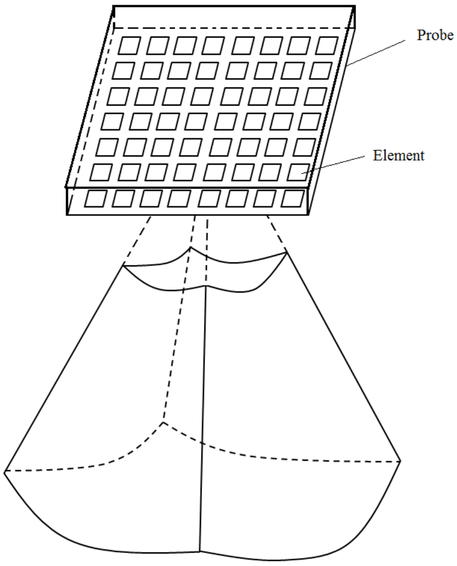

Figure 1.13: A 2D matrix array transducer.

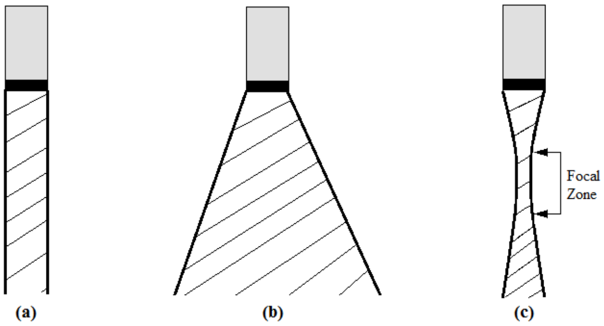

Figure 1.14: Shapes of ultrasound beams. (a) ideal beam, (b) unfocused beam, (c) focused beam.

Mechanical beamforming
In this case, the focusing can be performed by mechanically adding a concave lens on the front of the single element transducer. However, the beam will tend to diverge (increased beam width) once it passes the focal zone.

Electronic beamforming
For multi-element probes, the focusing can be done by electronic beamforming techniques. The main principle of this kind of technique is to play with the offset (emission or reception) of each piezoelectric element signal in order to optimize performance of an area and/or a direction.

The most commonly used electronic beamforming technique is called delay and sum (DAS) beamforming. The idea is to transmit or to receive the US waves taking into account the relative delay between different elements of the piezoelectric array and sum all these signals consistently to improve the image quality of an area and/or a particular direction, as it is schematically illustrated in Fig. 1.15. The focusing can be done in a conventional manner to a focal point or set dynamically by taking into account the evolution of this focus area over time. The data acquired before receiving beamforming is called *raw RF data* or *channel RF data* and the one after beamforming in reception is usually called *beamformed RF data*.

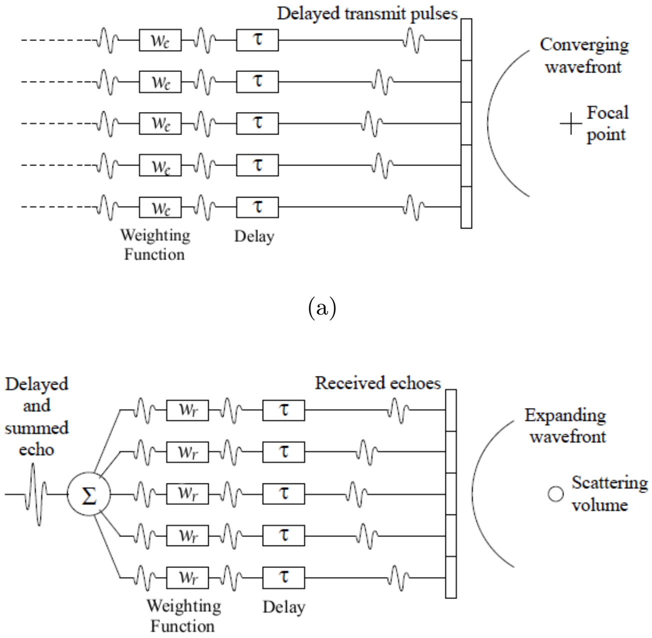

(a)

(b)

Figure 1.15: Delay and sum beamforming. (a) in emission, (b) in reception [Lorintiu 2015a].

1.3.4 Spatial Resolution

Spatial resolution represents the ability of an US system to distinguish two structures close to each other. In other words, it determines the degree of image clarity. The spatial resolution of an US system is determined by the axial and lateral resolutions, both of them are closely related to the ultrasound frequency and bandwidth.

1.3.4.1 Axial Resolution

Axial resolution, also called depth resolution, refers to the ability to display and distinguish two structures that are close together and lie along the axis of the ultrasound beam. Axial resolution is directly affected by the frequency of the transducer and the *pulse length*. Ultrasound waves are generated in pulses and each pulse commonly consists of 2 or 3 sound cycles of the same frequency. The *pulse length* is the distance travelled per pulse before vanishing. A high frequency wave with a short pulse length will yield better axial resolution than a low frequency wave, see Fig. 1.16.

From an instrumental point of view, the axial resolution can be improved mainly by increasing the frequency of the emitted US wave. However, we should keep in mind that if the probes run from 20 to 30 MHz, the depth of penetration will be decreased because of the phenomena of attenuation (see section 1.2.4). Instrumental techniques based on increasing the frequency of the probe have now reached their physical limit related to technological considerations, like the clock frequency of computer processors.

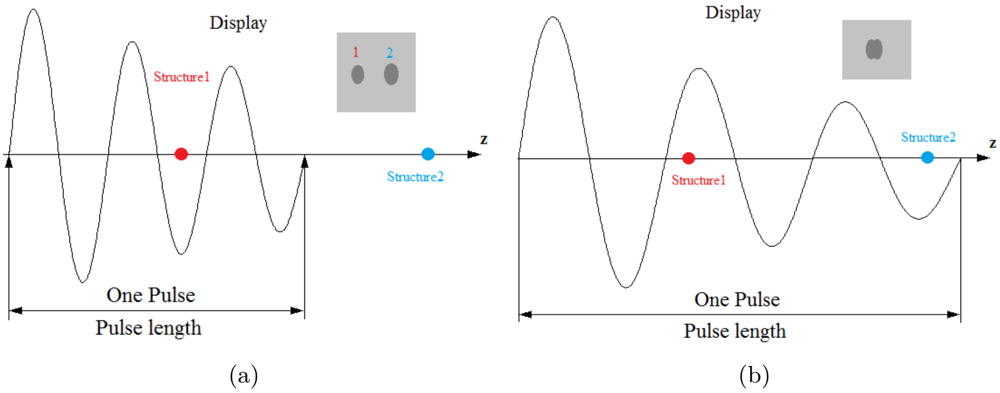

(a) (b)

Figure 1.16: (a) A high frequency wave with a short pulse length, (b) A low frequency wave with a long pulse length.

1.3.4.2 Lateral Resolution

Lateral resolution represents the ability to display and distinguish two structures that are close together and lie in a plane perpendicular to the ultrasound beam. Fig. 1.17 illustrates an example of three structures in a same lateral line. The distance between structure 1 and 2 is within the beam width, making the returning echoes overlapping with each other side by side. Thus, we cannot distinguish these two structures in the display image anymore.

From this example, one can conclude that the lateral resolution in an ultrasound beam varies with beam width. Therefore, it can be improved in two ways. The first one is to further reduce the beam width by adjusting the focal zone. Lateral resolution is the best at the focal zone, where the beam is the narrowest. Using beamforming techniques, the focusing can be modified to give an optimal resolution in the region of interest. The second one is to increase the frequency of the probe. The higher the frequency is, the shorter wavelenth the US wave is and the thinner the beam is. It is therefore clinically important to choose the highest frequency transducer possible to keep the beam width as narrow as possible in order to provide the best possible lateral resolution. However, as it was mentioned above, one must strike a right balance between resolution and attenuation. Finally it is possible to combine the two ways of improving lateral solution.

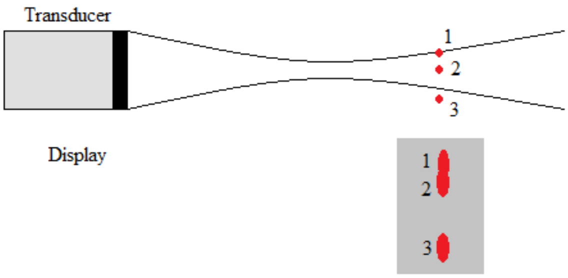

Figure 1.17: An example for lateral resolution.

Point Spread Function (PSF) A conventional approach to evaluate the resolution of an US imaging system is to analyze its PSF which contains complete information about the spatial resolution. The PSF represents the response of an US imaging system to a single point object. Using a Gaussian 1D PSF as example in Fig. 1.18, there are three different situations: the source points imaged by the acquisition system are separated, or at the limitation of resolution, or mixed. The Full-Width-at-Half-Maximum (FWHM) value is the common way to quantify the spatial resolution.

Regarding the 2D case, Fig. 1.19 displays an example of simulated US 2D PSF using Field II [Jensen 1996]. We can see 20 different PSFs in the same image, *i.e.*, the response of the US imaging system to 20 points at different depths. We may remark that the PSF represents both axial and lateral resolutions. While the frequency, the probe, and the focal zone are directly related to the spatial resolution as discussed above, they have thus a key influence on the PSF. Playing an important role in our research about image resolution enhancement, the PSF will be discussed in details in the next chapter.

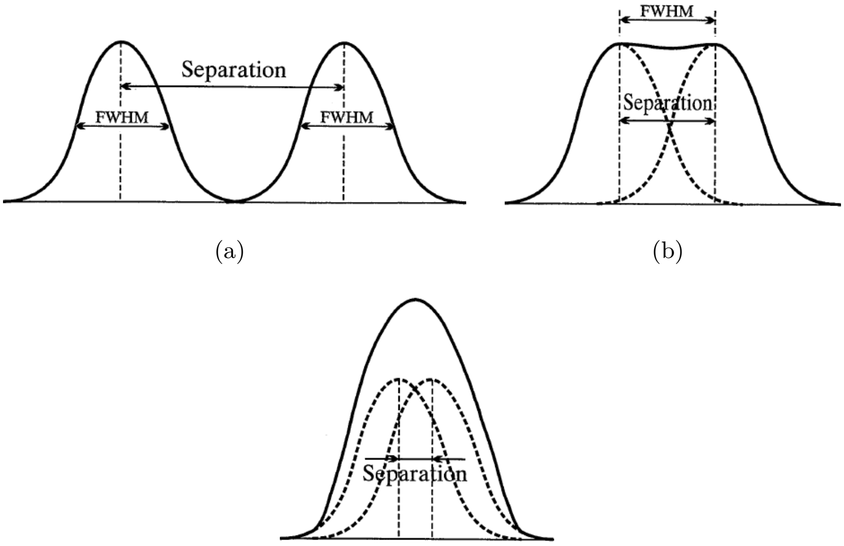

(a)

(b)

(c)

Figure 1.18: Three different cases of resolution in terms of FWHM: the source points are (a) separated, (b) at the limit of resolution and (c) confused. According to [Prince 2006].

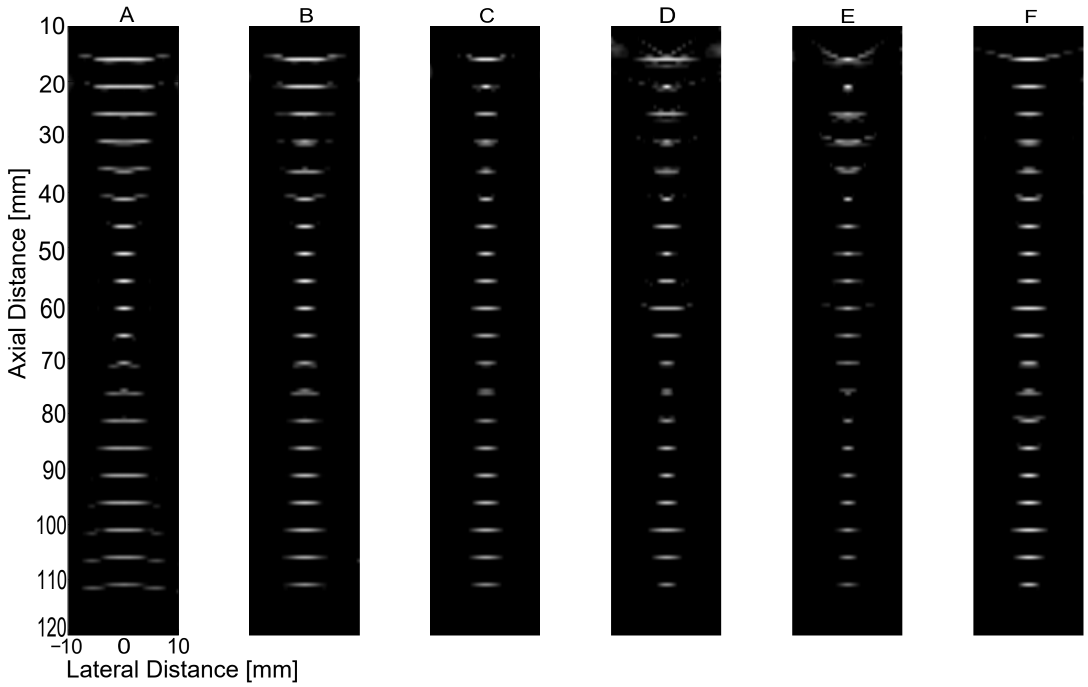

Figure 1.19: US PSFs simulated by Field II with a frequency of 3 MHz. In the graphs A - C, 64 of the transducer elements was used for imaging, and the scanning was done by translating the 64 active elements over the aperture and focusing in the proper points. In graph D and E 128 elements were used and the imaging was done solely by moving the focal points. Graph A uses only a single focal point at 60 mm for both emission and reception. B also uses reception focusing at every 20 mm starting from 30 mm. Graph C further adds emission focusing at 10, 20, 40, and 80 mm. D applies the same focal zones as C, but uses 128 elements in the active aperture. The focusing scheme used for E and F applies a new receive profile for each 2 mm [Jensen 1996].

1.4 Open challenges

Compared to other devices, ultrasound imaging has many advantages such as the high flexibility, low cost and noninvasive nature. It is therefore positioned as a preferred medical imaging modality. However, it still faces two main challenges listed below.

1.4.1 Image quality enhancement

All the advantages of US imaging come at a price - the reduced resolution and contrast compared to other image modalities. While the quality of a medical image determines the ability of a device to view the details of a biological structure, potentially important for diagnosis, it is facing physical and technological limitations today: the technological limitations related to the manufacture of high frequency piezoelectric elements, and the physical limitation related to the spread of US in tissues that it can hardly penetrate deeper at higher frequencies.

Many studies have therefore been undertaken to improve US image quality using post-processing approaches. As a typical class of these techniques, state-of-art deconvolution methods in US will be presented in Chapter 2.

1.4.2 Higher frame rate and/or less acquired data volume

The development and application of Doppler US imaging and 3D imaging bring a growing demand for higher frame rate or less data volume acquisition. While US imaging is still considered a "real-time" modality, it may however suffer from the frame rate. For example, in Doppler imaging and 3D imaging, the frame rate is strongly decelerated and the data volume is substantially increased. Moreover, the frame rate and the data volume usually conflict with the spatial resolution. Therefore, how to keep a reasonable spatial resolution when accelerating the frame rate or reduce the data volume is a new challenge in US imaging.

Instrumental solutions related to the emission modes like ultrafast imaging [Tanter 2014] have been proposed lately to overcome this issue. Another possible solution for post-processing would be the compressive sampling framework which will be presented in the next chapter.

Chapter 2

Compressive sampling and Deconvolution

Contents

The second chapter focuses on describing compressive sampling and deconvolution, two frameworks that will be used in this thesis. Compressive sampling, which aims at long term accelerating the frame rate or reduce the data volume, is firstly presented. Its theory, the state of art methods and its application in ultrasound imaging are included. We will then introduce the deconvolution by highlighting its effect on image quality enhancement. Numerous deconvolution algorithms applied in ultrasound imaging will be discussed. Finally, the main contributions of this thesis will be briefly highlighted in the last section of this chapter.

2.1 Compressive sampling

To accomplish the objective of less data volume, *compression* represents the technique of choice. Once the image is found to be sparse or to have a compressed representation in a basis or a frame, the values of the largest coefficients will be preserved and the rest of the coefficients discarded. Thus the data volume is reduced. However, since the image still needs to be completely acquired, the frame rate is not reduced due to compression.

In this context, compressive sampling is considered as one of the most promising techniques to reduce the acquired data volume (potentially accelerating the frame rate) without degrading the image quality.

2.1.1 Problem Formulation

Conventional approaches to sample signals or images follow the Shannon-Nyquist theorem. According to the Shannon-Nyquist sampling theorem, the sampling rate must be at least twice the maximum frequency presented in the signal. However, the theory of Compressive Sampling makes it possible to go against the common knowledge in data acquisition.

2.1.1.1 Direct Model

Compressive Sampling (CS), also known as compressed sensing, allows to recover, via non linear optimization routines, an image from few linear measurements (below the limit standardly imposed by the Shannon-Nyquist theorem) [Donoho 2006, Candès 2006a]. The direct model of CS is

$$\boldsymbol{y} = \Phi \boldsymbol{r} \tag{2.1}$$

where $\boldsymbol{y} \in \mathbb{R}^M$ corresponds to the M compressed measurements of signal or image $\boldsymbol{r} \in \mathbb{R}^N$, $\Phi \in \mathbb{R}^{M \times N}$ represents the acquisition matrix, also called *sampling matrix*, with $M << N$.

The CS theory demonstrates that $\boldsymbol{r}$, containing N samples or pixels, may be recovered from the M measurements in $\boldsymbol{y}$ provided two conditions: i) the image must have a sparse representation in a known basis or frame and ii) the measurement matrix and sparsifying basis must be incoherent [Candès 2008]. These two concepts are detailed hereafter.

2.1.1.2 Sparsity

When a signal or an image can be expressed as a linear combination of just a few non-zero values in a known basis, frame or dictionary, we can say that the signal/image is sparse.

$$\boldsymbol{r} = \Psi \boldsymbol{a} \tag{2.2}$$

where $\boldsymbol{a}$ is the sparse representation of $\boldsymbol{r}$ in the basis of Ψ. If $\boldsymbol{a}$ only contains $K(K < N)$ non zero coefficients, $\boldsymbol{r}$ is called *K-sparse*.

Although sparsity is almost never reachable due to the presence of noise, one can find that many natural signals/images have almost sparse representations in certain basis. That is, most of the coefficients are small and almost the whole energy of the image is contained by a small number of elements. For example, the image in Fig. 2.1(a) has the coefficients in wavelet domain as Fig. 2.1(b) (Haar wavelet, 3 level). One may remark from the image that most coefficients are small, thus the relatively few large coefficients can store most of the information. By taking only 5% of the largest coefficients, most of the information in the original image can be reconstructed shown as Fig. 2.1(c).

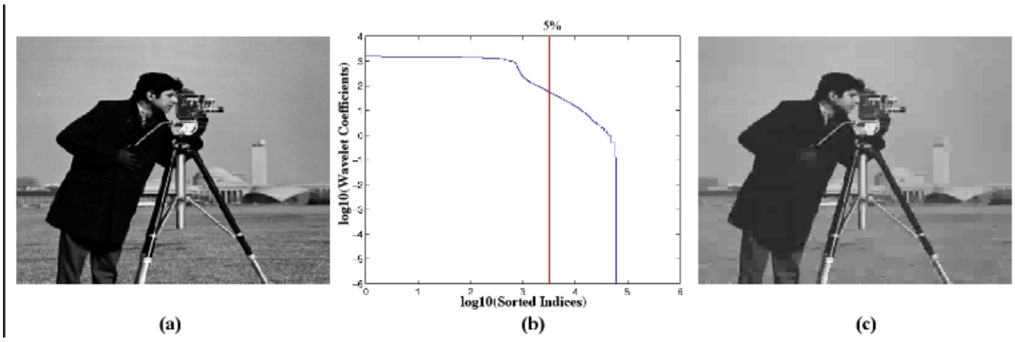

Figure 2.1: (a) Original image (256×256) and (b) its sorted wavelet transform coefficients in log-scale. (c) The reconstruction obtained by setting all the coefficients in wavelet domain to zero except the 5% largest.

Aside from the wavelet basis, there are other known basis such as Fourier, curvelets, and wave atoms that have already been used in the literature to provide sparsity [Candès 2005, Candès 2006b, Candès 2008, Baraniuk 2007]. If certain characteristics of the signal/image are known, the sparsest representation basis will be chosen among known basis. Otherwise, adaptive dictionaries could be obtained through dictionary learning to build more sparse representation [Duarte-Carvajalino 2008]. However, for known basis, mathematical properties are usually well known and the associated transforms provide fast implementations [Mallat 1999].

2.1.1.3 Incoherence

The *coherence* between the sampling matrix Φ and the sparsifying basis Ψ is defined as

$$\mu(\Phi, \Psi) = \sqrt{N} \cdot \underset{1 \leqslant k,j \leqslant N}{max} |\langle \phi_k, \psi_j \rangle| \tag{2.3}$$

where $\langle \phi_k, \psi_j \rangle$ represents the inner product between the k-th column of Φ and the j-th column of Ψ.

The coherence above measures the largest correlation between any two elements of Φ and Ψ [Candès 2008, Donoho 2001]. The value of $\mu(\Phi, \Psi)$ drops in $[1, \sqrt{N}]$. If Φ and Ψ contain correlated elements, the coherence is large. Otherwise, it is small. Compressive sampling is mainly concerned with low coherence pairs, in other words, incoherent pairs.

In the next subsection, we will show the importance of the incoherence between Φ and Ψ. In subsection 2.1.2, we will review the existing techniques to compose the sampling matrice Φ.

2.1.1.4 Sparse recovery

With the sparse representation in (2.2), (2.1) can be rewritten as

$$\boldsymbol{y} = A\boldsymbol{a} \tag{2.4}$$

where $A = \Phi\Psi$. According to CS framework, $\boldsymbol{a}$ can be recovered by solving the following ℓ_0-minimization problem (P_0):

$$(P_0) \qquad \min_{\boldsymbol{a} \in \mathbb{R}^N} \parallel \boldsymbol{a} \parallel_0 \quad \text{subject to} \quad \boldsymbol{y} = A\boldsymbol{a} \tag{2.5}$$

where $\parallel \boldsymbol{a} \parallel_0 = \#(i | \boldsymbol{a}_i \neq 0)$ representing the total number of non-zero elements in vector $\boldsymbol{a}$. (P_0) seeks the sparsest solution to (2.1). However, solving (P_0) requires exhaustive searches over all subsets of columns of A, a procedure which is combinatorial and has thus exponential complexity.

An alternative to (P_0) is to consider the convexification of (2.5) to an ℓ_1-norm minimization problem, namely basis pursuit problem [Chen 2001]:

$$(P_1) \qquad \min_{\boldsymbol{a} \in \mathbb{R}^N} \parallel \boldsymbol{a} \parallel_1 \quad \text{subject to} \quad \boldsymbol{y} = A\boldsymbol{a} \tag{2.6}$$

where $\parallel \boldsymbol{a} \parallel_1 = \sum_{i=1}^{N} |\boldsymbol{a}_i|$. It has been proven that the (P_1) problem gives an exact reconstruction with the Restricted Isometry Property which will be detailed later.

Theorem 1 ([Candès 2007a]) *Fix $\boldsymbol{r} \in \mathbb{R}^N$ and suppose that the coefficient sequence $\boldsymbol{a}$ of $\boldsymbol{r}$ in the basis Ψ is K-sparse. Select M measurements in the Φ domain uniformly at random. Then if*

$$M \geqslant C \cdot \mu^2(\Phi, \Psi) \cdot K \cdot logN \tag{2.7}$$

for some positive constant C, the solution to (2.6) is exact with overwhelming probability.

From this theorem we may firstly conclude that the smaller the coherence, the fewer measurements are needed for exact reconstruction. At the same time, the sparsity of the signal/image is also related since a more sparse signal/image has a smaller number K.

2.1.1.5 The Restricted Isometry Property (RIP)

The theoretical results previously correspond to the noiseless case. However, in practice, we are always in presence of noise. We will continue the discussion on CS with the more general case:

$$\boldsymbol{y} = A\boldsymbol{a} + \boldsymbol{n} \tag{2.8}$$

where $\boldsymbol{n}$ is an additive Gaussian noise with a bounded energy. The corresponding reconstruction can be done by using ℓ_1-minimization with relaxed constraints [Candès 2008]:

$$(P_2) \qquad \min_{\boldsymbol{a}\in\mathbb{R}^N} \parallel \boldsymbol{a} \parallel_1 \quad \text{subject to} \quad \parallel \boldsymbol{y} - A\boldsymbol{a} \parallel_2^2 \leq \epsilon \tag{2.9}$$

where ϵ is a noise related hyper-parameter.

In this context, the restricted isometry property (RIP) which allows to study the general robustness of CS and provides a mean to evaluate the precision of the reconstruction was introduced by Candès, Tao and others [Candès 2005, Candès 2006b, Candès 2006a, Baraniuk 2008].

Definition 1 ([Candès 2005]) *For each integer $K = 1, 2, ...,$ define the isometry constant δ_K of a matrix A as the smallest number such that*

$$(1 - \delta_K) \parallel \boldsymbol{a} \parallel_2^2 \leq \parallel A\boldsymbol{a} \parallel_2^2 \leq (1 + \delta_K) \parallel \boldsymbol{a} \parallel_2^2 \tag{2.10}$$

holds for all $K-$sparse vector $\boldsymbol{a}$.

We say that the matrix A obeys RIP of order K if $\delta_K \in (0, 1)$. To better explain the RIP, let us take an extreme example. Suppose $\delta_K = 0$, then A is an orthogonal matrix which means that it should be a square matrix. However, in CS, A is supposed to be a "short" and "fat" matrix, *i.e.*, $M << N$. Thus RIP describes the approximate orthogonality of the matrix of A. That is, for a matrix which obeys RIP of order K, all subsets of K columns taken from it are nearly orthogonal. The smaller the δ_K is, the closer the A is to be orthogonal.

To reconstruct the signal/image from compressed measurements, we need to guarantee the distance between every two signals/images is preserved after the sampling. That is, $(1 - \delta_{2K}) \parallel \boldsymbol{a}_1 - \boldsymbol{a}_2 \parallel_2^2 \leq \parallel A\boldsymbol{a}_1 - A\boldsymbol{a}_2 \parallel_2^2 \leq (1 + \delta_{2k}) \parallel \boldsymbol{a}_1 - \boldsymbol{a}_2 \parallel_2^2$ holds for all K-sparse vectors $\boldsymbol{a}_1$,$\boldsymbol{a}_2$. This is how RIP connects with CS.

If RIP holds, then (P_1) problem gives an exact reconstruction [Candès 2006b, Candès 2008, Cohen 2009].

Theorem 2 **([Candès 2006b])** *Assume that* $\delta_{2K} < \sqrt{2} - 1$*. Then the solution* $\boldsymbol{a}^*$ *to* (P_1) *obeys*

$$\begin{aligned} \| \boldsymbol{a}^* - \boldsymbol{a} \|_2 \leq C_0 \cdot \| \boldsymbol{a} - \boldsymbol{a}_K \|_2 / \sqrt{K} \quad \textit{and} \\ \| \boldsymbol{a}^* - \boldsymbol{a} \|_1 \leq C_0 \cdot \| \boldsymbol{a} - \boldsymbol{a}_K \|_1 \end{aligned} \tag{2.11}$$

for some constant C_0*, where* $\boldsymbol{a}_K$ *is the vector* $\boldsymbol{a}$ *with all but the largest* K *components set to* 0*.*

The conclusions of Theorem 2 are stronger than those of Theorem 1. If $\boldsymbol{a}$ is K-sparse, then $\boldsymbol{a} = \boldsymbol{a}_K$, thus, the recovery is exact.

In the noisy case (2.8), the next theorem assesses a stable reconstruction of the signal/image.

Theorem 3 **([Candès 2006b])** *Assume that* $\delta_{2K} < \sqrt{2} - 1$*. Then the solution* $\boldsymbol{a}^*$ *to* (P_2) *obeys*

$$\| \boldsymbol{a}^* - \boldsymbol{a} \|_2 \leq C_0 \cdot \| \boldsymbol{a} - \boldsymbol{a}_K \|_2 / \sqrt{K} + C_1 \cdot \epsilon \tag{2.12}$$

for some constants C_0 *and* C_1*.*

Theorem 3 states that the reconstruction error is proportional to the noise level of the measurements.

2.1.2 Sampling matrices

According to RIP, for successful CS reconstruction, we need to find sensing matrices A with the property that column vectors taken from arbitrary subsets are nearly orthogonal. The larger these subsets, the better. Due to the proved connection between the RIP and the coherence property (section 2.1.1.3) [Cai 2009], the problem turns to construct a sampling matrix Φ which is maximally incoherent with the sparsifying basis Ψ.

Fortunately, it has been shown that random matrices are largely incoherent with any fixed basis [Candès 2008, Eldar 2012]. Thus, a popular family of sampling matrices is a random projection or a matrix of independent and identically distributed (i.i.d.) random variables from a sub-Gaussian distribution such as Gaussian (2.13) or Bernoulli (2.14) [Candès 2006c, Mendelson 2008].

$$\phi_{i,j} \sim \mathcal{N}(0, \frac{1}{M}) \tag{2.13}$$

$$\phi_{i,j} := \begin{cases} +1/\sqrt{M} & \text{with probability} \quad 0.5 \\ -1/\sqrt{M} & \text{with probability} \quad 0.5 \end{cases} \tag{2.14}$$

where $\phi_{i,j}$ is the element of sampling matrix Φ at ith row and jth column. It has been proven that this kind of sampling matrices are universally incoherent with all other sparsifying basis. This universality property of a sampling matrix allows us to sample a signal directly in its original domain without significant loss of sensing efficiency and without any other prior knowledge.

However, this kind of random matrix approach usually requires very high computational complexity and huge memory buffering due to their completely unstructured nature. It is sometimes impractical to build in hardware. To overcome this issue, another class of sampling matrices was developed to have significantly more structure. For example, the partial FFT [Needell 2009b, Candès 2007a] is well known for having fast and efficient implementation. However, it only works well in the case when the sparsifying basis is the identity matrix. The Noiselets has also low-complexity implementation but it is designed to be incoherent with the Haar wavelet basis [Coifman 2001]. T.T.Do [Do 2012] then proposed the structurally random matrix (SRM) to obtain its low complexity, fast computation and universal incoherence with most sparsifying basis at the same time. Since we employed the SRM in our simulations in the next two chapters, we give a detailed description hereafter. The SRM is defined as a product of three matrices:

$$\Phi = \sqrt{\frac{N}{M}} DFR \tag{2.15}$$

where $R \in \mathbb{R}^{N\times N}$ is either a uniform random permutation matrix or a diagonal random matrix whose diagonal entries R_{ii} are i.i.d Bernoulli random variables with identical distribution $P(R_{ii} = \pm 1) = 1/2$. This corresponds to the pre-randomize step which randomizes a target signal by either flipping its sample signs or uniformly permuting its sample locations. $F \in \mathbb{R}^{N\times N}$ stands for the transform step to spread information (or energy) of the signal's samples over all measurements. In practice, F can be fast computable such as popular fast transforms: FFT, DCT, WHT or their block diagonal versions. Finally, a subsample step is done through matrix $D \in \mathbb{R}^{M\times N}$. It randomly pick up M measurements out of N transform coefficients.

Finally more recent works proposed some deterministic sensing matrices with promising results [Naidu 2015].

2.1.3 Sparse recovery algorithms

The core problem in CS is to recover a sparse signal/image $\boldsymbol{a}$ from a set of measurements $\boldsymbol{y}$ by solving a minimization problem such as (P_0), (P_1) or (P_2). A variety of algorithms have been introduced and proposed to perform fast, accurate, and stable reconstruction of $\boldsymbol{a}$ from $\boldsymbol{y}$. We hereby give a brief introduction and review to the existing algorithms by classifying them into three groups: greedy methods, convex optimization-based approaches, and other techniques [Baraniuk 2011].

2.1.3.1 Greedy methods

The intuition of sparse recovery is to find the solution to (P_0). In other words, it is to recover the sparsest $\boldsymbol{a}$ from the measurements $\boldsymbol{y}$. It is well-known that this is an NP-hard problem. Greedy methods tackle this problem by greedily selecting columns of the sampling matrix Φ and iteratively approximate $\boldsymbol{y}$. There are a lot of greedy methods for CS reconstruction, among which the most used are the Matching Pursuit (MP)-based methods and the Iterative Hard Thresholding (IHT).

MP has been firstly introduced in the field of signal processing by [Mallat 1993, Mallat 1999]. The problem of MP is that the complexity grows linearly with the number of iterations. It has been then extended to the Orthogonal MP (OMP) to upper bound the maximum number of MP iterations [Pati 1993]. In [Tropp 2007], Tropp and Gilbert proved that OMP can be used to recover a sparse signal with high probability using CS measurements. However, it is ineffective when the signal is not strictly sparse. For approximately sparse signals in a large-scale setting, the Stagewise OMP (StOMP) proposed by Donoho in [Donoho 2012] is a better choice. Other examples of greedy algorithms include Compressive sampling MP (CoSaMP) [Needell 2009a] and various regularized OMP methods [Needell 2009b, Needell 2010] which have also been developed to guarantee uniform signal recovery.

IHT is a well-known algorithm for solving nonlinear inverse problems. It starts with an initial estimate $\hat{\boldsymbol{a}}_0$ and iterates a gradient descent step followed by hard thresholding until a convergence criterion is met. In [Blumensath 2009], Blumensath and Davies proved that the iterations can converge to a fixed point $\hat{\boldsymbol{a}}$.

Instead of doing a exhaustive search, greedy methods compute iteratively approximation of the signal coefficients and support until a convergence criterion is met. Compared to the convex optimization-based approach described below, they are relatively straightforward and fast. However, they can not always guarantee that the local optimal solution they find is the optimal global solution.

2.1.3.2 Convex optimization-based methods

It has been proven that under certain conditions, the solution to (P_1) can give an exact reconstruction of $\boldsymbol{a}$ when there is no noise while the solution to (P_2) can give a stable one when there is noise (see section 2.1.1.5). Thus, the sparse recovery problem turns to be a convex optimization problem.

(P_2) can be also reformulated as an unconstrained problem:

$$\min_{\boldsymbol{a}\in\mathbb{R}^N} \quad \| \boldsymbol{a} \|_1 + \frac{1}{2\mu} \| \boldsymbol{y} - A\boldsymbol{a} \|_2^2 \tag{2.16}$$

where $\mu > 0$ is a Lagrange parameter which can be chosen by trial-and error, or by statistical techniques such as cross-validation (see section 2.2.2.1). Another formulation of (P_2) is the so-called *Lasso* problem:

$$\min_{\boldsymbol{a}\in\mathbb{R}^N} \quad \| \boldsymbol{y} - A\boldsymbol{a} \|_2^2 \quad \text{subject to} \quad \| \boldsymbol{a} \|_1 \leq \delta \tag{2.17}$$

where δ is a fixed threshold for the ℓ_1-norm term.

Since the applications of CS are usually large-scale (an image of a resolution of 1024×1024 pixels leads to optimization over a million of variables) and the objective function is nonsmooth (ℓ_1 term), a lot of efforts have been made to propose and improve the sparse recovery algorithms. The standard second-order methods such as the interior-point methods (ℓ_1-magic [Candès 2007b], ℓ_1-ls [Kim 2007]) were proposed to solve (2.16). They are usually accurate but problematic with the bottleneck of the calculation of the Newton step. In this context, first-order methods are largely developed. Inspired by the iterative shrinkage (also called *soft thresholding*), numerous methods in this category are now available: the gradient projection method (GPSR) [Figueiredo 2007], the iterative shrinkage-thresholding (IST) method [Daubechies 2004], the fixed-point continuation (FPC) [Hale 2007], the fast IST (FIST) [Beck 2009a], etc. The shrinkage operator on any scalar component can be defined as follows:

$$shrink(s,t) = \begin{cases} s - t \quad \text{if} \quad s > t, \\ 0 \quad \text{if} \quad -t \leq s \leq t, \\ s + t \quad \text{if} \quad s < -t. \end{cases} \tag{2.18}$$

This notion was then extended to that of *proximal thresholding* (proximity operator) by P.L. Combbettes and J.C. Pesquet in [Combettes 2007]. More details about the notion of proximal operator will be given in section 2.2.2.3.

Several algorithms also exist to obtain the solution to the constrained optimization problem in (2.9). Bregman iterations have been shown as an efficient method to obtain the solution to this constrained optimization problem and can be derived by solving a small number of unconstrained problems [Yin 2008]. These algorithms are known to be equivalent to the augmented Lagrangian (AL) method. The ideal of AL was introduced in the 70's, e.g. [Gabay 1976]. It was used by different authors for solving many convex optimization problems [Eckstein 1994, Fortin 2000, Fukushima 1992, He 2002, Kontogiorgis 1998] including the ℓ_1-minimization problem for compressive sampling, e.g. the YALL1 method [Yang 2011]. Moreover, in [Van Den Berg 2008], the spectral projection gradient method (SPGL1) was proposed by Friedlander and Van den Berg based on the Lasso problem in (2.17).

Convex optimization-based approaches always have a guaranteed convergence to the global optimum. The literature of corresponding algorithms proposed in the context of CS is vast. However, to the best of our knowledge, there is no exhaustive review classifying or comparing all these existing algorithms. We thus consider that there is no clear winner which would always achieve the best performance in terms of both accuracy and speed.

2.1.3.3 Other methods

In this section, we will review some other sparse recovery techniques which are classical but have not been mentioned previously.

Aside from the ℓ_0-minimization in 2.1.3.1 and the convex ℓ_1-minimization in 2.1.3.2, the ℓ_p-minimization $(0 < p < 1)$ in (2.19) has also shown its ability for sparse recovery. Numerical experiments in e.g. [Chartrand 2007, Chartrand 2008b, Chartrand 2008a] have demonstrated that fewer measurements are required for exact reconstruction than the case when $p = 1$.

$$\min_{\boldsymbol{a}\in\mathbb{R}^N} \quad \| \boldsymbol{a} \|_p^p \quad \text{subject to} \quad \boldsymbol{y} = A\boldsymbol{a} \tag{2.19}$$

where $\| \boldsymbol{a} \|_p^p = \sum_i |a_i|^p$ represents the ℓ_p-norm of $\boldsymbol{a}$. This minimization problem has also the noisy and unconstrained variants (2.9) and (2.16). In practice, this ℓ_p-minimization can be carried out by various algorithms based on the Iteratively Reweighted Least Squares (IRLS) which was firstly proposed in [Lawson 1961, Beaton 1974] for $p \geq 1$ and then extended to the case of $p < 1$ in [Rao 1999]. Hence, the nonconvexity does not necessarily make the problem intractable [Chartrand 2008c, Daubechies 2010].

Another new class of algorithms called approximate message passing or AMP was firstly introduced by Donoho in [Donoho 2009]. They proposed a simple costless modification to iterative thresholding making the sparsity-undersampling tradeoff of the new algorithms equivalent to that of the corresponding convex optimization procedures.

In addition to the algorithms mentioned above, based on variational frameworks, another family of sparse recovery algorithms are studied in the Baysian framework, where the sparsity constraint is incorporated by choosing a suitable sparse prior on the coefficient vector $\boldsymbol{a}$, e.g. [Dobigeon 2012]. Bayesian pursuit algorithms are the Bayesian counterparts of the greedy method presented in section 2.1.3.1 [Schniter 2008, Zayyani 2009]. There are also Bayesian methods that employ some other fixed and computationally convenient family of priors such as Laplacian or α-stable distribution [Ji 2008, Babacan 2010]. Sparse Bayesian learning (SBL) used a prior that is learned from the data [Tipping 2001, Wipf 2004, Wipf 2007]. The algorithms in this category are usually robust but computationally expensive.

2.1.4 Application to Ultrasound imaging

As described in Chapter 1, despite its intrinsic rapidity of acquisition, several US applications such as Doppler or 3D imaging may require higher frame rates than those provided by conventional acquisition schemes or may suffer from the high amount of acquired data. In this context, CS framework appears as a natural solution to overcome these issues.

Since the first works published in 2010 [Friboulet 2010, Quinsac 2010a, Quinsac 2010b], there have been several studies devoted to this topic to date. In this subsection, we will review the existing works within two aspects, the sparsity study and the incoherent acquisition, which are two key elements for successful CS reconstruction as discussed previously in section 2.1.1.1.

2.1.4.1 Sparsity in US imaging

Existing works have proposed diverse strategies to apply CS framework in different stages of US imaging. Thus, the recovery targets are different, resulting in various sparsity assumptions detailed as below.

Scatterers The works in [Tur 2011, Wagner 2012, Chernyakova 2014, Schiffner 2012, Schiffner 2011] employ CS based on the sparse assumption of scatterer map.

In [Schiffner 2012, Schiffner 2011], the authors propose to image using only a single plane wave emission. The inverse scattering problem is increasingly ill-posed in this case. Thus, they established and investigated a solution based on CS. The approach accounts for the lack of measurement data by assuming sparsity of the scatterers in an arbitrary basis. In their experiments, they have chosen different sparsifying basis such as wave atoms, Daubechies-20 and curvelets, see Fig. 2.2.

In [Wagner 2012], a compressed beamforming method based on the finite rate of innovation model [Tur 2011, Gedalyahu 2011] was introduced. In [Mishali 2011], CS and Xampling ideas were developed to reduce the number of samples needed to reconstruct an image containing strong reflectors. A drawback of this method is its inability to treat speckle, which is of significant importance in medical imaging. Chernyakova and Eldar then extended it to a general concept of beamforming in frequency domain [Chernyakova 2014]. In their works, the authors assume the scatterers are sparse in the direct spatial domain.

Raw RF signals Friboulet et al. and Liebgott et al. studied the feasibility of CS for the reconstruction of raw RF data, *i.e.*, the 2D set of channel RF data gathered at the receive elements [Friboulet 2010, Liebgott 2013]. These raw RF data were subsampled by removing varying amounts of samples and providing the input raw RF to CS reconstruction. Beamforming was then applied to these reconstructed channel RF data using the delay and sum beamformer. ℓ_1-minimization based on three sparsifying bases, Fourier, Daubechies wavelets and wave atoms have been employed. The obtained results showed that the wave atoms give the best reconstruction result.

Beamformed RF signals Most of the works exploring the application of CS in US imaging concern the beamformed RF signals, *i.e.*, the US RF images, are sparse in given basis.

In [Quinsac 2010a, Quinsac 2012, Dobigeon 2012, Basarab 2013], the authors consider the US RF images have a sparse representation in Fourier domain (see Fig. 2.3), while in [Chuo 2013], the RF signals are considered to be sparse in the wavelet domain.

In [Achim 2010, Achim 2014, Achim 2015], ℓ_p-minimization for CS reconstruction has been employed to adjust to the assumption of α-stable distributed beamformed RF

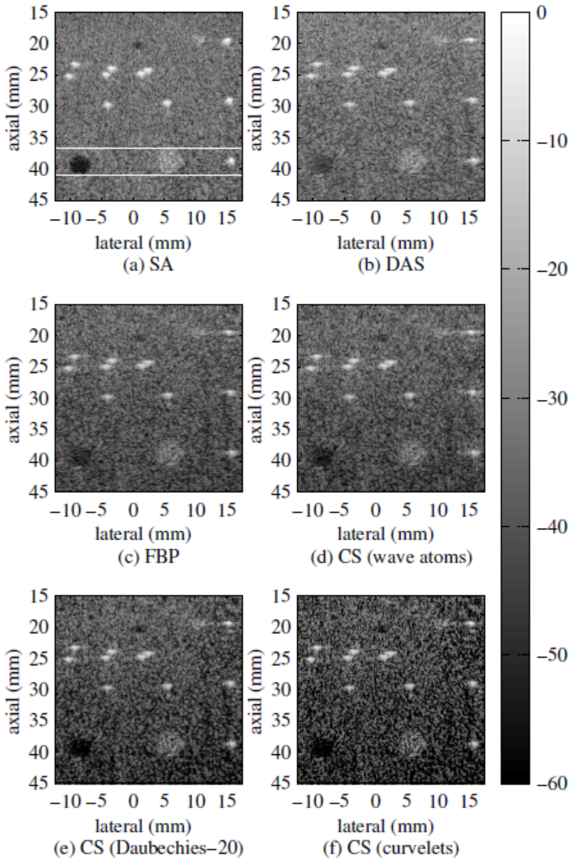

(a) SA
(b) DAS
(c) FBP
(d) CS (wave atoms)
(e) CS (Daubechies−20)
(f) CS (curvelets)

Figure 2.2: Result from [Schiffner 2012]. (a) synthetic aperture (SA; 128 emissions, each of them is emitted from an element and received by all the elements [Jensen 2006]) result with the region of interest indicated, (b) delay and sum, (c) filtered backpropagation [Jensen 2006], (d)-(f) CS results with sparsifying basis of wave atoms, Daubechies-20 and curvelets.

signals. The results showed a significant increase of the reconstruction quality when compared with ℓ_1-minimization algorithms.

Aside from some fixed and known basis, adaptive overcomplete dictionaries could also be used to do the CS reconstruction in US image. The authors in [Lorintiu 2014, Lorintiu 2015b] built sparser representations through dictionary learning for 3D US image reconstruction. However, compared to the fixed and known basis, the resulting dictionaries are more computationally expensive.

2.1.4.2 Incoherent acquisition in US imaging

The existing works mentioned above, according to their different CS application scenarios, exploit three different ways to achieve incoherent measurements.

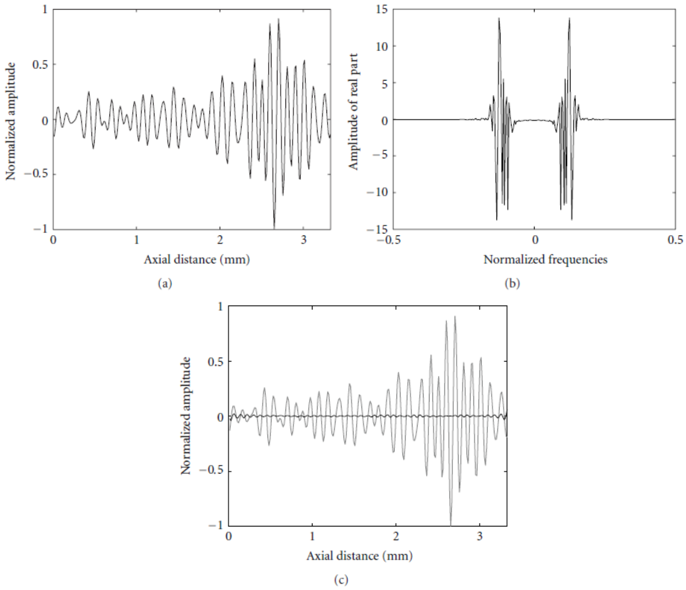

Figure 2.3: Result from [Quinsac 2012]. (a) A fully sampled US RF signal, (b) its sparse representation in Fourier domain where most of the coefficients are equal or close to zero, (c) Compressed US RF signal (gray), corresponding to 30% of the largest Fourier coefficients, the rest of them being set to zero. The difference between the full and compressed US RF signal (black) is minimal.

Plane wave In [Schiffner 2012, Schiffner 2011], the authors applied the CS to regularize the inverse scattering problem modelling the imaging procedure based on single plane wave emission. Thus, the sampling matrix in this case is related to the plane wave propagation.

Xampling The acquisitions in [Wagner 2012, Chernyakova 2014] were obtained using a Xampling-based hardware. It is able to compute low-rate samples of the input from which a certain set of DFT coefficients can be computed on the outputs. The Xampling idea was proposed in [Mishali 2011] for sub-Nyquist sampling.

Random matrices So far, there are two strategies for incoherent acquisition of pre-beamformed or beamformed US data.

Gaussian projections The first one adopted the existing sampling matrices described in section 2.1.2 and take the linear projection of the data on sub-Gaussian random matrices [Friboulet 2010, Achim 2010, Achim 2014, Achim 2015]. Their universal incoherence with most of the sparsifying basis allow the measurements for exact recovery. However, in practice, these random sampling matrices are difficult to implement.

Bernoulli masks The second strategy is to apply a random mask to the US data. The mask, of the same size as the original US data, have entries ones at random positions and zeros elsewhere. However, switching rapidly from one position to the next one in this kind of sampling pattern might be also difficult from the instrumentation point of view. The authors in [Quinsac 2012] proposed to choose uniformly random several lines or columns of the mask and set them all zeros. On the remaining lines or columns, random points are set to zeros and the other to ones (see an example in Fig. 2.4). In other words, the mask allows to skip RF lines in 2D or 3D. The results in [Dobigeon 2012, Basarab 2013, Liebgott 2013, Lorintiu 2014, Lorintiu 2015b] have all showed successful CS recovery using this kind of strategy.

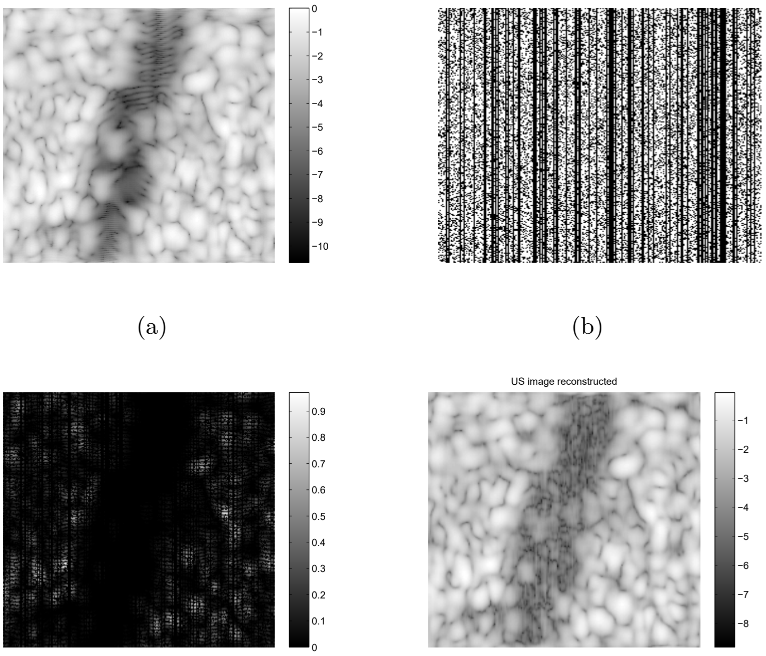

(a) (b)

(c) (d)

Figure 2.4: An incoherent acquisition example using Bernoulli random vectors. (a) Original US image, (b) sampling mask (M/N=0.5), (c) measurements, (d) CS reconstruction [Quinsac 2012].

2.1.5 Conclusion

The fundamental concepts of CS theory, the existing research on CS theory and its application to US imaging have made it possible to recover US images from few linear measurements (below the limit standardly imposed by the Shannon-Nyquist theorem), thus aiming at the objective of higher frame rates or less amount of acquired data.

However, there are still two problems remaining. i) The noise, the incomplete sparsity or the incomplete incoherence make it difficult to get exact CS recovery. For a low number of measurements, the reconstructed image tends to be less good than the fully sampled ones, ii) even if it is possible to obtain an exact CS recovery, the quality of the recovered US images is at most equivalent to those acquired using standard schemes and as described in section 1.4. Their quality is one of the open challenges US imaging is facing nowadays.

In the next subsection, we will present the deconvolution technique as one of the main post-processing approaches in US imaging for image quality enhancement.

2.2 Deconvolution

Deconvolution, also called *deblurring*, is a widely used technique in signal and image processing. It represents a valuable tool that can be used for improving image quality without requiring complicated calibrations of the real-time image acquisition and processing systems. Since the first proposition of convolution model for US images in 1980 (see [Fatemi 1980]), deconvolution methods have been intensively considered to enhance the quality of US images.

2.2.1 Problem Formulation

Based on the first order Born approximation, the US RF image is assumed to follow a 2D convolution model as below [Jensen 1992, Ng 2007b]:

$$\boldsymbol{r} = H\boldsymbol{x} + \boldsymbol{n} \tag{2.20}$$

where $\boldsymbol{r} \in \mathbb{R}^N$ represents hereby an RF US image, *i.e.* the observation from the acquisition device in a general case, $H \in \mathbb{R}^{N \times N}$ is a Block Circulant with Circulant Block (BCCB) matrix related to the 2D PSF of the system and $\boldsymbol{x} \in \mathbb{R}^N$ represents the lexicographically ordered Tissue Reflectivity Function (TRF) [Jensen 1991], *i.e.* the image to be recovered. $\boldsymbol{n} \in \mathbb{R}^N$ is a zero-mean additive white Gaussian noise with variance σ^2. Since BCCB matrices are diagonalized using the 2-D Discrete Fourier Transform (DFT), (2.20) can be expressed in the discrete frequency domain which is very useful for practical computation.

The objective of the deconvolution is to recover $\boldsymbol{x}$ from $\boldsymbol{r}$. It is not an easy task because i) it is an ill-posed inverse problem and consequently requires proper incorporation of prior knowledge about the TRF $\boldsymbol{x}$ into the restoration process, ii) the PSF is usually unknown. The methods assuming the PSF known are categorized as non-blind deconvolution, in opposition to blind deconvolution where the PSF is jointly estimated with $\boldsymbol{x}$. In the next subsection, we will first assume the PSF known and discuss about the regularizations and corresponding existing non-blind deconvolution algorithms.

2.2.2 Regularization and recovery algorithms

Regularization should be incorporated into the deconvolution problem because of its ill-posedness. Thus, the TRF can be estimated by solving the minimization problem below

$$\min_{\boldsymbol{x}\in\mathbb{R}^N} \quad P(\boldsymbol{x}) \quad \text{subject to} \quad \| \boldsymbol{r} - H\boldsymbol{x} \|_2^2 \leq \kappa \tag{2.21}$$

where $P(\boldsymbol{x})$ is the regularization term and κ is an "SNR-dependent" hyper-parameter. The corresponding unconstrained form of this minimization problem is

$$\min_{\boldsymbol{x}\in\mathbb{R}^N} \quad \alpha P(\boldsymbol{x}) + \| \boldsymbol{r} - H\boldsymbol{x} \|_2^2 \tag{2.22}$$

where α is called the regularization parameter.

From a statistical point of view, in the case of Gaussian distributed noise, this minimization problem is also a Maximum A Posteriori (MAP) estimation which stands for maximizing the log-posterior distribution $ln(p(\boldsymbol{x}|\boldsymbol{r}))$. According to the Bayes' rule

$$p(\boldsymbol{x}|\boldsymbol{r}) \propto p(\boldsymbol{r}|\boldsymbol{x})p(\boldsymbol{x}) \tag{2.23}$$

The form of $p(\boldsymbol{x})$ defines the prior probability distribution related to the expression of $P(\boldsymbol{x})$ and has a direct impact on the solution obtained. In this context, the common approach is to adopt an appropriate prior distribution $p(\boldsymbol{x})$ which can make the deconvolved images meet some visual quality requirements at a reasonable computational expense. The goal of deconvolution is indeed to restore higher quality information on the tissues, to be exploited for its characterization or visual analysis. We will remind several regularization terms adopted in the literature of US deconvolution.

2.2.2.1 Gaussian prior

Wiener filter was the very first deconvolution technique applied to US imaging [Fatemi 1980, Liu 1983, Robinson 1984]. The TRF was supposed to be Gaussian distributed and an ℓ_2-norm, also called *Tikhonov regularization*, was employed as below.

$$P(\boldsymbol{x}) = \| \boldsymbol{x} \|_2^2 \tag{2.24}$$

Then the analytical solution to (2.22) is

$$\hat{\boldsymbol{x}} = \frac{H^T}{H^T H + \alpha I}\boldsymbol{r} = f(H, \alpha)\boldsymbol{r} \tag{2.25}$$

where $I \in \mathbb{R}^{N\times N}$ is the identity matrix and $f(H, \alpha)$ stands for the Wiener filtering which is related to the PSF and the regularization parameter α. An appropriate choice of α is necessary to guarantee the balance between data fidelity and smoothness of the deconvolution result. It can be found empirically or assumed equal to the ratio between the squared spectrum of the noise and the squared spectrum of the signal, as in [Taxt 1995, Taxt 1997, Taxt 2001b]. However, it can also be estimated from the recorded data in a Bayesian framework [Jirik 2008] or with some other deterministic approaches like the Constrained least squares (CLS) [Hunt 1973], the Degree of freedom (EDF) [Wahba 1983], the Mean square error (MSE) based method [Galatsanos 1992], the predictive mean square error (PMSE) based method [Hall 1987] and the Generalized Stein's unbiased risk estimate (GSURE) [Eldar 2009]. Particularly, the method of Generalized cross-validation (GCV) [Golub 1979] and the one based on marginal likelihood (ML) [Galatsanos 1992] do not require any information about the SNR. All these methods including the ratio between the squared spectrum of the noise and the squared spectrum of the signal (denoted by 1/SNR) are compared in Fig. 2.5. More simulation results for the comparison of these methods in the context of Wiener filtering can be found in [Chen 2015c].

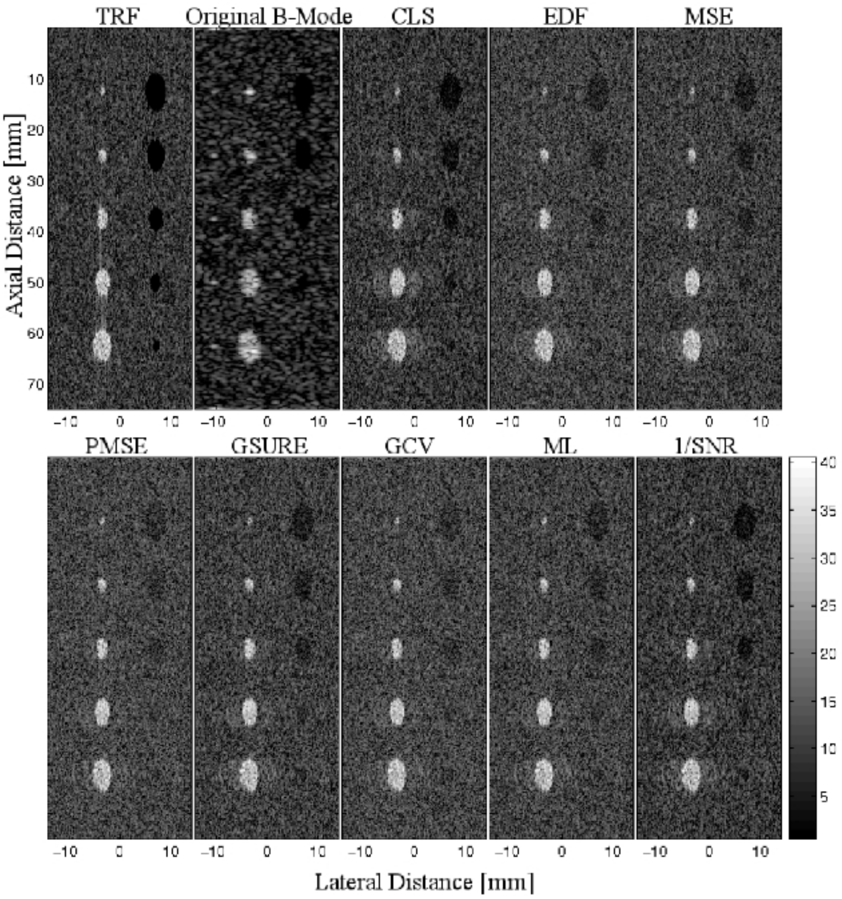

Figure 2.5: Results from [Chen 2015c]. SNR=30dB. From left to right, the images are Cyst phantom tissue reflectivity function, Cyst phantom B-mode US image and its deconvolution results (B-mode visualisation).

The main shortcoming of this method, however, is the Gibbs-like artifacts, which are usually produced by the filter near edge-shaped structures within the TRF $\boldsymbol{x}$. Moreover, because of its linearity, the Wiener filter is not able to interpolate the information lost in the process of image formation. As a result, the Wiener solutions are frequently over smoothed.

2.2.2.2 Laplacian prior

In the case when the samples of the reflectivity function are assumed to be independent, zero-mean random variables obeying the Laplacian distribution (corresponding to the assumption of "sparse tissue"), the regularization term is an ℓ_1-norm [Michailovich 2005, Michailovich 2007, Yu 2012].

$$P(\boldsymbol{x}) = \| \boldsymbol{x} \|_1 \tag{2.26}$$

The results in these works have shown that the sparse prior can produce a superior gain in resolution and contrast compared to the Gaussian prior. In [Michailovich 2005, Michailovich 2007], the authors used *truncated* Newton method to solve the unconstrained ℓ_1-minimization problem in (2.22). They have also pointed out the possibility to apply Conic Programming for the constraint equation (2.21).

In addition, in general image deconvolution [Bolte 2010, Repetti 2015], the proximal forward-backward (PFB) algorithm [Combettes 2005, Combettes 2011, Chouzenoux 2013, Raguet 2013, Bolte 2014], also called proximal gradient method, has been employed to solve this unconstrained ℓ_1-minimization problem.

More interestingly, the deconvolution problem actually becomes a convex sparse recovery problem as described in section 2.1.3.2. It is therefore possible to employ any existing algorithm to get the solution of (2.21) or (2.22).

2.2.2.3 General Gaussian Distribution

Although the previous statistical models are sufficient for achieving appreciable visual quality improvements in some applications, they are not flexible enough to describe a general tissue response. As a consequence, the use of these techniques may introduce a bias in the solutions which may distort important structural features that should be preserved in a tissue characterization context. In this context, the authors in [Alessandrini 2011b] proposed to model the TRF with a Generalized Gaussian Distribution (GGD), previously used for simulating the TRF in [Michailovich 2003]. The GGD probability distribution function (PDF) is

$$p(x_i) = a \exp(-|\frac{x_i}{b}|^p) \tag{2.27}$$

where p is the shape parameter, $b = \sigma_x\sqrt{\Gamma(1/p)/\Gamma(3/p)}$ is the scale parameter, σ_x is the standard deviation, $a = p/(2b\Gamma(1/p))$ is the normalization term and $\Gamma(\,\cdot\,)$ is the Gamma function. Note that Gaussian and Laplacian distributions are also included as special cases of GGD corrsponding to $p = 2$ and $p = 1$, respectively. For a MAP estimate, the regularization term becomes:

$$P(\boldsymbol{x}) = \parallel \boldsymbol{x} \parallel_p^p \tag{2.28}$$

where $p > 0$. Aside from the methods mentioned in section 2.1.3.3, this ℓ_p-minimization problem can also be solved in an expectation maximization (EM) framework [Alessandrini 2011b, Alessandrini 2011a] or a Bayesian framework [Zhao 2014, Zhao 2016].

Moreover, with the growing popularity of proximal operator (defined as below) [Pesquet 2012, Pustelnik 2011, Pustelnik 2012], the Proximal Forward Backward (PFB) algorithm mentioned above is able to solve efficiently (2.22) with an ℓ_p prior term. Compared to the EM algorithm and Bayesian based method, it is faster.

Since we will use this method in the next chapter, we hereby give the details of PFB. Let $f_1(\boldsymbol{x}) = \alpha \parallel \boldsymbol{x} \parallel_p^p$ and $f_2(\boldsymbol{x}) = \parallel \boldsymbol{r} - \boldsymbol{H}\boldsymbol{x} \parallel_2^2$, the PFB for deconvolution is shown in Algorithm 1.

Algorithm 1 PFB algorithm

```
Input: $\boldsymbol{x}_0$, $\alpha$, $t_0$
while not converged do
    $\boldsymbol{g}_n \leftarrow \boldsymbol{x}_n - t_n \nabla f_2(\boldsymbol{x})$                ▷ Forward step
    $\boldsymbol{x}_{n+1} \leftarrow prox_{t_0 \alpha \parallel \cdot \parallel_p^p}(\boldsymbol{g}_n)$     ▷ Backward step
end while
Output: $\boldsymbol{x}$
```

where $t_n > 0$ is step size, set to a constant or determined by line search. *prox* stands for the proximal operator. The proximal operator of a function f is defined for $x^0 \in \mathbb{R}^N$ by:

$$prox_f(x^0) = \underset{x \in \mathbb{R}^N}{argmin} \quad f(x) + \frac{1}{2} \parallel x - x^0 \parallel_2^2 \tag{2.29}$$

When $f = K|x|^p$, the corresponding proximal operator has been given by [Combettes 2011]:

$$prox_{K|x|^p}(x^0) = sign(x^0)q \tag{2.30}$$

where $q \geqslant 0$ and

$$q + pKq^{p-1} = \left|x^0\right| \tag{2.31}$$

It is obvious that the proximal operator of $K\,|x|$ is a soft thresholding as mentioned in section 2.1.3.2, which is equal to:

$$prox_{K|x|}(x^0) = max\left\{\left|x^0\right| - K, 0\right\} \frac{x^0}{|x^0|} \tag{2.32}$$

When $p \neq 1$, we can use Newton's method to obtain its numerical solution, *i.e.* the value of q.

In fact, when $p = 1$, the PFB algorithm becomes the IST method as mentioned in section 2.1.3.2.

To conclude about the three kinds of regularization terms described above, we herein give a comparison result based on an *in vivo* US image, see Fig. 2.6.

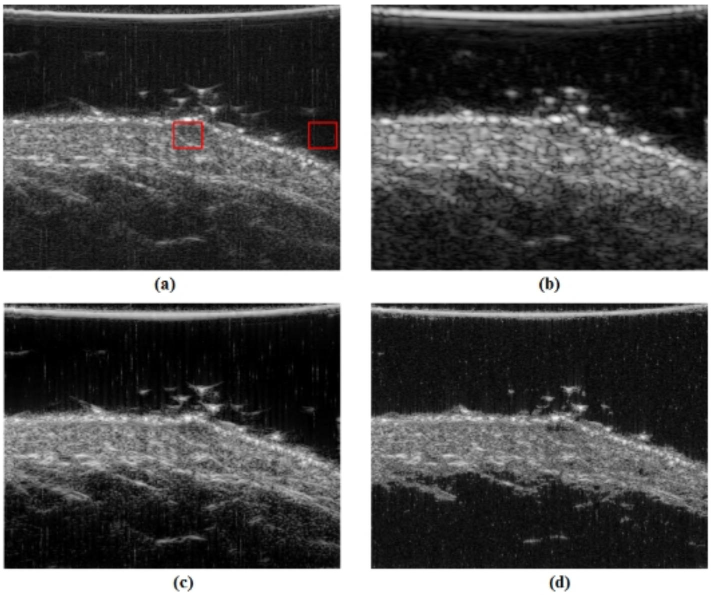

Figure 2.6: Results from [Zhao 2016]. (a) Observed B-mode image, (b) restored B-mode images with ℓ_2-norm, (c) ℓ_1-norm and (d) ℓ_p-norm.

2.2.2.4 Total Variation

Another deeply explored regularization term used in deconvolution is the Total Variation (TV). It is frequently used for piece-wise constant image deconvolution because of its edge-preserving property by not over-penalizing discontinuities in the image while imposing smoothness [Chan 1998, Chambolle 2004, Beck 2009b, Babacan 2009]. However, recently, it has also been adopted for B-mode US image deconvolution [Morin 2012, Morin 2013b]. The TV is defined as

$$TV(\boldsymbol{x}) = \sum_i \sqrt{(\Delta_i^h(\boldsymbol{x}))^2 + (\Delta_i^v(\boldsymbol{x}))^2} \tag{2.33}$$

where the operators $\Delta_i^h(\boldsymbol{x})$ and $\Delta_i^v(\boldsymbol{x})$ correspond to, respectively, the horizontal and vertical first order differences at pixel i. Various kinds of methods could be used to solve the TV regularized deconvolution problem such as the Fast IST algorithm (FISTA) [Beck 2009b] and the Bayesian method in [Babacan 2009]. The authors in [Ng 2010, Morin 2012, Morin 2013b] employed TV in both deconvolution and super-resolution problems and using alternative direction method of multipliers (ADMM) framework to get the solution.

2.2.3 Blind deconvolution

The deconvolution minimization problem in (2.21) or (2.22) assumes that the PSF is known. In this subsection, we will discuss the existing blind deconvolution in which the PSF is supposed to be unknown, which is obviously the case in most practical situations.

So far, two kinds of blind deconvolution methods have been commonly applied to both fields of general and ultrasound imaging [Campisi 2007]: the first is called a *priori* blur identification methods in which the PSF is identified separately from the observed image and later used in combination with one of the non-blind deconvolution algorithms as described above, the second is called joint identification methods which estimate the image and the PSF simultaneously.

2.2.3.1 A *priori* blur identification methods

In this category, the PSF H and the TRF $\boldsymbol{x}$ are estimated separately and sequentially. Since the $\boldsymbol{x}$-estimation part has been introduced in the previous subsection, here we only focus on the H-estimation part.

One class of algorithms is the parametric ones which explicitly model the PSF with a stochastic or deterministic model. For example, in [Jensen 1993, Jensen 1994a, Rasmussen 1994], the authors employed the *autoregressive moving average* (ARMA) model related to the theory of system identification and the PSF is recovered by estimating the ARMA parameters. In these methods, 1-D deconvolution only along the axial direction was applied.

The other class is the nonparametric algorithms. In [Abeyratne 1995], the proposed *high-order spectra* (HOS) based approach is shown to be less sensitive to measurement noises. Being noniterative, it offers some computational advantages and has been used for both axial and lateral deconvolution of RF images. However, the extension to higher-dimensional cases seems not practical. In [Jensen 1994b], the approach in the framework of *homomorphic signal processing* was firstly introduced followed by some substantial developments in [Taxt 1997]. The idea is to take the logarithm of the signal and convert the convolution into sums of their *cepstra*, for linear separation. In this context, a few *cepstrum-based* methods like [Taxt 1995, Taxt 2001a, Taxt 2001b, Jiřík 2006] have been demonstrated to result into accurate estimation and efficient computation. In particular, the *phase unwrapping* problem which concerns the estimation of the Fourier transform phase of the PSF exists in these cepstrum-based methods and is a very difficult reconstruction problem. The authors in [Michailovich 2004] then proposed a way to solve it and generalized the main concepts of homomorphic deconvolution in [Michailovich 2005] combining it with the outlier resistant denoising [Michailovich 2003]. Due to its accuracy, in the next two chapters presenting the work done during this PhD thesis, we employed this PSF estimation method proposed in [Michailovich 2005].

2.2.3.2 Joint identification methods

A different category of blind deconvolution approaches is to estimate the PSF H and TRF $\boldsymbol{x}$ simultaneously. One such method was presented in [Michailovich 2007], where the recovery of H and $\boldsymbol{x}$ is based on linear *inverse filtering*. Most of the methods in this category for both general image processing and US imaging, however, are to estimate the PSF and image of interest by solving the following problem:

$$\min_{\boldsymbol{x}\in\mathbb{R}^N,\boldsymbol{h}\in\mathbb{R}^n} \quad \alpha P(\boldsymbol{x}) + \gamma P(\boldsymbol{h}) + \parallel \boldsymbol{r} - H\boldsymbol{x} \parallel_2^2 \tag{2.34}$$

where $\boldsymbol{h} \in \mathbb{R}^n$ represents the PSF with a support of size n, $P(\boldsymbol{h})$ is the regularization term containing prior information on the PSF. The authors in [Molina 2006, Babacan 2009, Zhao 2015] solved this problem in a Bayesian framework. While in [Almeida 2010, Yu 2012, Morin 2013b], the *alternative minimization* (AM) method have been used to solve this non-convex problem.

2.2.4 Conclusion

Deconvolution has a long story in US imaging since 1980s. It is mainly devoted to overcoming one of the disadvantage of US imaging, the image quality. All the research works, including the prior assumptions made for TRF, the PSF estimation, the non-blind deconvolution algorithms and the blind deconvolution, have made it possible to enhance the quality of US images in a post-processing stage. In the next subsection, we will introduce the contributions of this thesis combining the deconvolution and CS as described in the previous subsection.

2.3 Contributions

The objective of this thesis is to meet with two challenges in US imaging mentioned in Chapter 1, *i.e.*, to obtain a higher frame rate or less data volume and enhance the image quality at the same time.

We thus first propose a framework called compressive deconvolution in US imaging. Compressive deconvolution, called also CS deblurring, has recently been studied in general-purpose image processing [Ma 2009, Xiao 2011, Zhao 2010, Amizic 2013, Spinoulas 2012]. To our knowledge, our work is the first attempt of addressing the compressive deconvolution problem in US imaging. The direct model is

$$\boldsymbol{y} = \Phi H\boldsymbol{x} + \boldsymbol{n} \tag{2.35}$$

Inverting the model in 2.35 will allow us to estimate the TRF $\boldsymbol{x}$ from the compressed RF measurements $\boldsymbol{y}$. We then formulate the reconstruction process into an optimization problem.

In Chapter 3 and Chapter 4, we propose two novel algorithms to find its optimal solution. Opposed to these contributions, in which the PSF is supposed to be known or estimated in a preceding stage, in Chapter. 5, we will present some preliminary results with joint PSF estimation. Conclusions and perspectives will be done in the last chapter.

Chapter 3

Compressive Deconvolution using ADMM

Part of the work in this chapter has been published in [Chen 2015a], [Chen 2015b] and [Chen 2016a].

Contents

3.1 Introduction

As introduced in the previous chapter, the direct model of Compressive Deconvolution is as follows:

$$\boldsymbol{y} = \Phi H \boldsymbol{x} + \boldsymbol{n} \tag{3.1}$$

where the variables $\boldsymbol{y} \in \mathbb{R}^M$ corresponds to the M compressed measurements, $\Phi \in \mathbb{R}^{M\times N}$ represents the sampling matrix, $H \in \mathbb{R}^{N\times N}$ is a BCCB matrix related to the 2D PSF of the system, $\boldsymbol{x} \in \mathbb{R}^N$ represents the TRF and $\boldsymbol{n}$ is a zero-mean additive white Gaussian noise. Inverting the model in (3.1) will allow us to estimate the TRF $\boldsymbol{x}$ from the compressed RF measurements $\boldsymbol{y}$.

In the general-purpose image processing literature, a few methods have been already proposed aiming at solving (3.1) [Hegde 2009, Hegde 2011, Zhao 2010, Ma 2009, Xiao 2011, Amizic 2013, Spinoulas 2012]. In [Hegde 2009, Hegde 2011, Zhao 2010], the authors assumed $\boldsymbol{x}$ was sparse in the direct or image domain and the PSF was unknown. In [Hegde 2009, Hegde 2011], a study on the number of measurements lower bound is presented, together with an algorithm to estimate the PSF and $\boldsymbol{x}$ alternatively. The authors in [Zhao 2010] solved the compressive deconvolution problem using an ℓ_1-norm minimization algorithm by making use of the "all-pole" model of the autoregressive process. In [Ma 2009, Xiao 2011], $\boldsymbol{x}$ was considered sparse in a transformed domain and the PSF was supposed known. An algorithm based on Poisson singular integral and iterative curvelet thresholding was shown in [Ma 2009]. The authors in [Xiao 2011] further combined the curvelet regularization with total variation to improve the performance in [Ma 2009]. Finally, the methods in [Amizic 2013, Spinoulas 2012] supposed the blurred signal $\boldsymbol{r} = H\boldsymbol{x}$ was sparse in a transformed domain and the PSF unknown. They proposed a compressive deconvolution framework that relies on a constrained optimization technique allowing to exploit existing CS reconstruction algorithms.

3.2 Optimization Problem Formulation

3.2.1 Sequential approach

In order to estimate the TRF $\boldsymbol{x}$ from the compressed and blurred measurements $\boldsymbol{y}$, an intuitive idea to invert the direct model in (3.1) is to proceed through two sequential steps. The aim of the first step is to recover the blurred US RF image $\boldsymbol{r} = H\boldsymbol{x}$ from the compressed measurements $\boldsymbol{y}$ by solving the following optimization problem or the constrained one as (2.17):

$$\underset{\boldsymbol{a}\in\mathbb{R}^N}{min} \; \|\boldsymbol{a}\|_1 + \frac{1}{2\mu}\|\boldsymbol{y} - \Phi\Psi\boldsymbol{a}\|_2^2 \tag{3.2}$$

where $\boldsymbol{a}$ is the sparse representation of the US RF image $\boldsymbol{r}$ in the transformed domain Ψ, that is, $\boldsymbol{r} = H\boldsymbol{x} = \Psi\boldsymbol{a}$. Different basis have been shown to provide good results in the application of CS in US imaging, such as wavelets, waveatoms or 2D Fourier basis [Liebgott 2012]. In this chapter the wavelet transform has been employed.

Once the blurred RF image, denoted by $\hat{\boldsymbol{r}}$, is recovered by solving the convex problem in (3.2), one can restore the TRF $\boldsymbol{x}$ by minimizing:

$$\min_{\boldsymbol{x}\in\mathbb{R}^N} \alpha \|\boldsymbol{x}\|_p^p + \|\hat{\boldsymbol{r}} - H\boldsymbol{x}\|_2^2 \tag{3.3}$$

which is a typical deconvolution problem and equivalent to (2.22).

3.2.2 Proposed approach

While the sequential approach represents the most intuitive way to solve the compressive deconvolution problem, dividing a single problem into two separate subproblems will inevitably generate larger estimation errors as shown by the results in section 3.6. Therefore, we propose herein a method to solve the CS and deconvolution problem simultaneously. Similarly to [Amizic 2013], we formulate the reconstruction process into a constrained optimization problem exploiting the relationship between CS recovery (as (3.2)) and deconvolution (as (3.3)).

$$\begin{aligned} &\min_{\boldsymbol{x}\in\mathbb{R}^N, \boldsymbol{a}\in\mathbb{R}^N} \parallel \boldsymbol{a} \parallel_1 + \alpha P(\boldsymbol{x}) + \frac{1}{2\mu} \parallel \boldsymbol{y} - \Phi\Psi\boldsymbol{a} \parallel_2^2 \\ &\quad s.t. \quad H\boldsymbol{x} = \Psi\boldsymbol{a} \end{aligned} \tag{3.4}$$

where α is the hyper-parameter.

Since our goal is to recover enhanced US images by estimating the TRF $\boldsymbol{x}$, we further reformulate the problem above into an unconstrained optimization problem:

$$\min_{\boldsymbol{x}\in\mathbb{R}^N} \quad \parallel \Psi^{-1}H\boldsymbol{x} \parallel_1 + \alpha P(\boldsymbol{x}) + \frac{1}{2\mu} \parallel \boldsymbol{y} - \Phi H\boldsymbol{x} \parallel_2^2 \tag{3.5}$$

where $P(\boldsymbol{x})$ represents the prior information of $\boldsymbol{x}$. The objective function in (3.5) contains, in addition to the data fidelity term, two regularization terms. The first one aims at imposing the sparsity of the RF data $H\boldsymbol{x}$ (i.e. minimizing the ℓ_1-norm of the target image $\boldsymbol{x}$ convolved with a bandlimited function) in a transformed domain Ψ. We should note that such an assumption has been extensively used in the application of CS in US imaging. Transformations such as 2D Fourier, wavelet or wave atoms have been shown to provide good results in US imaging (see section 2.1.4.1). The second term $P(\boldsymbol{x})$ represents the priori information of the target image $\boldsymbol{x}$. We will employ the ℓ_p-norm where the shape parameter related to the GGD is ranging from 1 to 2 ($1 \leq p \leq 2$), allowing us to generalize the existing works in US image deconvolution mainly based on Laplacian or Gaussian statistics as described in section. 2.2.2. While our main contribution is given for the case when this term is equal to $\parallel \boldsymbol{x} \parallel_p^p$ (adapted to US images), our approach using a generalized total variation regularization will also

(a) (b) (c)

Figure 3.1: Sparsity comparison of $\boldsymbol{x}$ and $H\boldsymbol{x}$ in wavelet domain. (a) A random scatterer map (TRF, denoted by $\boldsymbol{x}$) generated according to a zero-mean Generalized Gaussian distribution and (b) its corresponding blurred version (RF data, denoted by $H\boldsymbol{x}$), obtained by convolving the TRF with an US PSF.(c) the magnitude decay rates of the sorted wavelet coefficients, calculated for $\boldsymbol{x}$ and $H\boldsymbol{x}$.

detailed in this chapter and may be useful for other (medical) applications.

We notice that our regularized reconstruction problem based on the objective function in (3.5) is different from a typical CS reconstruction. Specifically, the objective function of a standard CS technique applied to our model would only contain the classical data fidelity term and an ℓ_1-norm penalty similar to the first term in (3.5) but without the operator H, shown as below:

$$\underset{\boldsymbol{x}\in\mathbb{R}^N}{min} \quad \| \boldsymbol{x} \|_1 + \frac{1}{2\mu} \| \boldsymbol{y} - \Phi H \boldsymbol{x} \|_2^2 \tag{3.6}$$

However, it would not take fully advantage of the prior information we may inject in the reconstruction process, *i.e.*, the sparsity of $H\boldsymbol{x}$ in a given transformation and the generalized Gaussian distributed $\boldsymbol{x}$. Moreover, blurred signals usually exhibit faster decay rates for the magnitude of their wavelet coefficients than their respective original versions. In Fig.3.1, we analyze the effect of blurring on the decay rates of the magnitude of the sorted wavelet coefficients for a random scatterer map. In addition, such a CS reconstruction is not adapted to compressive deconvolution, mainly because the requirements of CS theory such as the RIP might not be guaranteed [Amizic 2013].

3.3 Basics of Alternating Direction Method of Multipliers

Before going into the details of our algorithm, we report in this paragraph the basics of ADMM. ADMM has been extensively studied in the areas of convex programming and variational inequalities, e.g., [Boyd 2011]. The general optimization problem considered in ADMM framework is as follows:

$$\begin{aligned} \underset{\boldsymbol{u},\boldsymbol{v}}{min} \quad & f(\boldsymbol{u}) + g(\boldsymbol{v}) \\ s.t. \quad & B\boldsymbol{u} + C\boldsymbol{v} = \boldsymbol{b}, \boldsymbol{u} \in \mathcal{U}, \boldsymbol{v} \in \mathcal{V} \end{aligned} \tag{3.7}$$

where $\mathcal{U} \subseteq \mathbb{R}^s$ and $\mathcal{V} \subseteq \mathbb{R}^t$ are given convex sets, $f : \mathcal{U} \to \mathbb{R}$ and $g : \mathcal{V} \to \mathbb{R}$ are closed convex functions, $B \in \mathbb{R}^{r\times s}$ and $C \in \mathbb{R}^{r\times t}$ are given matrices and $\boldsymbol{b} \in \mathbb{R}^r$ is a given vector.

By attaching the Lagrangian multiplier $\boldsymbol{\lambda} \in \mathbb{R}^r$ to the linear constraint, the Augmented Lagrangian (AL) function of (3.7) is

$$\mathcal{L}(\boldsymbol{u}, \boldsymbol{v}, \boldsymbol{\lambda}) = f(\boldsymbol{u}) + g(\boldsymbol{v}) - \boldsymbol{\lambda}^t(B\boldsymbol{u} + C\boldsymbol{v} - \boldsymbol{b}) + \frac{\beta}{2} \parallel B\boldsymbol{u} + C\boldsymbol{v} - \boldsymbol{b} \parallel_2^2 \tag{3.8}$$

where $\beta > 0$ is the penalty parameter for the linear constraints to be satisfied. The standard ADMM framework follows the three steps iterative process:

$$\begin{cases} \boldsymbol{u}^{k+1} \in \underset{\boldsymbol{u}\in\mathcal{U}}{argmin} \mathcal{L}(\boldsymbol{u}, \boldsymbol{v}^k, \boldsymbol{\lambda}^k) \\ \boldsymbol{v}^{k+1} \in \underset{\boldsymbol{v}\in\mathcal{V}}{argmin} \mathcal{L}(\boldsymbol{u}^{k+1}, \boldsymbol{v}, \boldsymbol{\lambda}^k) \\ \boldsymbol{\lambda}^{k+1} = \boldsymbol{\lambda}^k - \beta(B\boldsymbol{u}^{k+1} + C\boldsymbol{v}^{k+1} - \boldsymbol{b}) \end{cases} \tag{3.9}$$

The main advantage of ADMM, in addition to the relative easy of implementation, is its ability to split awkward intersections and objectives to easy subproblems, resulting into iterations comparable to those of other first-order methods.

3.4 Proposed ADMM parameterization

In this subsection, we propose an ADMM method for solving the ultrasound compressive deconvolution problem in (3.5).

Using a trivial variable change, the minimization problem in (3.5) can be rewritten as:

$$\underset{\boldsymbol{x}\in\mathbb{R}^N}{min} \parallel \boldsymbol{w} \parallel_1 + \alpha P(\boldsymbol{x}) + \frac{1}{2\mu} \parallel \boldsymbol{y} - A\boldsymbol{a} \parallel_2^2 \tag{3.10}$$

where $\boldsymbol{a} = \Psi^{-1}H\boldsymbol{x}$, $\boldsymbol{w} = \boldsymbol{a}$ and $A = \Phi\Psi$. Let us denote $\boldsymbol{z} = \begin{bmatrix} \boldsymbol{w} \\ \boldsymbol{x} \end{bmatrix}$. The reformulated problem in (3.10) can fit the general ADMM framework in (3.7) by choosing: $f(\boldsymbol{a}) = \frac{1}{2\mu} \parallel \boldsymbol{y} - A\boldsymbol{a} \parallel_2^2$, $g(\boldsymbol{z}) = \parallel \boldsymbol{w} \parallel_1 + \alpha P(\boldsymbol{x})$, $B = \begin{bmatrix} I_N \\ \Psi \end{bmatrix}$, $C = \begin{bmatrix} -I_N & \mathbf{0} \\ \mathbf{0} & -H \end{bmatrix}$ and $\boldsymbol{b} = \mathbf{0}$. $I_N \in \mathbb{R}^{N\times N}$ is the identity matrix.

The AL function of (3.10) is then given by

$$\mathcal{L}(\boldsymbol{a},\boldsymbol{z},\boldsymbol{\lambda}) = f(\boldsymbol{a}) + g(\boldsymbol{z}) - \boldsymbol{\lambda}^t(B\boldsymbol{a} + C\boldsymbol{z}) + \frac{\beta}{2} \parallel B\boldsymbol{a} + C\boldsymbol{z} \parallel_2^2 \tag{3.11}$$

where $\boldsymbol{\lambda} \in \mathbb{R}^{2N}$ stands for $\boldsymbol{\lambda} = \begin{bmatrix} \boldsymbol{\lambda}_1 \\ \boldsymbol{\lambda}_2 \end{bmatrix}$, $\boldsymbol{\lambda}_i \in \mathbb{R}^N (i = 1, 2)$. According to the standard ADMM iterative scheme, the minimizations with respect to $\boldsymbol{a}$ and $\boldsymbol{z}$ will be performed alternatively, followed by the update of $\boldsymbol{\lambda}$.

3.5 Implementation Details

In this subsection, we detail each of the three steps of our ADMM-based compressive deconvolution method.

Step 1 consists in solving the $\boldsymbol{z}$-problem as below.

$$\boldsymbol{z}^k = \underset{\boldsymbol{z} \in \mathbb{R}^{2N}}{argmin} \quad g(\boldsymbol{z}) - (\boldsymbol{\lambda}^{k-1})^t(B\mathbf{a}^{k-1} + C\boldsymbol{z}) + \frac{\beta}{2} \parallel B\boldsymbol{a}^{k-1} + C\boldsymbol{z} \parallel_2^2 \tag{3.12}$$

Since $\boldsymbol{z} = \begin{bmatrix} \boldsymbol{w} \\ \boldsymbol{x} \end{bmatrix}$, this $\boldsymbol{z}$-problem can be further divided into two subproblems.

Step 1.1 aims at solving:

$$\begin{aligned} \boldsymbol{w}^k =& \underset{\boldsymbol{w} \in \mathbb{R}^N}{argmin} \quad \parallel \boldsymbol{w} \parallel_1 - (\boldsymbol{\lambda}_1^{k-1})^t(\mathbf{a}^{k-1} - \boldsymbol{w}) + \frac{\beta}{2} \parallel \boldsymbol{a}^{k-1} - \boldsymbol{w} \parallel_2^2 \\ \Leftrightarrow \boldsymbol{w}^k =& \underset{\boldsymbol{w} \in \mathbb{R}^N}{argmin} \parallel \boldsymbol{w} \parallel_1 + \frac{\beta}{2} \parallel \boldsymbol{a}^{k-1} - \boldsymbol{w} - \frac{\boldsymbol{\lambda}_1^{k-1}}{\beta} \parallel_2^2 \\ \Leftrightarrow \boldsymbol{w}^k =& prox_{\parallel \cdot \parallel_1 / \beta} \left(\boldsymbol{a}^{k-1} - \frac{\boldsymbol{\lambda}_1^{k-1}}{\beta} \right) \end{aligned} \tag{3.13}$$

where *prox* stands for the proximal operator as proposed in [Pesquet 2012, Pustelnik 2011, Pustelnik 2012]. The proximal operators of various kinds of functions including $\|\boldsymbol{x}\|_p^p$ have been given explicitly in the literature (see e.g. [Combettes 2011]). Basics about the proximal operator of $\|\boldsymbol{x}\|_p^p$ have been reminded in Section.2.2.2.3.

Step 1.2 consists in solving:

$$\boldsymbol{x}^k = \underset{\boldsymbol{x} \in \mathbb{R}^N}{argmin} \quad \alpha P(\boldsymbol{x}) - \boldsymbol{\lambda}_2^{k-1}(\Psi \boldsymbol{a}^{k-1} - H\boldsymbol{x}) + \frac{\beta}{2} \parallel \Psi \boldsymbol{a}^{k-1} - H\boldsymbol{x} \parallel_2^2 \tag{3.14}$$

Step 1.2a Being adapted to US images, $P(\boldsymbol{x}) = \parallel \boldsymbol{x} \parallel_p^p$. For p equal to 2, the minimization in (3.14) can be easily solved in the Fourier domain, as follows:

$$\boldsymbol{x}^k = \left[\beta H^t H + 2\alpha I_N\right]^{-1} \times \left[\beta H^t \Psi \boldsymbol{a}^{k-1} - H^t \boldsymbol{\lambda}_2^{k-1}\right] \tag{3.15}$$

For $1 \leqslant p < 2$, we propose to use the proximal operator to solve (3.14). In this case, (3.14) will be equivalent to

$$\boldsymbol{x}^k = \underset{\boldsymbol{x}\in\mathbb{R}^N}{argmin} \quad \alpha \parallel \boldsymbol{x} \parallel_p^p + \frac{\beta}{2} \parallel \Psi \boldsymbol{a}^{k-1} - H\boldsymbol{x} - \frac{\boldsymbol{\lambda}_2^{k-1}}{\beta} \parallel_2^2 \tag{3.16}$$

Denoting $h(\boldsymbol{x}) = \frac{1}{2} \parallel \Psi \boldsymbol{a}^{k-1} - H\boldsymbol{x} - \frac{\boldsymbol{\lambda}_2^{k-1}}{\beta} \parallel_2^2$, we can further approximate $h(\boldsymbol{x})$ by

$$h'(\boldsymbol{x}^{k-1})(\boldsymbol{x} - \boldsymbol{x}^{k-1}) + \frac{1}{2\gamma} \parallel \boldsymbol{x} - \boldsymbol{x}^{k-1} \parallel_2^2 \tag{3.17}$$

where $\gamma > 0$ is a parameter related to the Lipschitz constant [Chouzenoux 2014] and $h'(\boldsymbol{x}^{k-1})$ is the gradient of $h(\boldsymbol{x})$ when $\boldsymbol{x} = \boldsymbol{x}^{k-1}$, which is equal to

$$h'(\boldsymbol{x}^{k-1}) = H^t(H\boldsymbol{x}^{k-1} - \Psi \boldsymbol{a}^{k-1} + \frac{\boldsymbol{\lambda}_2^{k-1}}{\beta}) \tag{3.18}$$

By plugging (3.17) into (3.16), we obtain:

$$\begin{aligned} \boldsymbol{x}^k &\approx \underset{\boldsymbol{x}\in\mathbb{R}^N}{argmin} \quad \alpha \parallel \boldsymbol{x} \parallel_p^p + \beta h'(\boldsymbol{x}^{k-1})(\boldsymbol{x} - \boldsymbol{x}^{k-1}) + \frac{\beta}{2\gamma} \parallel \boldsymbol{x} - \boldsymbol{x}^{k-1} \parallel_2^2 \\ \Leftrightarrow \boldsymbol{x}^k &\approx \underset{\boldsymbol{x}\in\mathbb{R}^N}{argmin} \quad \alpha \parallel \boldsymbol{x} \parallel_p^p + \frac{\beta}{2\gamma} \parallel \boldsymbol{x} - \boldsymbol{x}^{k-1} + \gamma h'(\boldsymbol{x}^{k-1}) \parallel_2^2 \end{aligned} \tag{3.19}$$

According to the definition of the proximal operator, we can finally get

$$\boldsymbol{x}^k \approx prox_{\alpha\gamma\parallel\cdot\parallel_p^p/\beta}\{\boldsymbol{x}^{k-1} - \gamma h'(\boldsymbol{x}^{k-1})\} \tag{3.20}$$

We should note that (3.20) provides an approximate solution, thus resulting into an inexact ADMM scheme. However, the convergence of such inexact ADMM has been already established in [He 2002, Boyd 2011, Yang 2011].

Step 1.2b For general-purpose or some other image processing, a generalized total variation regularization would be more appropriate. By changing the priori term of the target image $\boldsymbol{x}$, our proposed method is still applicable.

As suggested in [Amizic 2013], the generalized TV is given by:

$$\sum_{d\in D} 2^{1-o(d)} \sum_i \left|\Delta_i^d(\boldsymbol{x})\right|^p \tag{3.21}$$

where $o(d) \in \{1, 2\}$ denotes the order of the difference operator $\Delta_i^d(\boldsymbol{x})$, $0 < p < 1$, and $d \in D = \{h, v, hh, vv, hv\}$. $\Delta_i^h(\boldsymbol{x})$ and $\Delta_i^v(\boldsymbol{x})$ correspond, respectively, to the horizontal and vertical first order differences, at pixel i, that is, $\Delta_i^h(\boldsymbol{x}) = u_i - u_{l(i)}$ and $\Delta_i^v(\boldsymbol{x}) = u_i - u_{a(i)}$, where $l(i)$ and $a(i)$ denote the nearest neighbors of i, to the left and above, respectively. The operators $\Delta_i^{hh}(\boldsymbol{x})$, $\Delta_i^{vv}(\boldsymbol{x})$, $\Delta_i^{hv}(\boldsymbol{x})$ correspond, respectively, to horizontal, vertical and horizontal-vertical second order differences, at pixel i.

Replacing the ℓ_p-norm by the generalized TV in our compressive deconvolution scheme results in a modified $\boldsymbol{x}$ update step, that turns in solving:

$$\boldsymbol{x}^k = \underset{\boldsymbol{x} \in \mathbb{R}^N}{argmin} \quad \alpha \sum_{d \in D} 2^{1-o(d)} \sum_i \left| \Delta_i^d(\boldsymbol{x}) \right|^p - \boldsymbol{\lambda}_2^{k-1}(\Psi \boldsymbol{a}^{k-1} - H\boldsymbol{x}) + \frac{\beta}{2} \parallel \Psi \boldsymbol{a}^{k-1} - H\boldsymbol{x} \parallel_2^2 \tag{3.22}$$

Similarly to the first step of the method in [Amizic 2013], the equation above can be solved iteratively by:

$$\boldsymbol{x}^{k,l} = \left[\beta H^t H + \alpha p \sum_d 2^{1-o(d)} (\boldsymbol{\Delta}^d)^t B_d^{k,l} (\boldsymbol{\Delta}^d) \right]^{-1} \times \left[\beta H^t \Psi \boldsymbol{a}^{k-1} - H^t \boldsymbol{\lambda}_2^{k-1} \right] \tag{3.23}$$

where l is the iteration number in the process of updating $\boldsymbol{x}$, $B_d^{k,l}$ is a diagonal matrix with entries $\boldsymbol{\Delta}^d$ is the convolution matrix (BCCB matrix) of the difference operator $\Delta_i^d(\cdot)$ and $B_d^{k,l}(i,i) = (v_{d,i}^{k,l})$, which is updated iteratively by:

$$v_{d,i}^{k,l+1} = [\Delta_i^d(\boldsymbol{x}^{k,l})]^2 \tag{3.24}$$

When a stopping criterion is met, we can finally get an update of $\boldsymbol{x}$.

Step 2 aims at solving:

$$\begin{aligned} \boldsymbol{a}^k &= \underset{\boldsymbol{a} \in \mathbb{R}^N}{argmin} \quad \frac{1}{2\mu} \parallel \boldsymbol{y} - A\boldsymbol{a} \parallel_2^2 - (\boldsymbol{\lambda}^{k-1})^t (B\boldsymbol{a} + C\boldsymbol{z}^k) \\ &+ \frac{\beta}{2} \parallel B\boldsymbol{a} + C\boldsymbol{z}^k \parallel_2^2 \\ \Leftrightarrow \boldsymbol{a}^k &= (\frac{1}{\mu} A^t A + \beta I_N + \beta \Psi^t \Psi)^{-1} (\frac{1}{\mu} A^t \boldsymbol{y} + \boldsymbol{\lambda}_1^{k-1} + \Psi^t \boldsymbol{\lambda}_2^{k-1} \\ &+ \beta \boldsymbol{w}^k + \beta \Psi^t H \boldsymbol{x}^k) \end{aligned} \tag{3.25}$$

The formula above is equivalent to solving an $N \times N$ linear system or inverting an $N \times N$ matrix. However, since the sparse basis Ψ considered is orthogonal (e.g. the wavelet transform), it can be reduced to solving a smaller $M \times M$ linear system or inverting an $M \times M$ matrix by exploiting the Sherman-Morrison-Woodbury inversion matrix lemma [Deng 2013]:

$$(\beta_1 I_N + \beta_2 A^t A)^{-1} = \frac{1}{\beta_1} I_N - \frac{\beta_2}{\beta_1} A^t (\beta_1 I_M + \beta_2 A A^t)^{-1} A \tag{3.26}$$

In our work, without loss of generality, we considered the compressive sampling matrix Φ as a Structurally Random Matrix (SRM) [Do 2012]. Therefore, A was formed by randomly taking a subset of rows from orthonormal transform matrices, that is, $AA^t = I_M$. As a consequence, there is no need to solve a linear system and the main computational cost consists into two matrix-vector multiplications per iteration.

Step 3 consists in solving:

$$\boldsymbol{\lambda}^k = \boldsymbol{\lambda}^{k-1} - \beta(B\boldsymbol{a}^k + C\boldsymbol{z}^k) \tag{3.27}$$

The proposed optimization routine is summarized in Algorithm 2.

Algorithm 2 Compressive deconvolution ADMM-based algorithm.

```
Input: $\boldsymbol{a}^0$, $\boldsymbol{\lambda}^0$, $\alpha$, $\mu$, $\beta$
while not converged do
    $\boldsymbol{w}^k \leftarrow \boldsymbol{a}^{k-1}, \boldsymbol{\lambda}^{k-1}$        ▷ update $\boldsymbol{w}^k$ using (3.13)
    switch $P(\boldsymbol{x})$ do
        case $P(\boldsymbol{x}) = \sum_{d\in D} 2^{1-o(d)} \sum_i \left|\Delta_i^d(\boldsymbol{x})\right|^p$
            for $l = 1, 2, \ldots$ until a stopping criterion is met do
                $\boldsymbol{x}^{k,l} \leftarrow \boldsymbol{a}^{k-1}, \boldsymbol{\lambda}^{k-1}, v_{d,i}^{k,l}$        ▷ update $\boldsymbol{x}^{k,l}$ using (3.23)
                $v_{d,i}^{k,l+1} \leftarrow \boldsymbol{x}^{k,l}$        ▷ update $v_{d,i}^{k,l+1}$ using (3.24)
            end for
        case $P(\boldsymbol{x}) = \| \boldsymbol{x} \|_p^p$
            $\boldsymbol{x}^k \leftarrow \boldsymbol{a}^{k-1}, \boldsymbol{\lambda}^{k-1}$        ▷ update $\boldsymbol{x}^k$ using (3.15) or (3.20)
    $\boldsymbol{a}^k \leftarrow \boldsymbol{w}^k, \boldsymbol{x}^k, \boldsymbol{\lambda}^{k-1}$        ▷ update $\boldsymbol{a}^k$ using (3.25)
    $\boldsymbol{\lambda}^k \leftarrow \boldsymbol{w}^k, \boldsymbol{x}^k, \boldsymbol{a}^k, \boldsymbol{\lambda}^{k-1}$        ▷ update $\boldsymbol{\lambda}^k$ using (3.27)
end while
Output: $\boldsymbol{x}$
```

3.6 Results

The performance of the proposed compressive deconvolution method are evaluated on several simulated and experimental data sets. First, we evaluate the performance of the proposed approach on a Shepp-Logan phantom compared to the one in [Amizic 2013], referred as CD_Amizic hereafter. Second, we test our algorithm on a modified Shepp-Logan phantom containing speckle noise to confirm that i) the l_p-norm regularization term is more adapted to US images than the generalized TV used in [Amizic 2013], ii) the proposed optimization scheme as (3.5) is more appropriate than a typical CS reconstruction as (3.6). Third, we give the results of our algorithm for different l_p-norm optimizations on simulated US images, showing the superiority of our approach over the intuitive sequential method explained in section 3.1. Finally, compressive deconvolution results on two *in vivo* ultrasound images are presented.

3.6.1 Quantitative evaluation criterions

To evaluate the results quantitatively, we employed three metrics in this chapter. Two of them are for simulated data which has the ground truth and the other is for *in vivo* data.

PSNR The standard peak signal-to-noise ratio (PSNR) is defined as

$$PSNR = 10log_{10}\frac{NL^2}{\parallel \boldsymbol{x} - \hat{\boldsymbol{x}} \parallel^2} \tag{3.28}$$

where $\boldsymbol{x}$ and $\hat{\boldsymbol{x}}$ are the original and reconstructed images, and the constant L represents the maximum intensity value in $\boldsymbol{x}$.

SSIM The Structural Similarity (SSIM) [Wang 2004] is extensively used in US imaging and defined as

$$SSIM = \frac{(2\mu_x\mu_{\hat{x}} + c_1)(2\sigma_{x\hat{x}} + c_2)}{(\mu_x^2 + \mu_{\hat{x}}^2 + c_1)(\sigma_x^2 + \sigma_{\hat{x}}^2 + c_2)} \tag{3.29}$$

where x and $\hat{x}$ are the original and reconstructed images, μ_x, $\mu_{\hat{x}}$, σ_x and $\sigma_{\hat{x}}$ are the mean and variance values of x and $\hat{x}$, $\sigma_{x\hat{x}}$ is the covariance between x and $\hat{x}$; $c_1 = (k_1L)^2$ and $c_2 = (k_2L)^2$ are two variables aiming at stabilizing the division with weak denominator, L is the dynamic range of the pixel-values and k_1, k_2 are constants. Herein, $L = 1$, $k_1 = 0.01$ and $k_2 = 0.03$.

CNR Given that the true TRF is not known in experimental conditions, the quality of the reconstruction results is evaluated using the contrast-to-noise ratio (CNR) [Lyshchik 2005], defined as

$$CNR = \frac{|\mu_1 - \mu_2|}{\sqrt{\sigma_1^2 + \sigma_2^2}} \tag{3.30}$$

where μ_1 and μ_2 are the mean of pixels located in two regions extracted from the image while σ_1 and σ_2 are the standard deviations of the same blocks.

3.6.2 Results on Shepp-Logan phantom

In this subsection we show an experiment aiming to evaluate the performance of the proposed approach compared to CD_Amizic. The comparison results are obtained on the standard 256 × 256 Shepp-Logan phantom. The measurements have been generated in a similar manner as in [Amizic 2013], *i.e.* the original image was normalized, degraded by a $2D$ Gaussian PSF with a 5-pixel variance, projected onto a structured random matrix (SRM) to generate the CS measurements and corrupted by an additive Gaussian noise. We should remark that in [Amizic 2013] the compressed measurements were originally generated using a Gaussian random matrix. However, we have found that the reconstruction results with CD_Amizic are slightly better when using a SRM compared to the PSNR results reported in [Amizic 2013]. Both methods were based on the generalized TV to model the image to be estimated and the 3-level Haar wavelet transform as sparsifying basis Ψ. With our method, the hyperparameters were set to $\{\alpha, \mu, \beta\} = \{10^{-1}, 10^{-5}, 10^{2}\}$. The same hyperparameters as reported in [Amizic 2013] were used for CD_Amizic. Both algorithms based on the non-blind deconvolution (PSF is supposed to be known) and used the same stopping criteria.

Fig.3.2 shows the original Shepp-Logan image, its blurred version and a series of compressive deconvolution reconstructions using both our method and CD_Amizic for CS ratios running from 0.4 to 0.8 and a SNR of 40 dB. Table.3.1 regroups the PSNRs obtained with our method and with CD_Amizic for two SNRs and for four CS ratios from 0.2 to 0.4. In each case, the reported PSNRs are the mean values of 10 experiments. We may observe that our method outperforms CD_Amizic in all the cases, allowing a PSNR improvement in the range of 0.5 to 2 dB. Moreover, Fig.3.3 shows the computational times with CD_Amizic and the proposed method, obtained with Matlab implementations (for CD_Amizic, the original code provided by the authors of [Amizic 2013] has been employed) on a standard desktop computer (Intel Xeon CPU E5620 @ 2.40GHz, 4.00G RAM). We notice that our approach is less time consuming than CD_Amizic for all the CS ratios considered.

Table 3.1: PSNR assessment for Shepp-Logan phantom

SNR	CS ratios	20%	40%	60%	80%
40dB	CD_Amizic	23.04	24.88	25.30	25.51
	Proposed method	**24.09**	**25.38**	**26.26**	**26.91**
30dB	CD_Amizic	22.61	24.05	24.40	24.55
	Proposed method	**23.92**	**25.12**	**25.82**	**26.33**

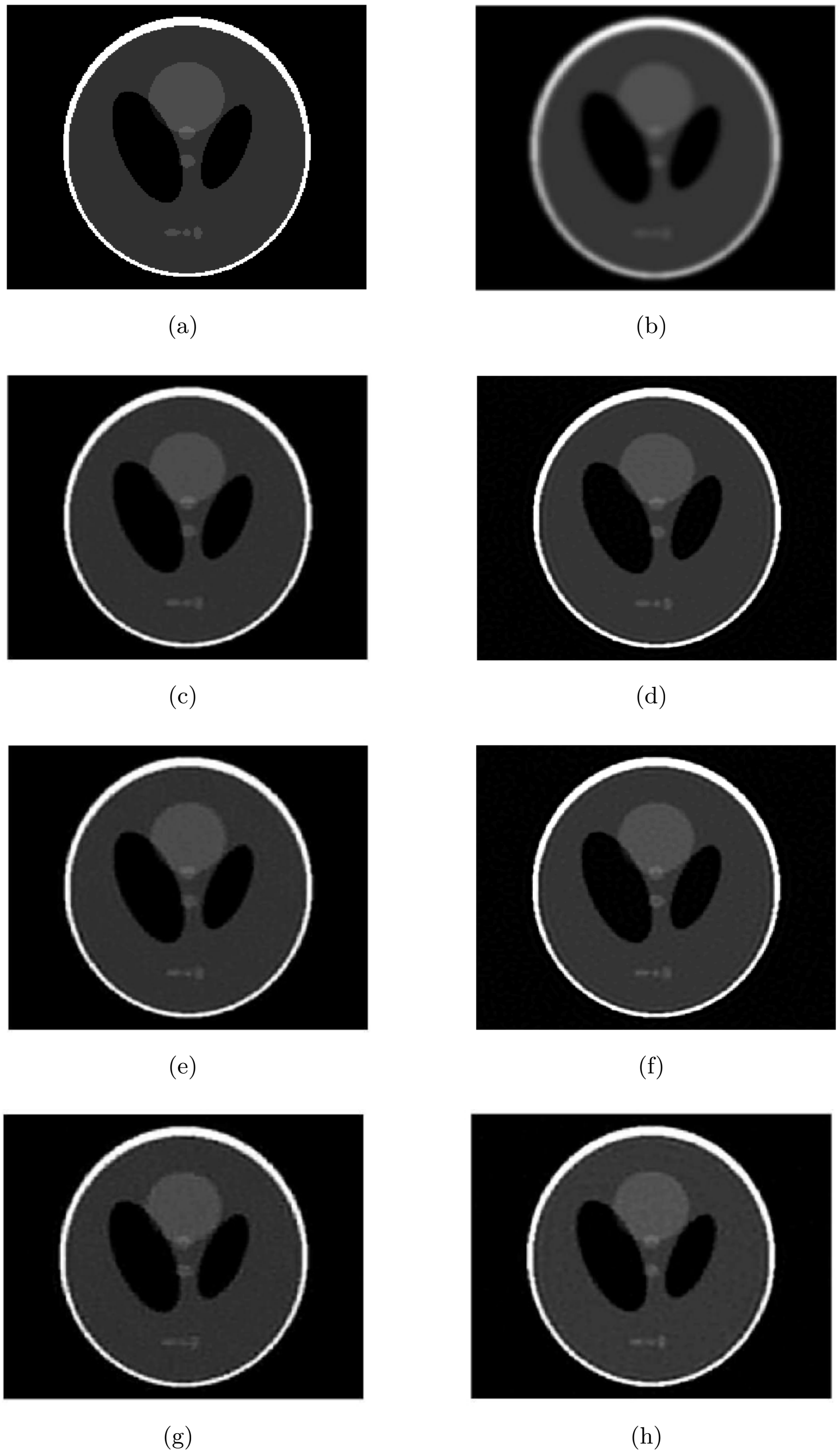

(a) (b) (c) (d) (e) (f) (g) (h)

Figure 3.2: Shepp-logan image and its compressive deconvolution results for a SNR of 40dB. (a) Original image, (b) Blurred image, (c,e,g) Compressive deconvolution results with CD_Amizic for CS ratios of 0.8, 0.6 and 0.4, (d,f,h) Compressive deconvolution results with the proposed method for CS ratios of 0.8, 0.6 and 0.4.

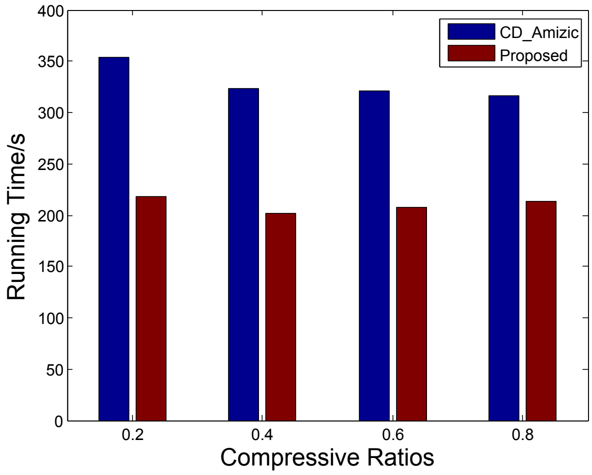

Figure 3.3: Mean reconstruction running time for 10 experiments conducted for each CS ratio for a SNR of 40 dB.

3.6.3 Results on modified Shepp-Logan phantom

We modified the Shepp-Logan phantom in order to simulate the speckle noise that degrades in practice the US images. For this, we followed the procedure classically used in US imaging [Ng 2007a]. First, scatterers at uniformly random locations have been generated, with amplitudes distributed according to a zero-mean generalized Gaussian distribution (GGD) with the shape parameter set to 1.3 and the scale parameter equal to 1. The scatterer amplitudes were further multiplied by the values of the original Shepp-Logan phantom pixels located at the closest positions to the scatterers. The resulting image, mimicking the tissue reflectivity function (TRF) in US imaging, is shown in Fig.3.4(a). The blurred image in Fig.3.4(b) was obtained by 2D convolution between the TRF and a spatially invariant PSF generated with Field II [Jensen 1991], a state-of-the-art simulator in US imaging. It corresponds to a 3.5 MHz linear probe, sampled in the axial direction at 20 MHz. The compressive measurements were obtained by projecting the blurred image onto SRM and by adding a Gaussian noise corresponding to a SNR of 40 dB.

3.6.3.1 Comparison between different prior terms

Reconstruction results for a CS ratio of 0.6 are shown in Fig.3.4. They were obtained with: the recent compressive deconvolution technique reported in [Amizic 2013] (referred as CD_Amizic), the proposed method using the generalized TV prior (denoted by ADMM_GTV) and the proposed method using the l_p-norm for p equal to 1.5, 1.3 and 1 (denoted respectively by ADMM_L1.5, ADMM_L1.3 and ADMM_L1). All the hyperparameters were set to their best possible values by cross-validation. For CD_Amizic, $\{\beta, \alpha, \eta, \tau\} = \{10^7, 1, 10^4, 10^2\}$. For ADMM_GTV $\{\mu, \alpha, \beta\} = \{10^{-5}, 2 \times 10^{-1}, 10^2\}$ and for the proposed method with l_p-norms, $\{\mu, \alpha, \beta, \gamma\} = \{10^{-5}, 2 \times 10^{-1}, 10^1, 3 \times 10^{-2}\}$.

The quantitative results for different CS ratios are regrouped in Table.3.2. They confirm that the l_p-norm is better adapted to recover the TRF in US imaging than the generalized TV. The difference between the two priors is further accentuated when the CS ratio decreases.

Keeping in mind that the generalized TV prior is not well suited to model the TRF in US imaging, we did not use CD_Amizic in the following sections dealing with simulated and experimental US images. Moreover, the proposed method was only evaluated in its l_p-norm minimization form.

3.6.3.2 Comparison with a typical CS reconstruction

In Fig.3.4 and Table.3.2, we have also shown the results of a typical CS reconstruction algorithm, YALL1 [Yang 2011]. Both the visual and quantitative results confirm that the proposed optimization scheme can outperform the typical CS reconstruction algorithms.

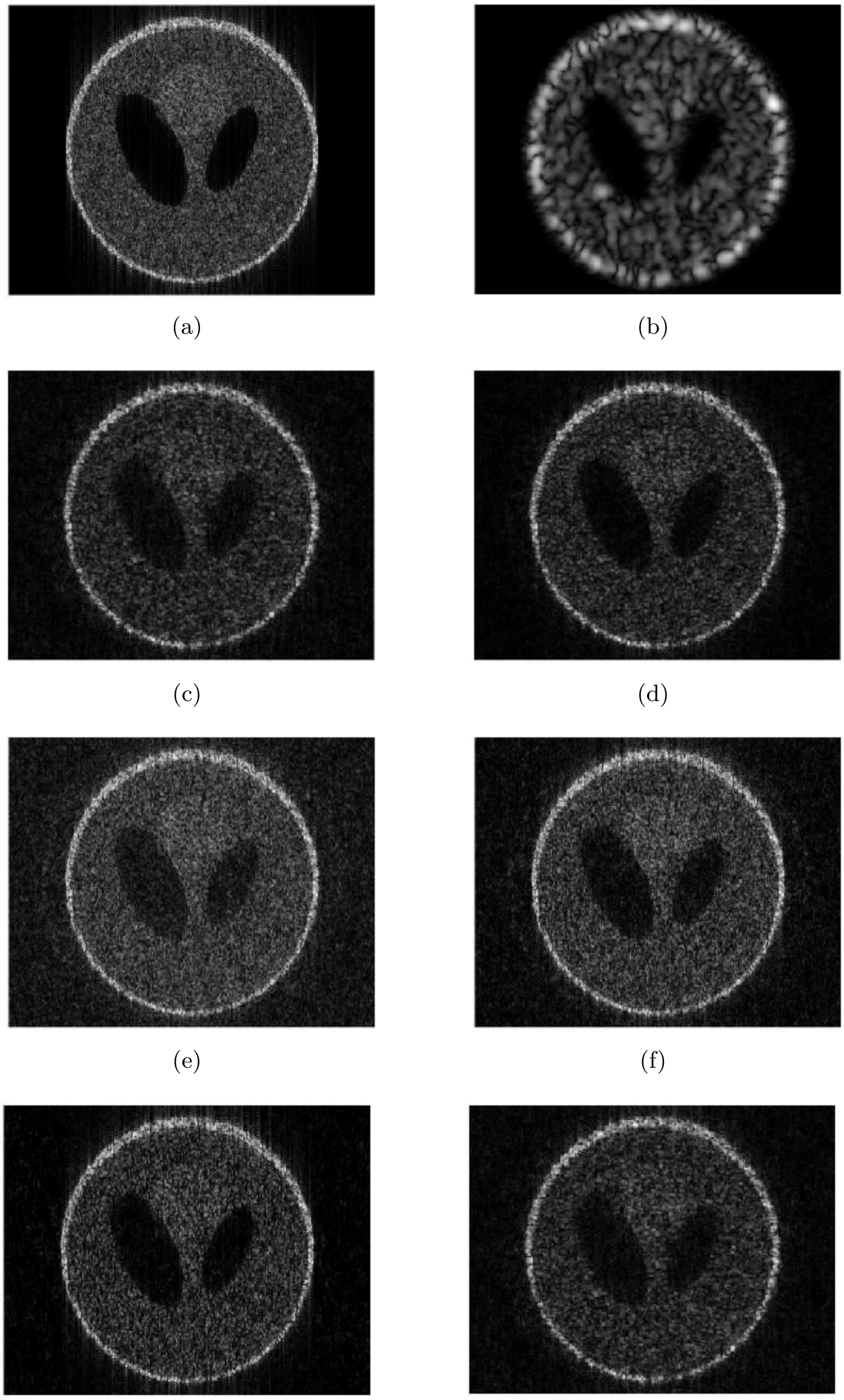

(a) (b)

(c) (d)

(e) (f)

(g) (h)

Figure 3.4: Reconstruction results for SNR = 40dB and a CS ratio of 0.6. (a) Modified Shepp-Logan phantom containing random scatterers (TRF), (b) Degraded image by convolution with a simulated US PSF, (c) Reconstruction result with CD_Amizic, (d) Reconstruction result with the proposed method using a generalized TV prior (ADMM_GTV), (e, f, g) Reconstruction results with the proposed method using an l_p-norm prior, for p equal to 1.5, 1.3 and 1 (ADMM_L1.5, ADMM_L1.3 and ADMM_L1), (h) Reconstruction results with the Yall1.

Table 3.2: Quatitative results for the modified Shepp-Logan phantom with US speckle (SNR = 40dB)

CS ratios		CD _Amizic	ADMM _GTV	ADMM _L1.5	ADMM _L1.3	ADMM _L1	YALL1
80%	PSNR	30.82	31.11	32.23	**32.32**	32.05	27.12
	SSIM	83.24	85.03	86.44	**88.77**	87.70	77.43
60%	PSNR	29.68	29.83	31.27	**31.50**	31.32	26.91
	SSIM	74.58	77.83	82.26	**86.03**	85.64	75.78
40%	PSNR	26.76	28.11	29.58	30.04	**30.12**	26.73
	SSIM	43.43	61.46	73.88	79.95	**81.75**	73.33
20%	PSNR	20.22	21.53	26.81	27.29	**28.20**	25.78
	SSIM	8.35	12.77	51.70	62.93	**72.34**	64.82

3.6.4 Results on simulated data

In this section, we compared the compressive deconvolution results with our method to those obtained with a sequential approach. The latter recovers in a first step the blurred US image from the CS measurements and reconstructs in a second step the TRF by deconvolution.

Two ultrasound data sets were generated, as shown in Figures 3.5 and 3.6. They were obtained by 2D convolution between spatially invariant PSFs and the TRFs. For the first simulated image, the same PSF as in the previous section was simulated and the TRF corresponds to a simple medium representing a round hypoechoic inclusion into a homogeneous medium. The scatterer amplitudes were random variables distributed according to a GGD with the shape parameter set to 1. The second data set is one of the examples proposed by the Field II simulator [Jensen 1991], mimicking a kidney tissue. The PSF was also generated with Field II corresponding to a 4 MHz central frequency and an axial sampling frequency of 40 MHz. It corresponds to a focalized emission (the PSF was measured at the focal point) with a simulated linear probe containing 128 elements. The shape parameter of the GGD used to generate the scatterer amplitudes was set to 1.5 and the number of scatterers was considered sufficiently large (10^6) to ensure fully developped speckle. In both experiments, the compressed measurements were obtained by projecting the RF images on SRM, aiming at reducing the amount of data available.

With the sequential approach, YALL1 was used to process the CS reconstruction following the minimization in (2.16). The deconvolution step was processed using the PFB as described in section.2.2.2.3. Both the CS reconstruction and the deconvolution procedures were performed with the same priors as the proposed compressive deconvolution approach.

The algorithm stops when the convergence criterion $\| \boldsymbol{x}^k - \boldsymbol{x}^{k-1} \| / \| \boldsymbol{x}^{k-1} \| < 1e^{-3}$ is satisfied. In order to highlight the influence of these hyperparameters on the reconstruction results, we consider the simulated US image in Fig. 3.5. The PSNR values obtained while varying the values of these hyperparameters are shown in Fig. 3.7. From Fig. 3.7, one can observe that the best results are obtained for small values of μ, corresponding to an important weight given to the data attachment term. The best value of α is the one providing the best compromise between the two prior terms considered in (3.5), promoting minimal ℓ_1-norm of $\boldsymbol{Hx}$ in the wavelet domain and GGD statistics for $\boldsymbol{x}$. The choice of β and γ parameters, used in the augmented Lagrangian function and in the approximation of the ℓ_p-norm proximal operator, have an important impact on the algorithm convergence. Moreover, one may observe that for a given range of values, the choice of γ has less impact on the quality of the results than the other three hyperparameters. Despite different optimal values for each CS ratio, in the results presented through the paper, we considered their values fixed for all the CS ratios. The hyperparameters with our approach were set to $\{\mu, \alpha, \beta, \gamma\} = \{10^{-5}, 2\times 10^{-1}, 1, 10^{-2}\}$ for the round cyst image and $\{\mu, \alpha, \beta, \gamma\} = \{10^{-5}, 2 \times 10^{-1}, 1 \times 10^3, 10^{-4}\}$ for the simulated kidney image.

The quantitative results in Table 4.1 show that the proposed method outperforms the sequential approach, for all the CS ratios and values of p considered. They confirm the visual impression given by Figures 3.5 and 3.6. We should remark that for the first simulated data set, the l_1-norm gives the best result. This may be explained by the simple geometry of the simulated TRF, namely its sparse appearance. The second data set, more realistic and more representative of experimental situations, shows the interest of using different values of p. It confirms the generality interest of the proposed method, namely its flexibility in the choice of TRF priors.

Table 3.3: Quantitative results for simulated US images (SNR = 40dB)

CS Ratios		Sequential	Proposed ($l_{1.5}$)	Proposed ($l_{1.3}$)	Proposed (l_1)
			Figure 3.5		
80%	PSNR	26.50	24.74	25.29	**26.82**
	SSIM	75.01	73.91	77.66	**79.45**
60%	PSNR	25.96	24.44	24.74	**26.03**
	SSIM	68.59	69.37	74.72	**76.26**
40%	PSNR	23.38	24.21	24.57	**25.28**
	SSIM	47.60	62.58	71.86	**72.78**
20%	PSNR	21.10	23.72	24.42	**24.77**
	SSIM	36.07	50.34	66.48	**70.44**
			Figure 3.6		
80%	PSNR	26.06	26.71	**26.72**	26.69
	SSIM	45.99	56.81	**56.84**	56.71
60%	PSNR	25.44	**26.38**	26.31	26.29
	SSIM	38.86	**54.14**	53.90	53.80
40%	PSNR	25.37	25.89	25.95	**25,97**
	SSIM	34.61	50.22	50.51	**50.61**
20%	PSNR	24.96	**25.22**	25.20	25.12
	SSIM	30.89	**41.41**	41.32	40.97

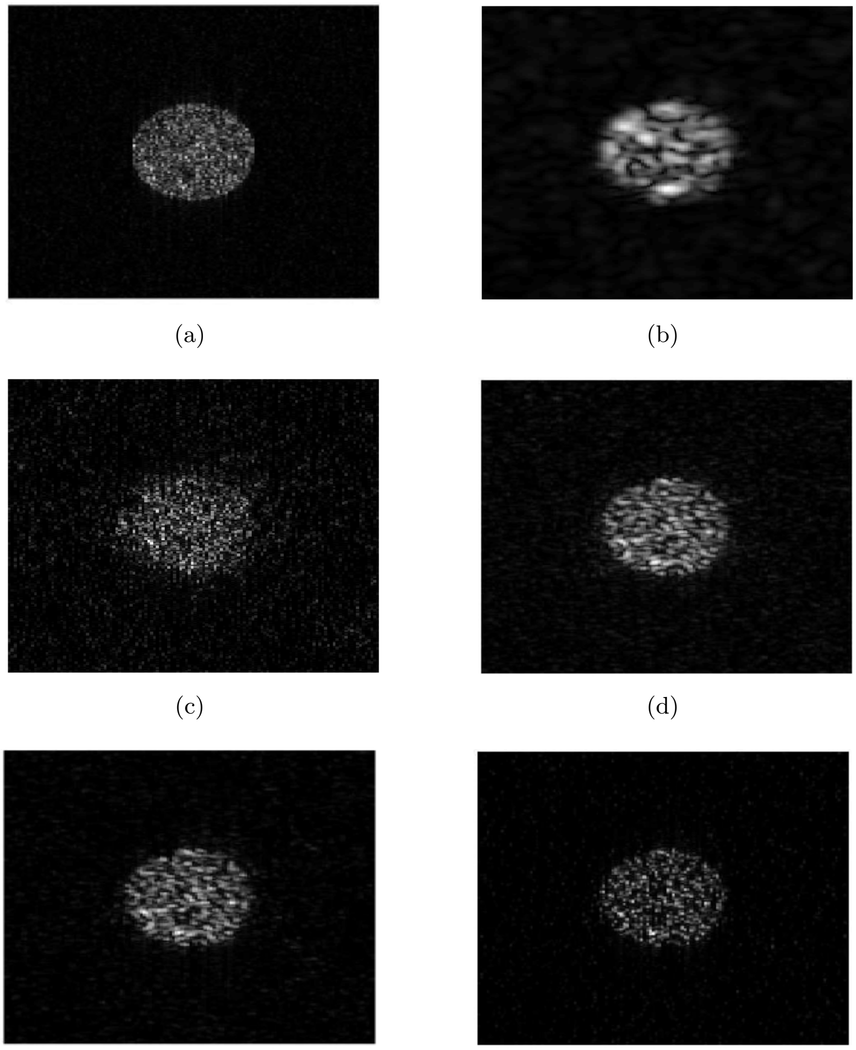

(a) (b)

(c) (d)

(e) (f)

Figure 3.5: Simulated US image and its compressive deconvolution results for a CS ratio of 0.4 and a SNR of 40 dB. (a) Original tissue reflectivity function, (b) Simulated US image, (c) Results using the sequential method, (d, e, f) Results with the proposed method for p equal to 1.5, 1.3 and 1 respectively.

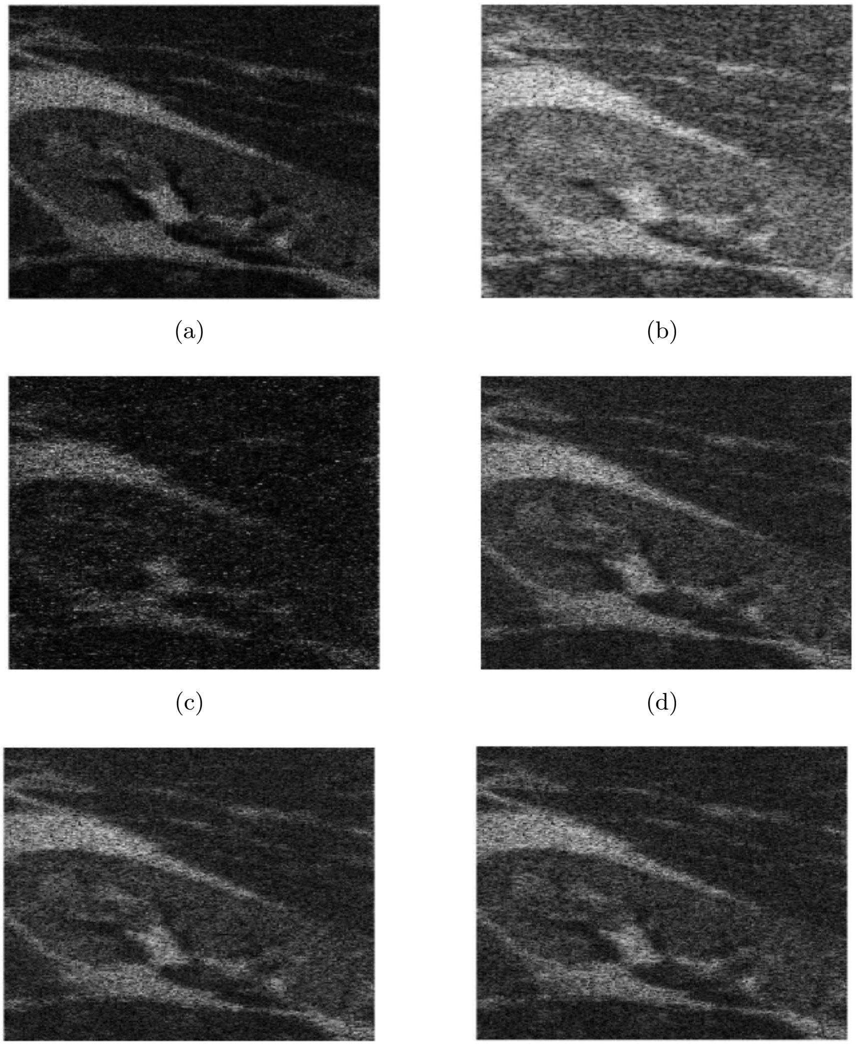
(a) (b) (c) (d) (e) (f)

Figure 3.6: Simulated kidney image and its compressive deconvolution results for a CS ratio of 0.2 and a SNR of 40dB. (a) Original tissue reflectivity function, (b) Simulated US image, (c) Results using the sequential method, (d, e, f) Results with the proposed method for p equal to 1.5, 1.3 and 1 respectively.

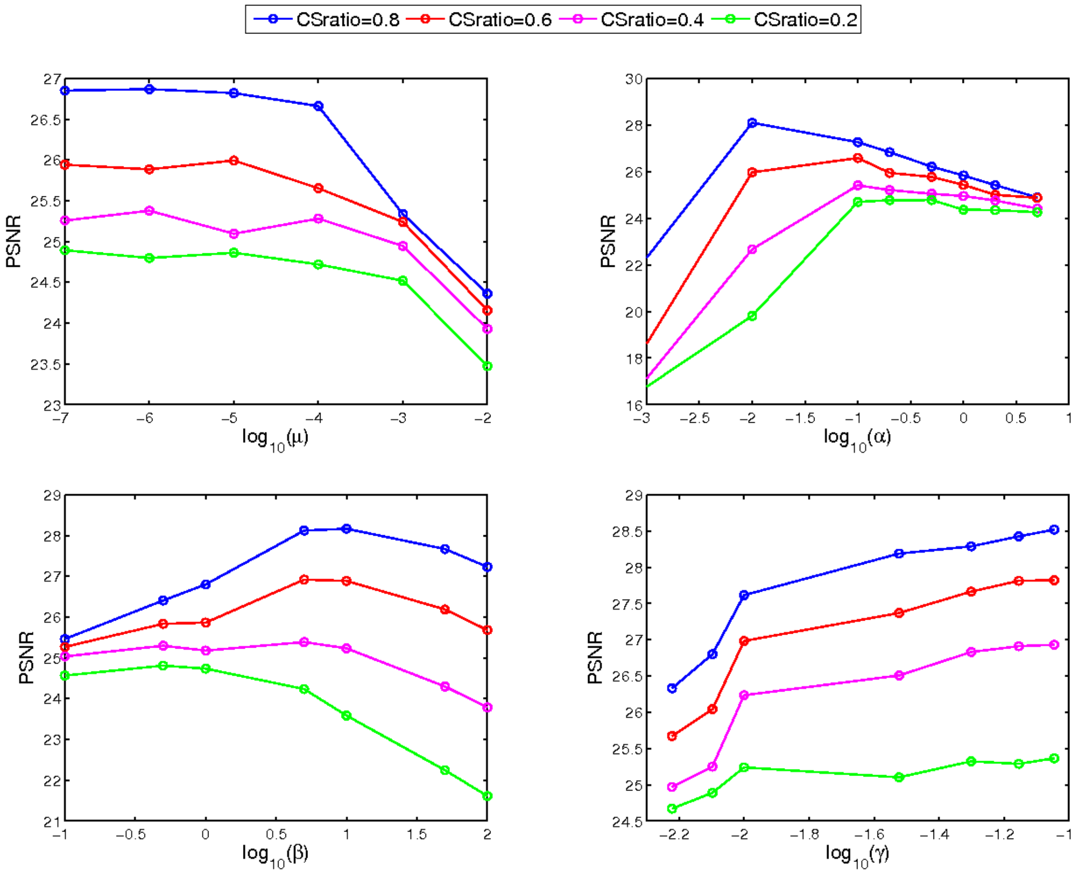

Figure 3.7: The impact of hyperparameters on the performance of proposed algorithm on Figure. 3.5.

3.6.5 Results on *in vivo* data

In this section, we tested our method with two *in vivo* data sets. The experimental data were acquired with a 20 MHz single-element US probe on a mouse bladder (first example) and kidney (second example). Unlike the simulated cases studied previously, the PSF is not known in these experiments and has to be estimated from the data. In our work, the PSF estimation method presented in [Michailovich 2005] has been adopted. The PSF estimation adopted is not iterative and the computational time for this pre-processing step is negligible compared to the reconstruction process. The compressive deconvolution results are shown in Figures 3.8 and 3.9 for different CS ratios.

The two regions selected for the computation of the CNR are highlighted by the two red rectangles in Figures 3.8(a) and 3.9(a). Table. 3.4 gives the CNR assessment for these two *in vivo* data sets with different CS ratios and p values. Given the sparse appearance of the bladder image in Fig. 3.8(a), the best result was obtained for p equal to 1. However, the complexity of the tissue structures in the kidney image in Fig. 3.9 results into better results for p larger than 1. Nevertheless, both the visual impression and the CNR results show the ability of our method to both recover the image from compressive measurements and to improve its contrast compared to the standard US image. In particular, we may remark the improved contrast of the structures inside the kidney on our reconstructed images compared to the original one.

Table 3.4: CNR assessment for *in vivo* data

Figure	Original CNR	p values	CS ratios			
			100%	80%	60%	40%
Fig.6	1.106	p = 1	**1.748**	**1.546**	**1.367**	**1.333**
		p = 1.5	1.690	1.424	1.304	1.287
Fig.7	1.316	p = 1	**2.373**	**2.162**	1.895	1.434
		p = 1.5	2.317	2.082	**1.905**	**1.451**

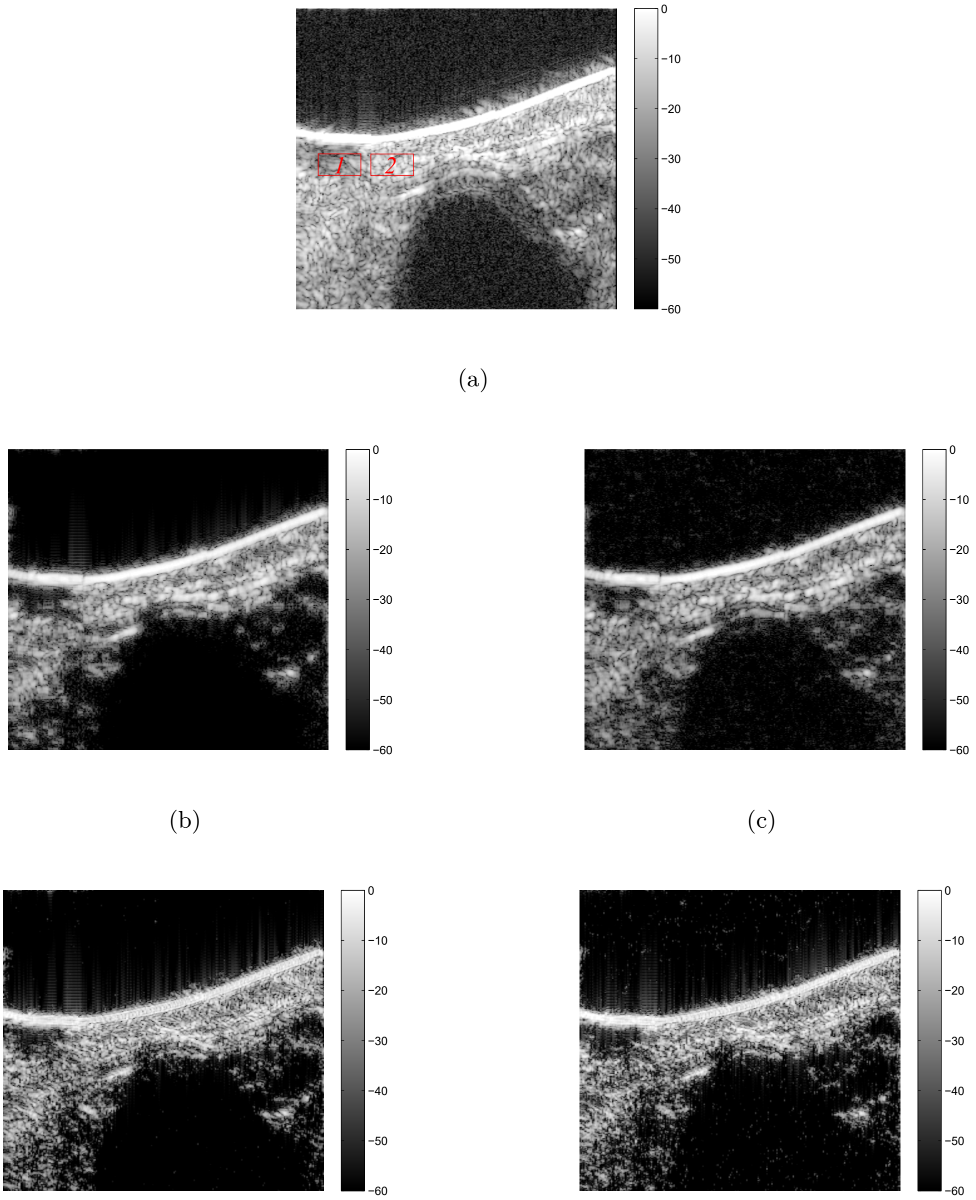

(a)

(b)

(c)

(d)

(e)

Figure 3.8: (a)Original *in vivo* image and (b-e) its compressive deconvolution results for CS ratios of 1, 0.8, 0.6 and 0.4 respectively with $p = 1$.

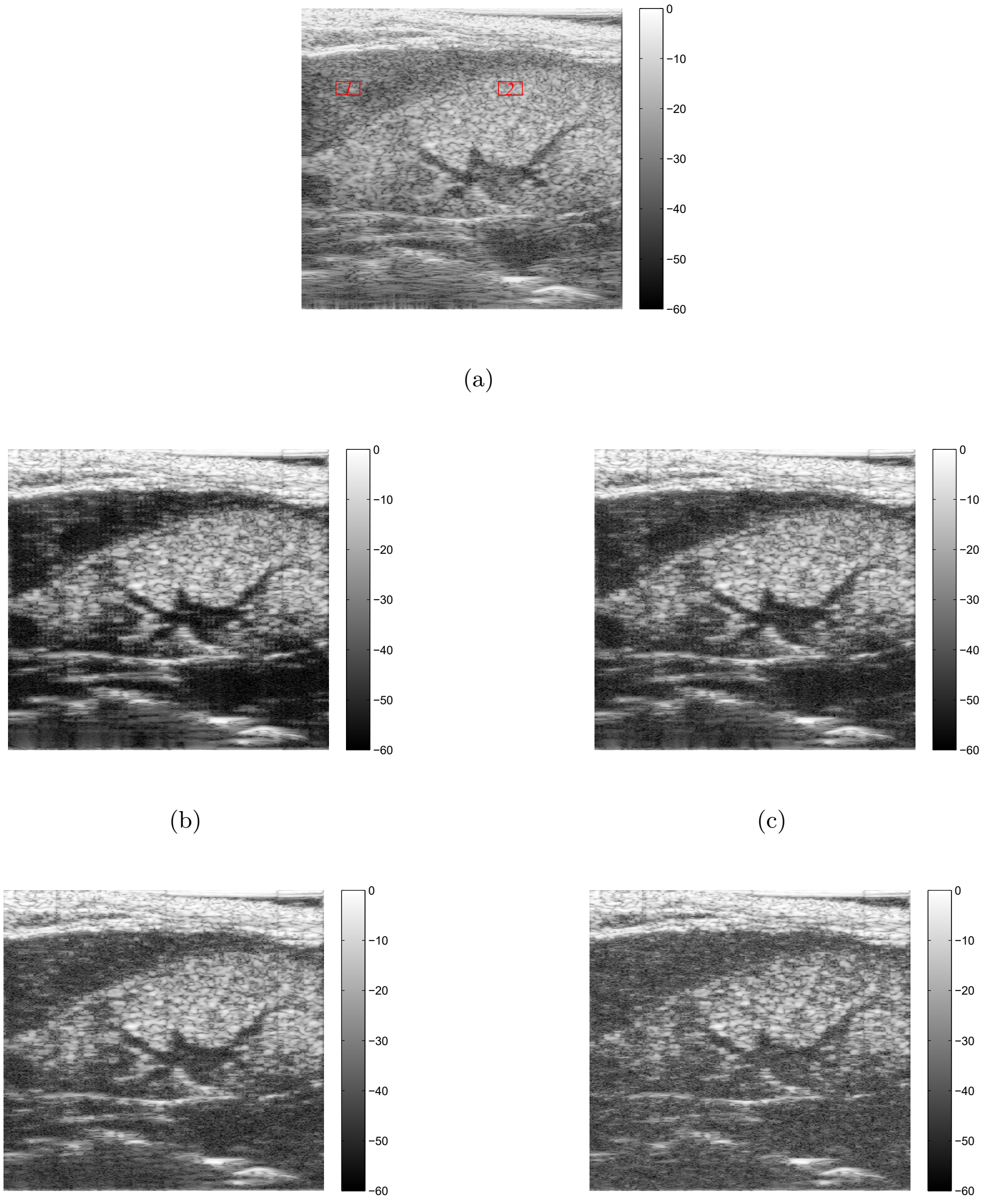

(a)

(b)

(c)

(d)

(e)

Figure 3.9: (a)Original *in vivo* image and (b-e) and its compressive deconvolution results for CS ratios of 1, 0.8, 0.6 and 0.4 respectively with $p = 1.5$.

3.7 Conclusion

This chapter introduced an ADMM-based compressive deconvolution framework for ultrasound imaging systems. The main benefit of our approach is its ability to reconstruct enhanced ultrasound RF images from compressed measurements, by inverting a linear model combining random projections and 2D convolution. Simulation results on the standard Shepp-Logan phantom show the superiority of our method, both in accuracy and in computational time, over a recently published compressive deconvolution approach. Moreover, we show that the proposed joint CS and deconvolution approach is more robust than an intuitive technique consisting of first reconstructing the RF data and second deconvolving it. Finally, promising results on *in vivo* data demonstrate the effectiveness of our approach in practical situations. We emphasize that the 2D convolution model may not be valid over the entire image because of the spatially variant PSF. While in our work we focused on compressive image deconvolution based on spatially invariant PSF, a more complicated global model combining several local shift invariant PSFs represents an interesting perspective of our approach.

Chapter 4

Compressive Deconvolution using SDMM

Part of the work in this chapter has been published in [Chen 2016b].

Contents

4.1 Introduction

The direct model of Compressive Deconvolution we have introduced is

$$\boldsymbol{y} = \Phi H \boldsymbol{x} + \boldsymbol{n} \tag{4.1}$$

where the variables $\boldsymbol{y} \in \mathbb{R}^M$ corresponds to the M compressed measurements, $\Phi \in \mathbb{R}^{M \times N}$ represents the sampling matrix, $H \in \mathbb{R}^{N \times N}$ is a BCCB matrix related to the 2D PSF of the system, $\boldsymbol{x} \in \mathbb{R}^N$ represents the TRF and $\boldsymbol{n}$ is a zero-mean additive white Gaussian noise.

In this Chapter, we further improve the US Compressive Deconvolution scheme described in the previous chapter by proposing a new reconstruction algorithm based on the Simultaneous Direction Method of Multipliers (SDMM) [Setzer 2010]. We hereby focus on the US imaging adjusted objective function as

$$\underset{\boldsymbol{x} \in \mathbb{R}^N}{min} \quad \| \Psi^{-1} H \boldsymbol{x} \|_1 + \alpha \| \boldsymbol{x} \|_p^p + \frac{1}{2\mu} \| \boldsymbol{y} - \Phi H \boldsymbol{x} \|_2^2 \tag{4.2}$$

4.2 Basics of Simultaneous Direction Method of Multipliers

The algorithm of Simultaneous Direction Method of Multipliers (SDMM) e.g, [Setzer 2010], generalizes the alternating split Bregman method (ASB) [Goldstein 2009] to a sum of more than two functions. The ASB was initially proposed to solve optimization problems that can be expressed in the following form:

$$\underset{u \in \mathbb{R}^s, v \in \mathbb{R}^t}{argmin} \quad f(u) + g(v) \quad s.t. \quad v = Cu \tag{4.3}$$

where $C \in \mathbb{R}^{t \times s}$ is a given matrix, $f : \mathbb{R}^s \to \bar{\mathbb{R}}$ and $g : \mathbb{R}^t \to \bar{\mathbb{R}}$ are convex functions. $\bar{\mathbb{R}}$ is designated for extended real numbers, *i.e.*, $\mathbb{R} \bigcup \{+\infty\}$.

The iterative ASB method declines as follows:

$$u^{k+1} = \underset{u \in \mathbb{R}^s}{argmin} \quad f(u) + \frac{1}{2\beta} \| b^k + Cu - v^k \|_2^2 \tag{4.4}$$

$$v^{k+1} = \underset{v \in \mathbb{R}^t}{argmin} \quad g(v) + \frac{1}{2\beta} \| b^k + Cu^{k+1} - v \|_2^2 \tag{4.5}$$

$$b^{k+1} = b^k + Cu^{k+1} - v^{k+1} \tag{4.6}$$

where $b \in \mathbb{R}^t$ is the Lagrangian parameter. It has been proven that the alternating split Bregman method is equivalent to Alternating Direction Method of Multipliers (ADMM) when the constraints are linear [Esser 2009].

Inspired from ASB, the general optimization problem considered in the framework of SDMM is:

$$\underset{u\in\mathbb{R}^s}{argmin}\sum_{i=1}^{m} f_i(C_i u) \tag{4.7}$$

where $C_i \in \mathbb{R}^{t_i,s}$ and $f_i : \mathbb{R}^{t_i} \to \bar{\mathbb{R}}$ are convex functions. Considering $v_i \in \mathbb{R}^{t_i}$, $v_i = C_i u$, $f(u) = \langle 0, u\rangle$ and $g(v) = \sum_{i=1}^{m} f_i(v_i)$, (4.7) can be reformulated as

$$\underset{u\in\mathbb{R}^s, v_i\in\mathbb{R}^t_i}{argmin} \quad f(u) + \sum_{i=1}^{m} f_i(v_i) \tag{4.8}$$

Similarly to ASB method, SDMM iteratively solves the optimization problem above as follows:

$$u^{k+1} = \underset{u\in\mathbb{R}^s}{argmin}\frac{1}{2\beta} \parallel \begin{pmatrix} b_1^k \\ \vdots \\ b_m^k \end{pmatrix} + \begin{pmatrix} C_1 \\ \vdots \\ C_m \end{pmatrix} u - \begin{pmatrix} v_1^k \\ \vdots \\ v_m^k \end{pmatrix} \parallel^2 \tag{4.9}$$

$$\begin{pmatrix} v_1^{k+1} \\ \vdots \\ v_m^{k+1} \end{pmatrix} = \underset{v_i\in\mathbb{R}^t_i}{argmin}\{\frac{1}{2\beta} \parallel \begin{pmatrix} b_1^k \\ \vdots \\ b_m^k \end{pmatrix} + \begin{pmatrix} C_1 \\ \vdots \\ C_m \end{pmatrix} u^{k+1} - \begin{pmatrix} v_1 \\ \vdots \\ v_m \end{pmatrix} \parallel^2 + \sum_{i=1}^{m} f_i(v_i)\} \tag{4.10}$$

$$\begin{pmatrix} b_1^{k+1} \\ \vdots \\ b_m^{k+1} \end{pmatrix} = \begin{pmatrix} b_1^k \\ \vdots \\ b_m^k \end{pmatrix} + \begin{pmatrix} C_1 \\ \vdots \\ C_m \end{pmatrix} u^{k+1} - \begin{pmatrix} v_1^{k+1} \\ \vdots \\ v_m^{k+1} \end{pmatrix} \tag{4.11}$$

4.3 Proposed SDMM parameterization

In this chapter we propose an SDMM-based optimization scheme adapted to solve the problem in (4.2). First, we remark that (4.2) can be reformulated as

$$\underset{\boldsymbol{x}}{argmin} \quad f_1(\boldsymbol{v}_1) + f_2(\boldsymbol{v}_2) + f_3(\boldsymbol{v}_3) \tag{4.12}$$

with

$$\begin{cases} f_1(\boldsymbol{v}_1) = \alpha \parallel \boldsymbol{v}_1 \parallel_p^p \\ f_2(\boldsymbol{v}_2) = \parallel \boldsymbol{v}_2 \parallel_1 \\ f_3(\boldsymbol{v}_3) = \frac{1}{2\mu} \parallel \boldsymbol{y} - \Phi\boldsymbol{v}_3 \parallel_2^2 \\ \boldsymbol{v}_1 = C_1\boldsymbol{x}, \boldsymbol{v}_2 = C_2\boldsymbol{x}, \boldsymbol{v}_3 = C_3\boldsymbol{x} \\ C_1 = I_N, C_2 = \Psi^{-1}H, C_3 = H \end{cases}$$

Using the parametrization above, the SDMM steps given in (4.9)-(4.11) write for our compressive deconvolution problem as follows:

$$\boldsymbol{x}^{k+1} = \underset{\boldsymbol{x}\in\mathbb{R}^N}{argmin} \quad \frac{1}{2\beta} \parallel \begin{pmatrix} \boldsymbol{b}_1^k \\ \boldsymbol{b}_2^k \\ \boldsymbol{b}_3^k \end{pmatrix} + \begin{pmatrix} I_N \\ \Psi^{-1}H \\ H \end{pmatrix} \boldsymbol{x} - \begin{pmatrix} \boldsymbol{v}_1^k \\ \boldsymbol{v}_2^k \\ \boldsymbol{v}_3^k \end{pmatrix} \parallel^2 \tag{4.13}$$

$$\begin{pmatrix} \boldsymbol{v}_1^{k+1} \\ \boldsymbol{v}_2^{k+1} \\ \boldsymbol{v}_3^{k+1} \end{pmatrix} = \underset{\boldsymbol{v}_1,\boldsymbol{v}_2,\boldsymbol{v}_3}{argmin}\{\frac{1}{2\beta} \parallel \begin{pmatrix} \boldsymbol{b}_1^k \\ \boldsymbol{b}_2^k \\ \boldsymbol{b}_3^k \end{pmatrix} + \begin{pmatrix} I_N \\ \Psi^{-1}H \\ H \end{pmatrix} \boldsymbol{x}^{k+1} - \begin{pmatrix} \boldsymbol{v}_1 \\ \boldsymbol{v}_2 \\ \boldsymbol{v}_3 \end{pmatrix} \parallel^2 + \sum_{i=1}^{3} f_i(\boldsymbol{v}_i)\} \tag{4.14}$$

$$\begin{pmatrix} \boldsymbol{b}_1^{k+1} \\ \boldsymbol{b}_2^{k+1} \\ \boldsymbol{b}_3^{k+1} \end{pmatrix} = \begin{pmatrix} \boldsymbol{b}_1^k \\ \boldsymbol{b}_2^k \\ \boldsymbol{b}_3^k \end{pmatrix} + \begin{pmatrix} I_N \\ \Psi^{-1}H \\ H \end{pmatrix} \boldsymbol{x}^{k+1} - \begin{pmatrix} \boldsymbol{v}_1^{k+1} \\ \boldsymbol{v}_2^{k+1} \\ \boldsymbol{v}_3^{k+1} \end{pmatrix} \tag{4.15}$$

In the following, we give the details of solving each of the steps above. Firstly, we remark that (4.13) is a classical l_2-norm minimization problem that can be efficiently solved in the Fourier domain [Ng 2010].

(4.14) consists in solving three subproblems, corresponding to the update of $\boldsymbol{v}_1$, $\boldsymbol{v}_2$ and respectively $\boldsymbol{v}_3$. The $\boldsymbol{v}_1$-subproblem can be solved as follows:

$$\begin{aligned} \boldsymbol{v}_1^{k+1} =& \underset{\boldsymbol{v}_1}{argmin} \quad \alpha \parallel \boldsymbol{v}_1 \parallel_p^p + \frac{1}{2\beta} \parallel \boldsymbol{b}_1^k + \boldsymbol{x}^{k+1} - \boldsymbol{v}_1 \parallel_2^2 \\ =& prox_{\alpha\beta\parallel\cdot\parallel_p^p}(\boldsymbol{b}_1^k + \boldsymbol{x}^{k+1}) \end{aligned} \tag{4.16}$$

where *prox* represents the proximal operator and the proximal operator of $\parallel \boldsymbol{x} \parallel_p^p$ has been given explicitly previously in section.2.2.2.3.

The $\boldsymbol{v}_2$-subproblem can also be solved using the proximal operator associated to the ℓ_1-norm that corresponds to the soft thresholding operator [Ng 2010] (see section.2.2.2.3):

$$\begin{aligned} \boldsymbol{v}_2^{k+1} =& \underset{\boldsymbol{v}_2}{argmin} \quad \parallel \boldsymbol{v}_2 \parallel_1 + \frac{1}{2\beta} \parallel \boldsymbol{b}_2^k + \Psi^{-1}H\boldsymbol{x}^{k+1} - \boldsymbol{v}_2 \parallel_2^2 \\ =& prox_{\beta\parallel\cdot\parallel_1}(\boldsymbol{b}_2^k + \Psi^{-1}H\boldsymbol{x}^{k+1}) \end{aligned} \tag{4.17}$$

Finally, the $\boldsymbol{v}_3$-subproblem can be solved as follows:

$$\begin{aligned} \boldsymbol{v}_3^{k+1} &= \underset{\boldsymbol{v}_3}{argmin} \frac{1}{2\mu} \parallel y - \Phi\boldsymbol{v}_3 \parallel_2^2 + \frac{1}{2\beta} \parallel \boldsymbol{b}_3^k + H\boldsymbol{x}^{k+1} - \boldsymbol{v}_3 \parallel_2^2 \\ &\Leftrightarrow [\beta\Phi^t\Phi + \mu]\boldsymbol{v}_3^{k+1} = \beta\Phi^t\boldsymbol{y} + \mu\boldsymbol{b}_3^k + \mu H\boldsymbol{x}^{k+1} \end{aligned} \tag{4.18}$$

For orthogonal sampling matrices Φ, the Sherman-Morrison-Woodbury inversion matrix lemma [Deng 2013] allows us to efficiently find the solution of the $\boldsymbol{v}_3$-subproblem above. However, when the sampling matrix Φ is non-orthogonal, the solution of $\boldsymbol{v}_3$-subproblem in (4.18) cannot be computed in practical situations because of the high-dimensional matrices. To overcome this issue and make our compressive deconvolution method more general and therefore relevant to various compressive acquisition schemes in US imaging, we propose to use Newton's method to approximate its solution.

Let us denote

$$h(\boldsymbol{v}_3) = [\beta\Phi^t\Phi + \mu]\boldsymbol{v}_3 - \beta\Phi^t\boldsymbol{y} + \mu\boldsymbol{b}_3^k + \mu H\boldsymbol{x}^{k+1} \tag{4.19}$$

At each iteration, we approximate $\boldsymbol{v}_3^{k+1}$ by

$$\boldsymbol{v}_3^{k+1} = \boldsymbol{v}_3^k - stp * h(\boldsymbol{v}_3^k) \tag{4.20}$$

where stp is defined as

$$stp = \frac{h(\boldsymbol{v}_3^k)^t h(\boldsymbol{v}_3^k)}{\beta[\Phi h(\boldsymbol{v}_3^k)]^t[\Phi h(\boldsymbol{v}_3^k)] + \mu h(\boldsymbol{v}_3^k)^t h(\boldsymbol{v}_3^k)} \tag{4.21}$$

To conclude, Algorithm. 3 summarizes the SDMM-based numerical scheme proposed for solving (4.2).

Algorithm 3 Compressive deconvolution SDMM-based algorithm.

```
Require: $\alpha$, $\mu$, $\beta$, $\boldsymbol{v}_i^0$, $\boldsymbol{b}_i^0$, $i = 1, 2, 3$
while not converged do
    $\boldsymbol{x}^{k+1} \leftarrow \boldsymbol{v}_i^k, \boldsymbol{b}_i^k$            ▷ update $\boldsymbol{x}^{k+1}$ using (4.13)
    $\boldsymbol{v}_1^{k+1} \leftarrow \boldsymbol{b}_1^k, \boldsymbol{x}^{k+1}$         ▷ update $\boldsymbol{v}_1^{k+1}$ using (4.16)
    $\boldsymbol{v}_2^{k+1} \leftarrow \boldsymbol{b}_2^k, \boldsymbol{x}^{k+1}$         ▷ update $\boldsymbol{v}_2^{k+1}$ using (4.17)
    $\boldsymbol{v}_3^{k+1} \leftarrow \boldsymbol{b}_3^k, \boldsymbol{x}^{k+1}$         ▷ update $\boldsymbol{v}_3^{k+1}$ using (4.18)
    if $\Phi$ is orthogonal then
        Solve (4.18) by Sherman-Morrison-Woodbury inversion matrix lemma
    else
        Solve (4.18) by using (4.20)
    end if
    $\boldsymbol{b}_i^{k+1} \leftarrow \boldsymbol{v}_i^{k+1}, \boldsymbol{x}^{k+1}$       ▷ update $\boldsymbol{b}_i^{k+1}$ using (4.15)
end while
Ensure: $\boldsymbol{x}$
```

We emphasize that compared to the ADMM-based scheme that we have discussed in the previous chapter, the method resumed in Algorithm. 3 requires one less hyperparameter. Moreover, with the proposed optimization scheme all the subproblems are solved exactly, while in the ADMM-based method we have only obtained an approximation for the $\boldsymbol{v}_1$-subproblem in (4.16). This improvement allows the SDMM-based iterative scheme to converge faster than the ADMM-based algorithm described in Chapter 3.

Since this $\boldsymbol{v}_1$-subproblem is critical for the deconvolution process, one may also expect more accurate compressive deconvolution results with SDMM than with ADMM.

4.4 Results

In this section, we provide numerical experiments to evaluate the effectiveness of the proposed compressive deconvolution optimization framework, denoted by SDMM hereafter. Since we have shown in Chapter 3 the superiority of the ADMM-based method (denoted by ADMM in this section) compared to other compressive deconvolution methods, the technique in Chapter. 3 is used herein for comparison purpose.

4.4.1 Results on simulated data

Two groups of simulation experiments (named Group 1 and 2) have been conducted to evaluate the performance of the proposed scheme. The RF images have been generated following the procedure in [Ng 2007a] using a 2D convolution between a US PSF and a map of scatterers, i.e, tissue reflectivity function (TRF).

4.4.1.1 Cartoon phantom image

For Group 1, the TRF was generated by assigning the scatterers random amplitudes following a given distribution, weighted by a cartoon image denoted by mask hereafter. A Laplacian distribution has been employed and the mask has been hand drawn to simulate four different regions with different echogenicity. The PSF was generated using a Field II [Jensen 1991] simulation corresponding to a 128-element linear probe operating at 3.5 MHz and an axial sampling frequency of 20 MHz. The resulting TRF and US image (plotted in B-mode) are shown in Fig. 4.1 (a) and (b). The compressed measurements were obtained by projecting the RF images onto orthogonal Structurally Random Matrix (SRM) [Do 2012] and were degraded by an additive Gaussian noise corresponding to a SNR of 40 dB. In order to evaluate the performance of the algorithm with a non-orthogonal measurement matrix, namely nSDMM, we have also projected the RF data onto a random Gaussian matrix. The corresponding results are provided in Fig. 4.1 (e), (h) and (k).

Sampling with Bernoulli masks In section 2.1.4.2, we have presented several existing CS acquisition schemes in US imaging. In order to show how the proposed method is able to handle such acquisition schemes, we give hereafter an example in Fig. 4.2. Based on the same simulated data as Group 1, the measurements were obtained by sampling with Bernoulli masks.

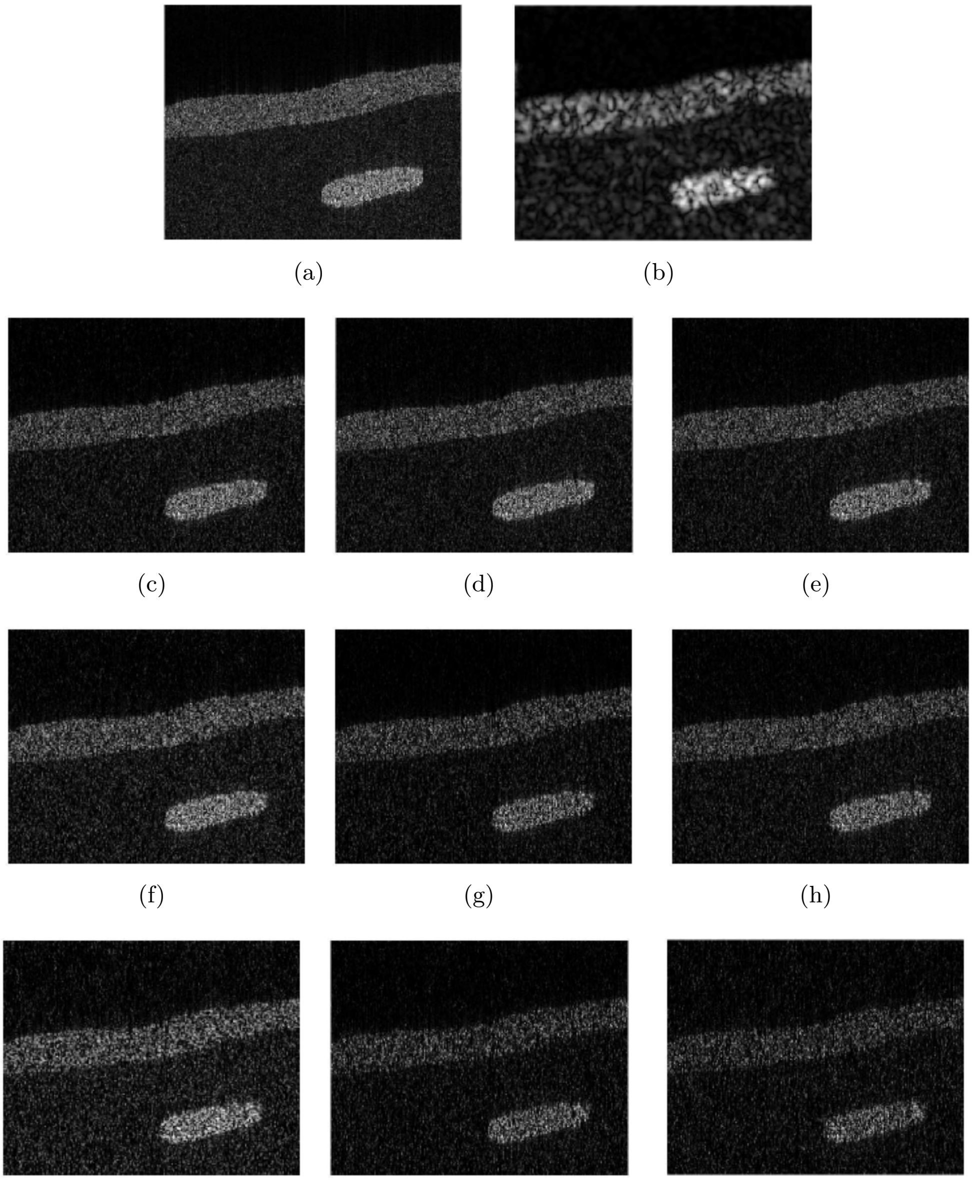
(a) (b)

(c) (d) (e)

(f) (g) (h)

(i) (j) (k)

Figure 4.1: Results on simulated data (Group 1). (a) TRF, (b) Simulated US image, (c,f,i) Reconstruction results using ADMM for CS ratios of 0.6, 0.4 and 0.2, (d,g,j) Reconstruction results using SDMM for CS ratios of 0.6, 0.4 and 0.2, (e,h,k) Reconstruction results using nSDMM for CS ratios of 0.6, 0.4 and 0.2.

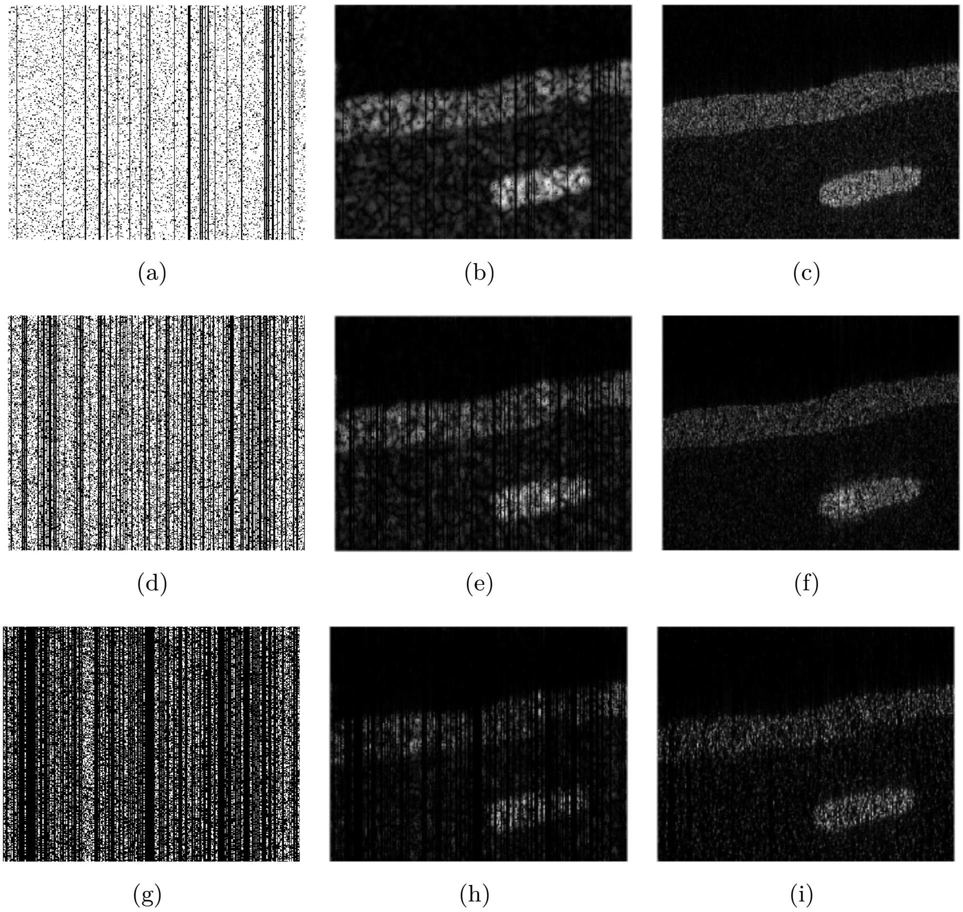

(a) (b) (c)

(d) (e) (f)

(g) (h) (i)

Figure 4.2: Results with Bernoulli masks on simulated data (Group 1). (a,b,c) Bernoulli mask, CS measurements and reconstruction using proposed method with CS ratio of 0.8, (d,e,f) Bernoulli mask, CS measurements and reconstruction using proposed method with CS ratio of 0.5, (g,h,i) Bernoulli mask, CS measurements and reconstruction using proposed method with CS ratio of 0.2.

4.4.1.2 Simulated kidney image

The PSF for Group 2 was also generated with Field II [Jensen 1991] and corresponds to a sectorial probe with the central frequency of 4 MHz and an axial sampling frequency of 40 MHz. The TRF follows one of the examples proposed by the Field II simulator [34], mimicking a kidney. The sampling matrix considered was a Structurally Random Matrix (SRM) [Do 2012] and the SNR was set at 40 dB. The TRF and the simulated US image are displayed in Fig. 4.3 (a) and (e).

4.4.1.3 Results' discussion

Fig. 4.1 and Fig. 4.3 display the compressive deconvolution reconstruction results obtained with different methods for CS ratios of 0.6, 0.4 and 0.2. The value of p used to regularize the TRF estimations was set to 1 for Group 1 and 1.5 for Group 2. All the other hyperparameters were set to their best possible values by cross-validation. We should note that since both ADMM and SDMM methods aim at solving the same objective function in (4.2), the hyperparameters α and μ have been assigned the same values in order to ensure a fair comparison. For the same reason, both algorithms were assigned the same convergence criterion, *i.e.* $\| \boldsymbol{x}^k - \boldsymbol{x}^{k-1} \| / \| \boldsymbol{x}^{k-1} \| < 5e^{-4}$, with k the iteration number and $\boldsymbol{x}_k$ the estimated image at iteration k.

Taking benefit from the fact that the TRF ground truth is available in simulation experiments, the PSNR and SSIM are also used in this subsection to assess the quality of the reconstruction results. The definition of PSNR and SSIM can be found as (3.28) and (3.29). Higher PSNR or SSIM indicates that the reconstruction is of higher quality. The definition of PSNR and SSIM can be found in section.3.6.1.

These quantitative results are regrouped in Table 4.1, where the reported PSNRs and SSIMs are the mean values of 10 experiments. The bold values stand for the best result obtained for each experiment. Note that given the more complex structures in Group 2, the intrinsic values of PSNR and SSIM are lower for Group 2 than for Group 1. However, the improvement between SDMM and ADMM is globally higher for Group 2 than for Group 1.

Both the visual inspection of images in figures 4.1 and 4.3 and the quantitative results in Table 4.1 show that the proposed SDMM-based method outperforms the ADMM algorithm for the two simulated images and for all the CS ratios. In addition to the reconstruction quality gain, the proposed method also offers better convergence properties compared to ADMM. This convergence improvement is clearly highlighted by the plots in Fig. 4.4. We may thus remark that for all the CS ratios, the convergence curves, both in terms of objective function (as eq. (4.2)) and of Normalized Mean Square Error (NMSE) defined in eq.(4.22), decreases much faster with SDMM than with ADMM. The computations were performed using a computer with Intel Xeon CPU E5620 @2.40GHz, 4.00G RAM. Depending on the stopping criterion, the convergence rate of SDMM for Group 1 is at least twice faster than the one of ADMM. We emphasize that the same convergence properties have been obtained for Group 2. The convergence performance of nSDMM is also shown in Fig. 4.4. We may remark that nSDMM has degraded con-

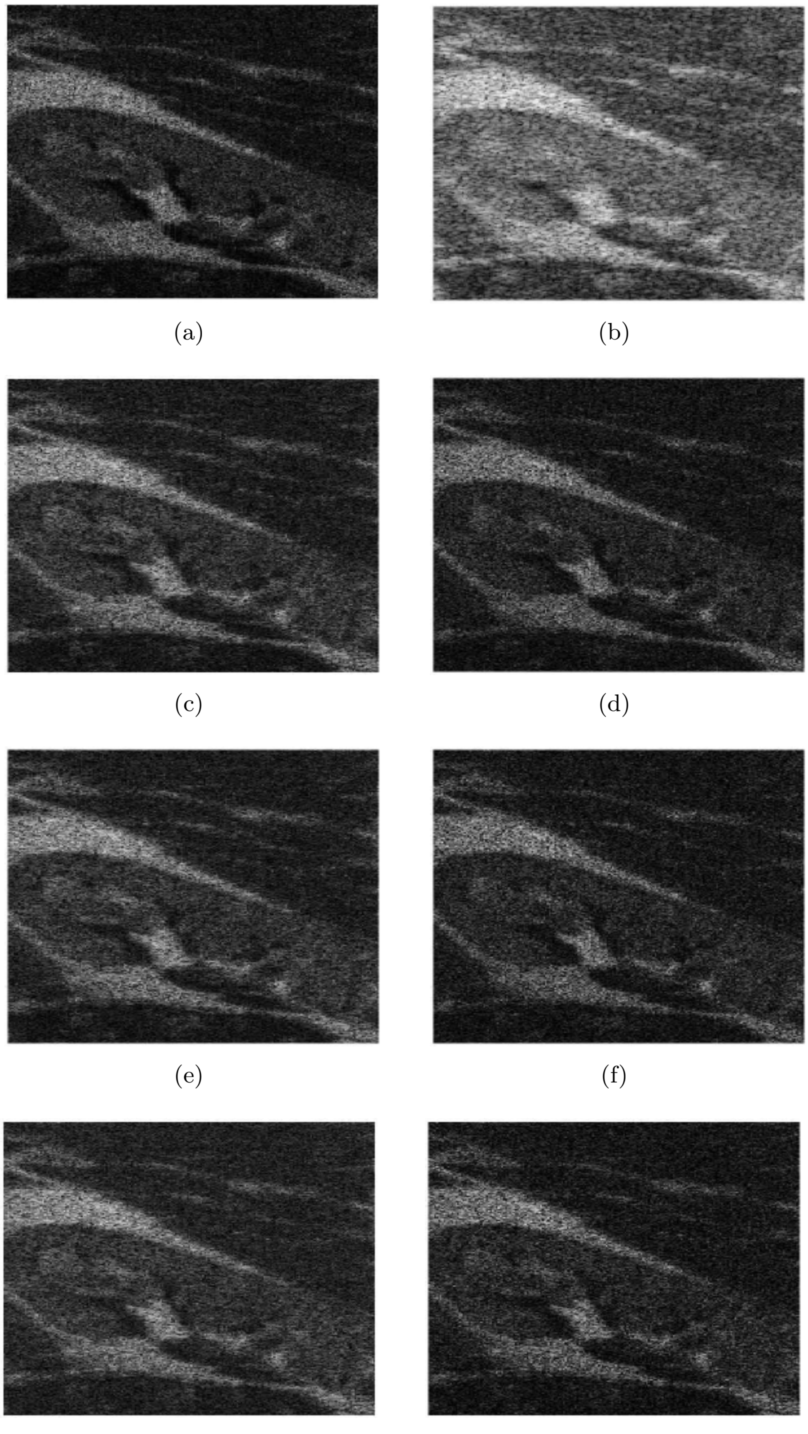

(a) (b)

(c) (d)

(e) (f)

(g) (h)

Figure 4.3: Results on simulated data (Group 2). (a) TRF, (b-d) Reconstruction results using ADMM for CS ratios of 0.6, 0.4 and 0.2, (e) Simulated US image, (f-h) Reconstruction results using SDMM for CS ratios of 0.6, 0.4 and 0.2.

Table 4.1: Quantitative results for compressive deconvolution reconstruction of simulated US images

	CS ratios	0.8	0.6	0.4	0.2
Group 1					
ADMM	PSNR(dB)	29.14	28.34	27.01	24.60
	SSIM(%)	81.58	77.44	69.07	51.65
SDMM	PSNR(dB)	**30.67**	**29.55**	**27.94**	**26.18**
	SSIM(%)	**85.77**	**81.66**	**74.37**	**63.15**
Group 2					
ADMM	PSNR(dB)	28.02	26.89	26.20	25.32
	SSIM(%)	60.56	58.20	54.21	45.35
SDMM	PSNR(dB)	**31.53**	**30.95**	**30.19**	**28.10**
	SSIM(%)	**76.85**	**74.45**	**70.40**	**56.20**

vergence properties compared to SDMM method, caused by the approximation in (4.20). However, when the convergence is achieved, both objective function value and NMSE obtained with nSDMM and SDMM are similar.

$$NMSE = \frac{1}{N} \parallel \boldsymbol{x} - \hat{\boldsymbol{x}} \parallel_2^2 \tag{4.22}$$

where $\boldsymbol{x}$ and $\hat{\boldsymbol{x}}$ are the normalized original and reconstructed TRF images and N represents the number of pixels in the image.

As explained previously, the value of the regularization parameter p has been manually tuned in the two simulated experiments. However, one may notice the importance of this parameter on the reconstruction results, as it directly affects the regularization of the TRF [Achim 2014]. In order to show its influence on the results, we regroup in Fig. 4.5 the PSNR and SSIM results for both SDMM and ADMM methods for three values of p, versus the CS ratio. In addition to the superiority of SDMM compared to ADMM, one may remark that the choice of p is more important for low CS ratios. This observation can be explained by the further importance of the regularization when only a small amount of data is available.

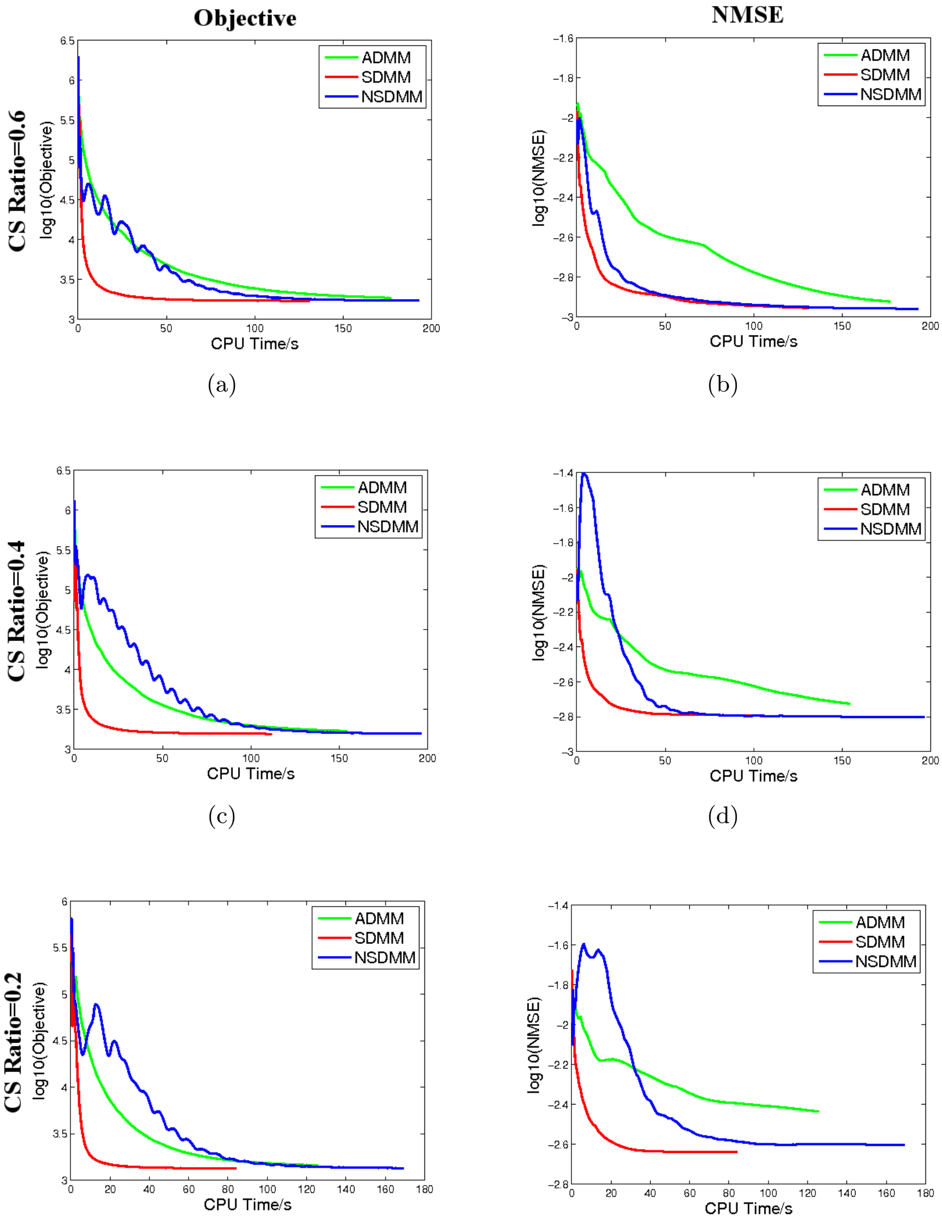

(a) (b)

(c) (d)

(e) (f)

Figure 4.4: Convergence performance on simulated data (Group1). (a,c,e) Objective vs CPU time for CS ratios of 0.6, 0.4, 0.2, (b,d,f) NMSE vs CPU time for CS ratios of 0.6, 0.4, 0.2.

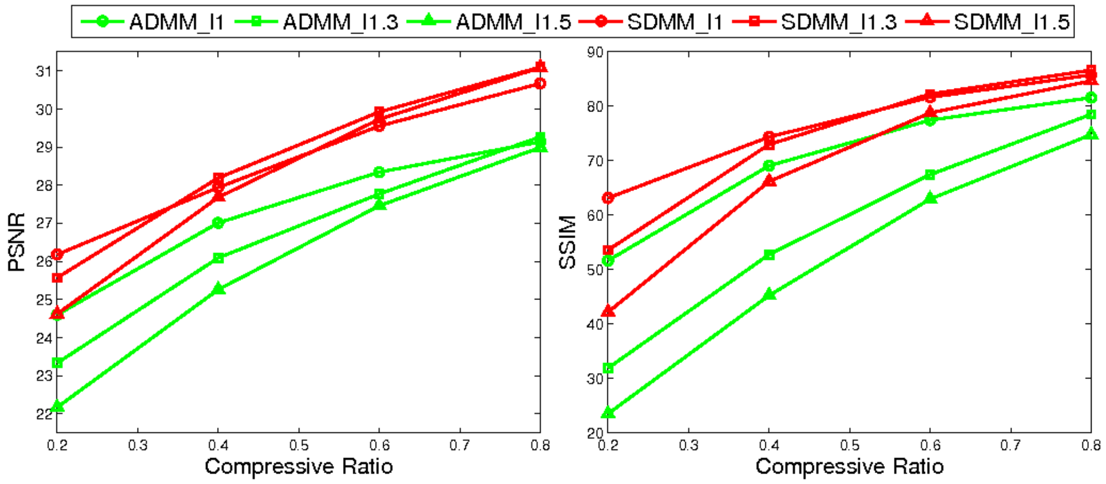

Figure 4.5: Results of all the methods with different p on simulated data (Group1).

4.4.2 Results on *in vivo* data

In this section, we evaluate the results of the proposed SDMM-based compressive deconvolution method on two *in vivo* US images, denoted by Group 3 and Group 4. Group 3 corresponds to a mouse bladder shown in Fig. 4.6 (a), while Group 4 represents a mouse kidney, see Fig. 4.7 (a). Both images were acquired with a 20 MHz single-element US probe. Since the PSF is unknown in practical situations, it has been initially estimated from the data, as a pre-processing step, following the PSF estimation procedure presented in [Michailovich 2005]. The compressive deconvolution results obtained with ADMM and SDMM are shown in figures 4.6 (b-g) and 4.7 (b-g) for CS ratios of 0.8, 0.6 and 0.4. Given the "sparse" appearance of the mouse bladder caused by the weak amount of scatterers in the liquid, the value of p was set to 1 for Group 3 and to 1.5 for Group 4.

For the *in vivo* data, the true TRFs are obviously not available, making thus impossible the computation of quantitative results such as the PSNR or the SSIM. As a consequence, the quality of the compressive deconvolution results is evaluated in this section according to the standard contrast-to-noise ratio (CNR) and the resolution gain (RG) proposed in [Yu 2012]. The RG is the ratio of the normalized auto correlation (higher than -3 dB) of the original RF US image to the normalized auto correlation (higher than -3 dB) of the reconstructed TRF. Moreover, CPU times for both ADMM and SDMM reconstructions are shown in Table 4.2. The CNR values were computed for the regions highlighted by the red or orange rectangles in Figures 4.6 and 4.7. For instance, two CNRs have been calculated for Group 3, between one region in the bladder cavity and respectively two regions extracted from the bladder wall. The numbers in Table 4.2 show equivalent results between ADMM and SDMM. Nevertheless, SDMM was roughly 2 to 6 times faster than ADMM, due to its better convergence properties discussed in the previous section. The contrast of the reconstructed images is shown to be better, in terms of CNR, than the one of the original B-mode images. Moreover, the RG computed between the estimated TRFs and the original images is always larger than 1. This demonstrates the ability of our compressive deconvolution method to improve the spatial resolution.

The visual inspection of the results highlights better denoising achievements with SDMM compared to ADMM, as for example in weak scatterer regions such as the bladder cavity. We emphasize that the reconstructed TRF in Figures 4.6 and 4.7 are shown after envelope detection and log compression, in order to be comparable to the standard B-mode images. However, the deconvolution process results into TRFs that, contrary to RF images, are not longer modulated in the axial direction. Indeed, the carrier information is included in the PSF that is eliminated during the deconvolution process. For this reason, the standard procedure of envelope detection based on the amplitude of the complex analytic signal, is not adapted to TRF. Instead, we have used an envelope estimator based on the detection and interpolation of local maximum, classically used in empirical mode decomposition techniques [Flandrin 2004].

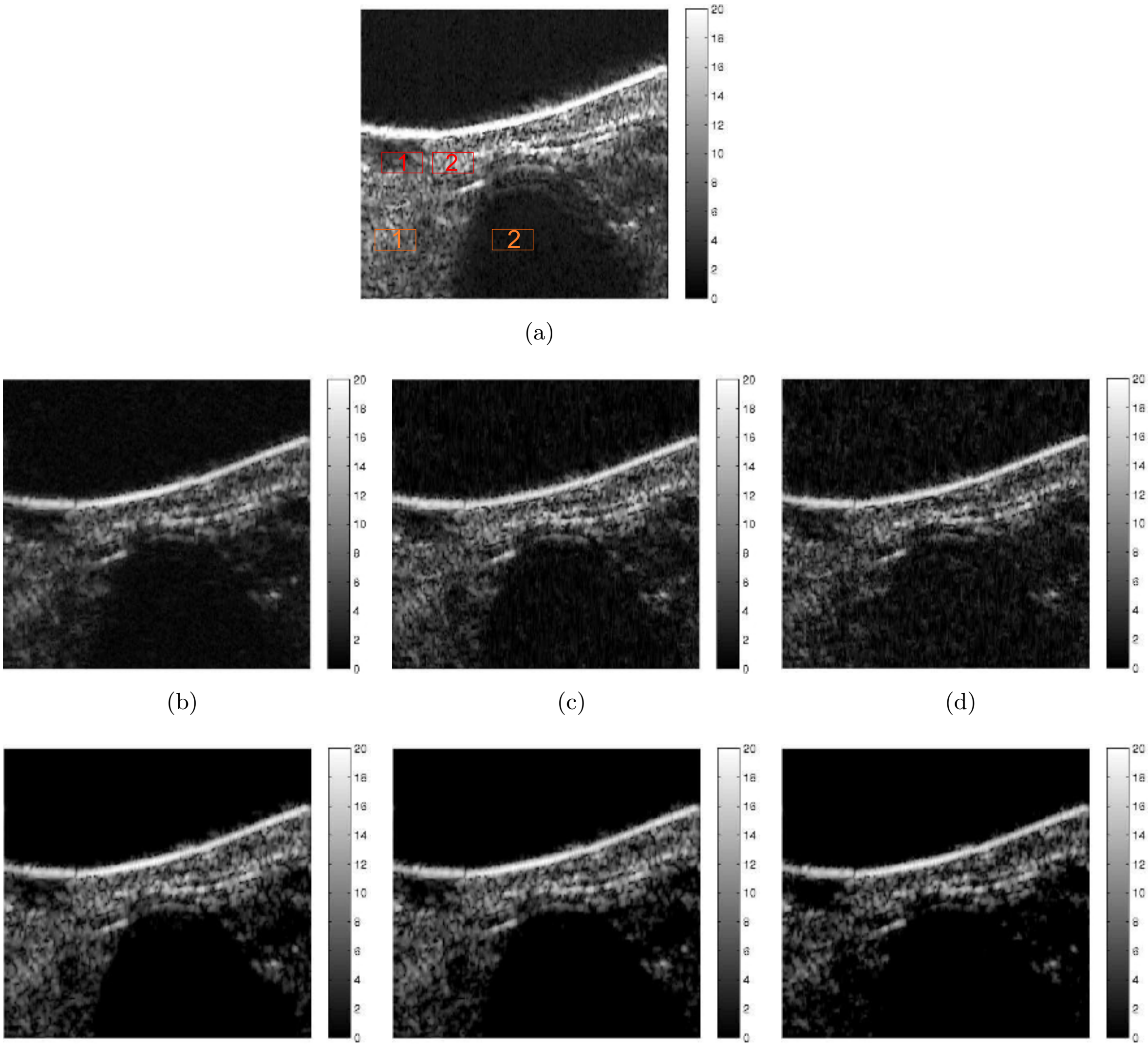

(a)

(b)

(c)

(d)

(e)

(f)

(g)

Figure 4.6: Results on *in vivo* data (Group 3). (a) Original US image, (b-d) Reconstruction results using ADMM for CS ratios of 0.8, 0.6 and 0.4, obtained for $p = 1$, (e-g) Reconstruction results using SDMM for CS ratios of 0.8, 0.6 and 0.4, obtained for $p = 1$.

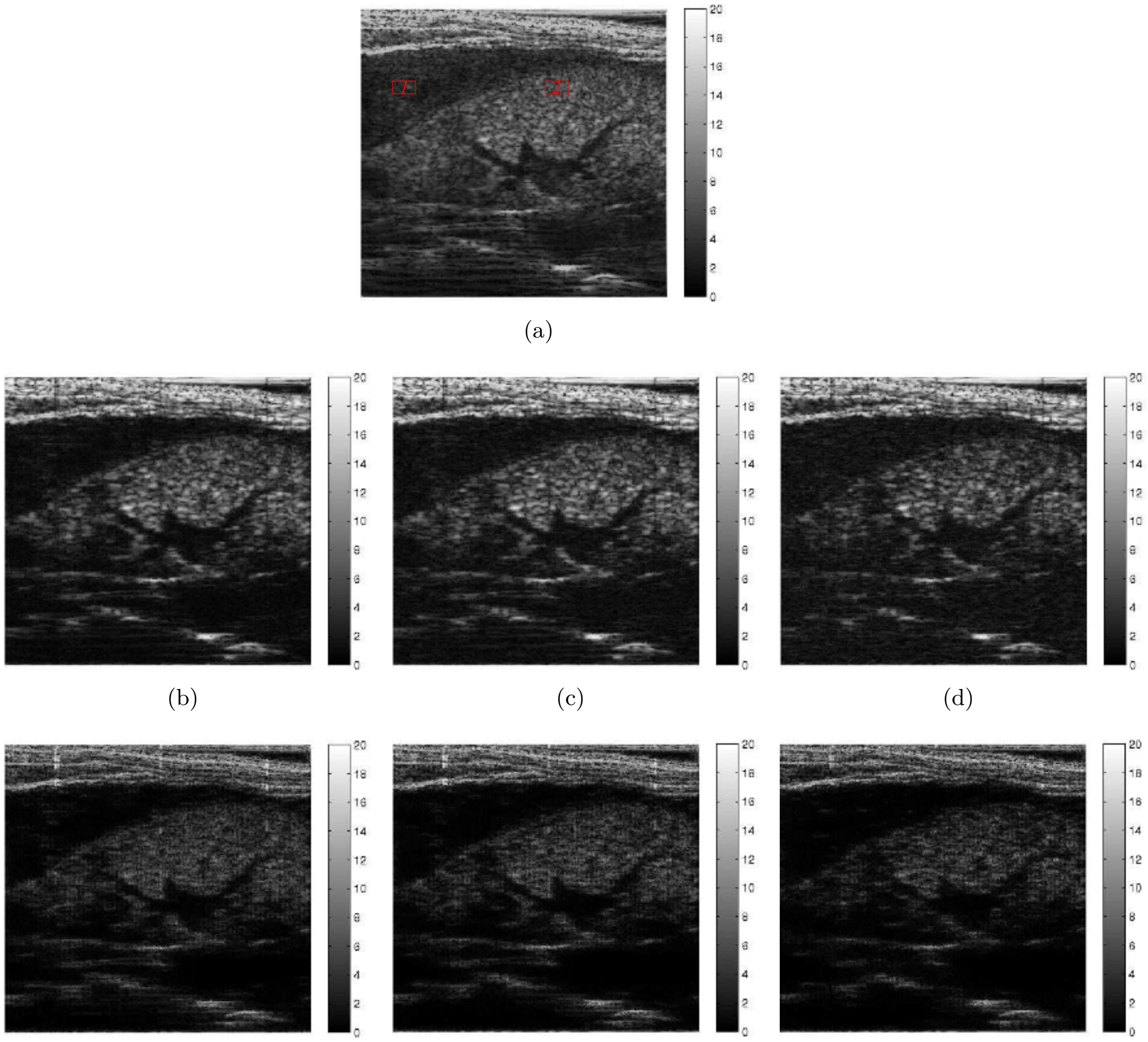

(a)

(b) (c) (d)

(e) (f) (g)

Figure 4.7: Results on *in vivo* data (Group 4). (a) Original US image, (b-d) Reconstruction results using ADMM for CS ratios of 0.8, 0.6 and 0.4, obtained for $p = 1.5$, (e-g) Reconstruction results using SDMM for CS ratios of 0.8, 0.6 and 0.4, obtained for $p = 1.5$.

Table 4.2: Quantitative results for the *in vivo* data

Images		Group 3				Group 4		
Criterion		CNR1	CNR2	RG	Time/s	CNR	RG	Time/s
Original		1.41	2.62	1.00	-	1.48	1.00	-
ADMM	1	**1.65**	2.51	2.32	76.40	**1.98**	2.69	629.57
	0.8	**1.63**	2.00	2.39	77.36	**1.90**	2.68	561.20
	0.6	**1.57**	1.52	2.45	100.88	1.77	2.34	484.93
	0.4	1.40	1.10	2.50	112.96	1.40	2.68	343.09
SDMM	1	1.61	**2.56**	**3.30**	**12.90**	1.90	**3.50**	**186.64**
	0.8	1.60	**3.28**	**2.39**	**17.62**	1.87	**3.61**	**216.66**
	0.6	1.54	**2.62**	**2.81**	**24.89**	**1.84**	**3.89**	**265.43**
	0.4	**1.52**	**2.07**	**3.17**	**40.57**	**1.58**	**4.17**	**312.12**

4.5 Conclusion

The main objective of this chapter was to propose an SDMM-based algorithm dedicated to solve the compressive deconvolution problem in US imaging which is able to reconstructing enhanced US images from compressed measurements. Compared to an ADMM-based method that we have presented in the previous chapter, the proposed algorithm requires one less hyperparameter since one of the optimization subproblems can be solved without any approximation. Moreover, the proposed variable splitting scheme made possible by SDMM is shown to allow faster convergence compared to ADMM. Finally, an alternative to compressed measurements obtained with non-orthogonal matrices is provided, thus extending the practical interest of the compressive deconvolution approach.

Chapter 5

Compressive Blind Deconvolution

Contents

5.1 Introduction

In the previous two chapters, two algorithms were proposed to solve the compressive deconvolution problem with the assumption that the PSF was known or could be estimated in a pre-processing step. Obviously, the PSF cannot be perfectly known in practical situations. As described in section 2.2.3, blind deconvolution includes two classed approaches. The first identifies the PSF in a precede step and later use it in combination with one of the non-blind deconvolution. The second estimates the target image and the PSF simultaneously. Following the idea of joint image reconstruction and PSF estimation, we present in this chapter an approach for compressive blind deconvolution.

5.2 Optimization Problem Formulation

Inspired by the existing joint identification methods for blind deconvolution problem (see (2.34) in section 2.2.3.2) and the *priori* information on the PSF adopted in [Morin 2013b, Repetti 2015], we formulate the compressive blind deconvolution problem as below.

$$\begin{aligned} &\underset{\boldsymbol{x}\in\mathbb{R}^N,\boldsymbol{a}\in\mathbb{R}^N,\boldsymbol{h}\in\mathbb{R}^n}{min} \parallel \boldsymbol{a} \parallel_1 + \alpha P(\boldsymbol{x}) + \gamma \parallel \boldsymbol{h} \parallel_2^2 + \frac{1}{2\mu} \parallel \boldsymbol{y} - \Phi\Psi\boldsymbol{a} \parallel_2^2 \\ &s.t. \quad H\boldsymbol{x} = \Psi\boldsymbol{a} \end{aligned} \tag{5.1}$$

where all the variables have the same significance as in the previous chapters and γ is a hyper-parameter weighting the energy term envolving the PSF. As described in the previous chapters, the first term aims at imposing the sparsity of the RF data $H\boldsymbol{x}$ in a transformed domain Ψ, the second and the third terms represent the *prior* information on the target image $\boldsymbol{x}$ and the PSF $\boldsymbol{h}$ respectively. In US imaging, instead of the general total variation as used in [Amizic 2013], an ℓ_p-norm was adopted to adjust the GGD statistics of the TRF. Inspired by [Morin 2013b, Repetti 2015], we employed an ℓ_2-norm to regularize the PSF.

Compared to the compressive deconvolution problem in (3.4), this objective function in no longer a convex optimization problem. We hereafter present a dedicated algorithm to solve this problem.

5.3 Alternating Minimization (AM)-based algorithm

The aforementioned objective function in (5.1) can be divided into two sub-problems by using the Alternating Minimization (AM)-based algorithm [Wang 2008]. The first sub-problem, aiming to estimate $\boldsymbol{a}$ and $\boldsymbol{x}$ for a fixed $\boldsymbol{h}$ at kth iteration, is:

$$\begin{aligned}(\boldsymbol{x}^{k+1}, \boldsymbol{a}^{k+1}) = \underset{\boldsymbol{x}\in\mathbb{R}^N, \boldsymbol{a}\in\mathbb{R}^N}{argmin} \parallel \boldsymbol{a} \parallel_1 + \alpha P(\boldsymbol{x}) + \frac{1}{2\mu} \parallel \boldsymbol{y} - \Phi\Psi\boldsymbol{a} \parallel_2^2 \\ s.t. \quad H^k\boldsymbol{x} = \Psi\boldsymbol{a}\end{aligned} \tag{5.2}$$

This sub-problem is in fact the same with the compressive deconvolution problem addressed in the previous chapters. Both ADMM-based and SDMM-based algorithms are able to get an optimal $\boldsymbol{x}$ and $\boldsymbol{a}$ by solving the unconstrained form of this optimization problem:

$$\boldsymbol{x}^{k+1} = \underset{\boldsymbol{x}\in\mathbb{R}^N}{argmin} \parallel \Psi^{-1}H\boldsymbol{x} \parallel_1 + \alpha P(\boldsymbol{x}) + \frac{1}{2\mu} \parallel \boldsymbol{y} - \Phi H\boldsymbol{x} \parallel_2^2 \tag{5.3}$$

$$\boldsymbol{a}^{k+1} = \Psi H\boldsymbol{x}^{k+1} \tag{5.4}$$

The second sub-problem concerns the estimation of $\boldsymbol{h}$ for fixed $\boldsymbol{a}$ and $\boldsymbol{x}$

$$\boldsymbol{h}^{k+1} = \underset{\boldsymbol{h}\in\mathbb{R}^n}{argmin} \gamma \parallel \boldsymbol{h} \parallel_2^2 \quad s.t. \quad X^{k+1}P\boldsymbol{h} = \Psi\boldsymbol{a}^{k+1} \tag{5.5}$$

where $X^{k+1} \in \mathbb{R}^{N\times N}$ is a Block Circulant with Circulant Block (BCCB) matrix with the same structure as H. Its circulant kernel is $x^{k+1} \in \mathbb{R}^N$, $P \in \mathbb{R}^{N\times n}$ is a simple structure matrix mapping the n coefficients of the PSF kernel $\boldsymbol{h}$ to a N length vector so that $Hx^{k+1} = X^{k+1}P\boldsymbol{h}$. Its definition and implementation can be found in Appendix A. The constrained problem above can be solved by reformulating it as an unconstrained one:

$$\boldsymbol{h}^{k+1} = \underset{\boldsymbol{h}\in\mathbb{R}^n}{argmin} \quad \gamma \parallel \boldsymbol{h} \parallel_2^2 + \parallel X^{k+1}P\boldsymbol{h} - \Psi\boldsymbol{a}^{k+1} \parallel_2^2 \tag{5.6}$$

It thus becomes a regularized least square problem and its analytical solution can be written as [Morin 2013b]:

$$\boldsymbol{h}^{k+1} = [(X^{k+1}P)^t X^{k+1}P + \gamma I_n]^{-1}(X^{k+1}P)^t\Psi\boldsymbol{a}^{k+1} \tag{5.7}$$

where $I_n \in \mathbb{R}^n$ is an identity matrix. Instead of inverting the $N \times N$ matrix, we hereby only need to deal with the inversion of an $n \times n$ matrix. Thus the computational cost is reduced. More details about the practical implementation of the analytic solution in (5.7) can be found in Appendix B.

To conclude, the AM-based algorithm for compressive blind deconvolution is summarized in Algorithm 4.

Algorithm 4 Compressive blind deconvolution AM-based algorithm.

```
Input: $\boldsymbol{h}^0$, $\alpha$, $\mu$, $\beta$, $\gamma$
while not converged do
    $\boldsymbol{x}^{k+1}, \boldsymbol{a}^{k+1} \leftarrow \boldsymbol{h}^k$        ▷ update $\boldsymbol{x}^{k+1}$, $\boldsymbol{a}^{k+1}$ using Algorithms 2 or 3
    $\boldsymbol{h}^{k+1} \leftarrow \boldsymbol{x}^{k+1}, \boldsymbol{a}^{k+1}$        ▷ update $\boldsymbol{h}^{k+1}$ using (5.7)
end while
Output: $\boldsymbol{x}, \boldsymbol{a}, \boldsymbol{h}$
```

5.4 Results

In this section, we provide a preliminary evaluation through two numerical experiments of the performance of the proposed compressive blind deconvolution method, denoted by CBD_AM hereafter. The first simulation is based on the Shepp-Logan phantom and serves to compare our approach to the method in [Amizic 2013], referred as CBD_Amizic hereafter. Second, we test our algorithm on a simulated US image, showing the effectiveness of our approach compared to compressive non-blind deconvolution.

5.4.1 Results on Shepp-logan phantom

In this subsection we show an experiment aiming to evaluate the performance of the proposed approach compared to CBD_Amizic. The comparison results are obtained on the standard 256×256 Shepp-Logan phantom. As described in section 3.6.2, the measurements have been generated in a similar manner as in [Amizic 2013], *i.e.* the original image was normalized, degraded by a 17×17 Gaussian PSF with variance of 9, projected onto a structured random matrix (SRM) to generate the CS measurements. Finally, the compressed measurements were corrupted by an additive Gaussian noise. We should remark that in [Amizic 2013] the compressed measurements were originally generated using a Gaussian random matrix. However, we have found that the reconstruction results with CBD_Amizic are slightly better when using a SRM compared to the PSNR results reported in [Amizic 2013]. Both methods were based on the generalized TV to model the image to be estimated and the 3-level Haar wavelet transform as sparsifying basis Ψ. With our method, the ADMM-based (Algorithm 2) approach was employed to update the $\boldsymbol{x}$ and $\boldsymbol{a}$. Interestingly, although the SDMM-based method is shown faster converged compared to the ADMM-based method in the previous chapter, the latter one performs better than the former one in this experiment. Hyperparameters were set to $\{\alpha, \mu, \beta, \gamma\} = \{10^{-1}, 10^{-4}, 10^{-4}, 1\}$. The same hyperparameters as reported in [Amizic 2013] were used for CD_Amizic. Both algorithms used the same stopping criteria.

Fig. 5.1 shows the original Shepp-Logan image, its blurred version and a series of compressive deconvolution reconstructions using both our method and CBD_Amizic for CS ratios running from 0.4 to 0.8 and a SNR of 40 dB. Additionally, in Fig. 5.2, we provided the estimated PSFs together with the true Gaussian PSF of variance 9 used to degrade the original images and the initial Gaussian PSF of variance 2 as used in

[Amizic 2013]. Table 5.1 regroups the PSNR of the estimated $\boldsymbol{x}$ and $\boldsymbol{h}$ obtained with our method and with CBD_Amizic for four CS ratios from 0.2 to 0.8 when SNR is equal to 40dB. In each case, the reported PSNRs are the mean values of 10 experiments. We may observe that our method outperforms CBD_Amizic in all the cases. Moreover, Table 5.1 also shows the computational times with CBD_Amizic and the proposed method, obtained with Matlab implementations (for CBD_Amizic, the original code provided by the authors of [Amizic 2013] has been employed) on a standard desktop computer (Intel Xeon CPU E5620 @ 2.40GHz, 4.00G RAM). We notice that our approach is less time consuming than CBD_Amizic for all the CS ratios considered.

Table 5.1: Quantitative assessment for Shepp-Logan phantom

Methods	CS ratios	PSNRx	PSNRh	Time/s
CBD_Amizic	80%	22.55	86.86	353.64
	60%	22.48	86.49	415.96
	40%	22.38	86.18	535.59
	20%	19.80	82.41	534.34
CBD_AM	80%	**24.39**	**92.41**	**243.31**
	60%	**23.12**	**89.70**	**320.82**
	40%	**22.59**	**88.36**	**321.39**
	20%	**21.48**	**85.96**	**329.90**

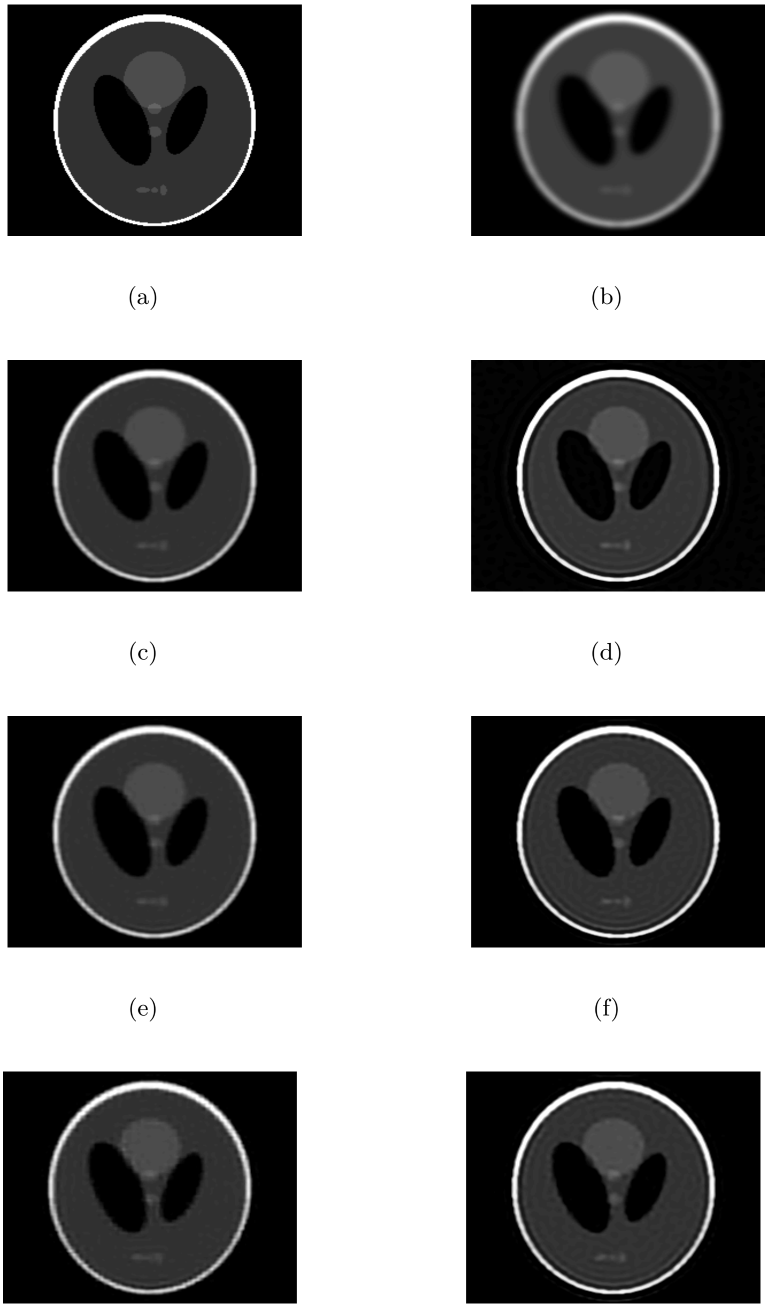

(a) (b)

(c) (d)

(e) (f)

(g) (h)

Figure 5.1: Results on Shepp-logan phantom. (a) Original, (b) blurred, (c,e,g) reconstruction results with CBD_Amizic for CS ratios of 0.8, 0.6 and 0.4, (d,f,h) reconstruction results with AM_ADMM for CS ratios of 0.8, 0.6 and 0.4.

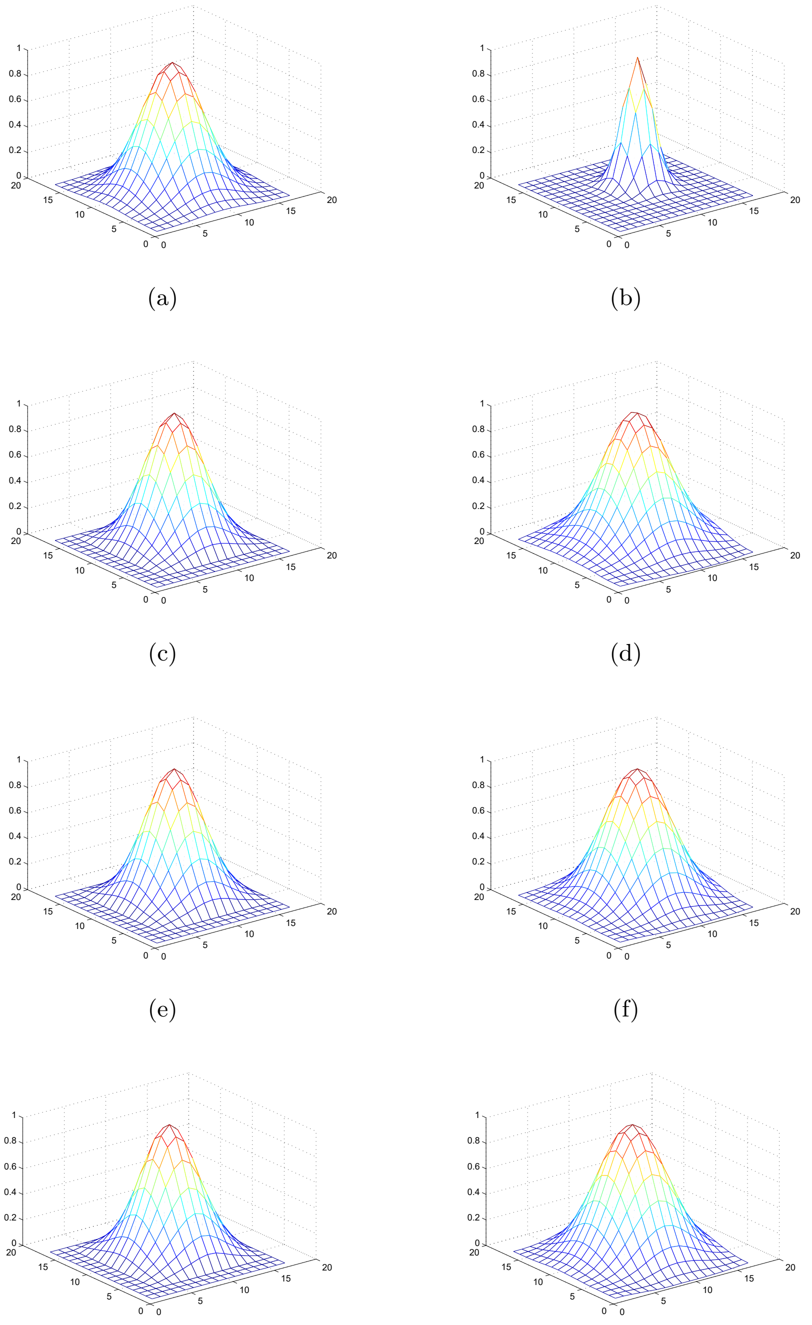

(a) (b) (c) (d) (e) (f) (g) (h)

Figure 5.2: Estimated PSFs for compressive blind deconvolution presented in Fig. 5.1. (a) Original, (b) initial, (c,e,g) estimated PSFs with CBD_Amizic for CS ratios of 0.8, 0.6 and 0.4, (d,f,h) estimated PSFs with CBD_AM for CS ratios of 0.8, 0.6 and 0.4.

5.4.2 Results on simulated US images

In this section, we tested the proposed CBD_AM method on one simulated US image. We should keep in mind that since the CBD_Amizic method using a generalized TV prior is not well suited to model the TRF in imaging (see section 3.6.3), we did not use it in the following simulation.

As an initial investigation, we generated hereby a B-mode US image by 2D convolution between a spatially invariant Gaussian PSF of variance 2 and a TRF, shown in Fig. 5.3. The TRF corresponds to a simple medium representing a round hypoechoic inclusion into a homogeneous medium, as described in section 3.6.4. The scatterer amplitudes were random variables distributed according to a GGD with the shape parameter set to 1. The compressed measurements were then obtained by projecting the RF images onto a SRM, aiming at reducing the amount of data available.

In order to evaluate the performance of the proposed method, we compared the blind reconstruction results with the one without updating the PSF estimation, *i.e.* the compressive non-blind deconvolution (denoted by CD). As it is done in the previous two chapters with *in vivo* data, the initial PSF used here is also estimated from the blurred data as a pre-processing step following the PSF estimation procedure presented in [Michailovich 2005]. We employed the SDMM-based compressive deconvolution method in this experiment to update $\boldsymbol{x}$ and $\boldsymbol{a}$.

The reconstruction results of the compressive non-blind deconvolution and the proposed method are presented in Fig. 5.4. We have also displayed the true, initial and estimated PSFs in Fig. 5.5. One may remark from the images and the quantitative results in Table 5.2 that the CBD_AM is able to recover both TRF and PSF with good accuracy.

Table 5.2: Quantitative assessment for simulated US data

Methods	CS ratios	PSNRx	SSIM	PSNRh
CD	80%	21.31	**50.64**	20.84
	60%	21.25	45.87	
	40%	20.81	40.48	
	20%	19.77	29.46	
CBD_AM	80%	**23.83**	48.41	**27.71**
	60%	**23.34**	**47.01**	**27.64**
	40%	**22.94**	**48.64**	**27.00**
	20%	**22.02**	**52.50**	**22.18**

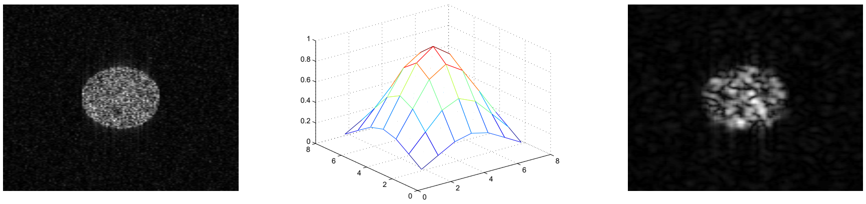

(a) (b) (c)

Figure 5.3: (a) TRF (256 × 128), (b) Gaussian PSF (7 × 7 central part) and (c) Simulated B-mode US image.

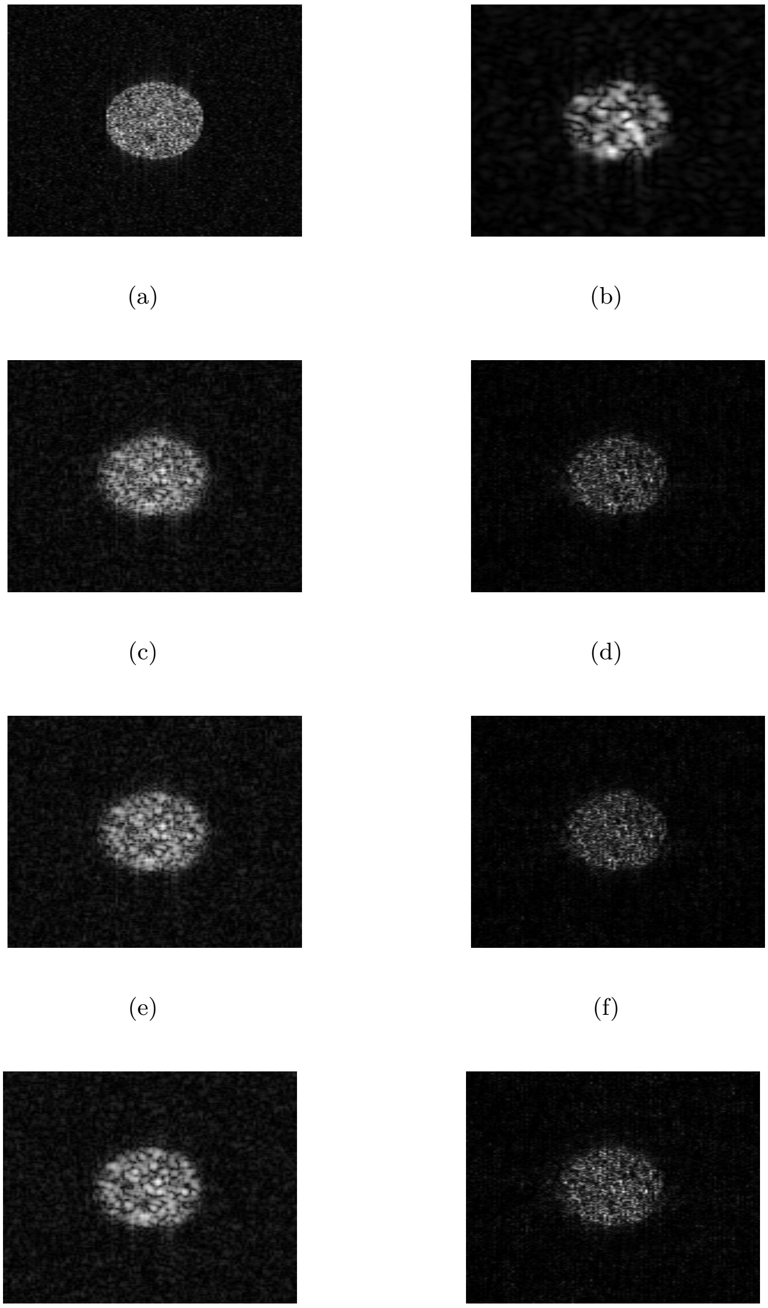

(a) (b)

(c) (d)

(e) (f)

(g) (h)

Figure 5.4: Simulated US image and its compressive blind deconvolution results for a SNR of 40 dB. (a) Original tissue reflectivity function, (b) Simulated B-mode US image, (c,e,g) results using CD with a pre-estimated PSF for CS ratios of 0.8, 0.6 and 0.4, (d,f,h) results using CBD_AM for CS ratios of 0.8, 0.6 and 0.4.

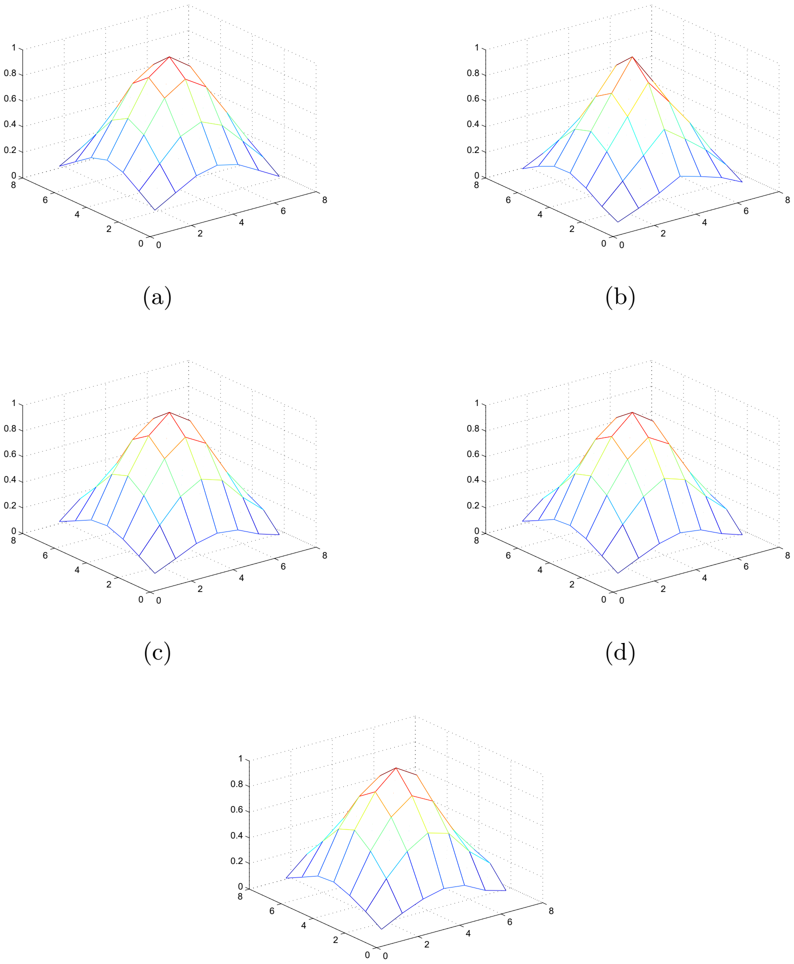

(a)

(b)

(c)

(d)

(e)

Figure 5.5: Estimated PSFs using CBD_AM for compressive blind deconvolution. (a) True PSF, (b) estimated PSF using an existing method [Michailovich 2005], (c,d,e) estimated PSF of CBD_AM for CS ratios of 0.8, 0.6 and 0.4.

5.5 Conclusion

In this chapter, we gave an initial investigation to a compressive blind deconvolution algorithm. The proposed AM-based approach is composed by two parts with a initial guess of PSF. The first part is to estimate the TRF and the sparse representation of the blurred US RF image, which can be completed by either the ADMM-based or SDMM-based method. The second part is to update the PSF estimation by solving an analytical equation. Simulation results on the standard Shepp-Logan phantom show the superiority of our method, both in accuracy and in computational time, over a recently published compressive deconvolution approach. Moreover, preliminary results on a simulated US image have also shown the efficiency of the proposed approach on both TRF and PSF estimation.

Chapter 6

Conclusions and Perspectives

6.1 Conclusions

The goal of this work was to propose a framework for reconstructing enhanced ultrasound images from compressed measurements, namely compressive deconvolution. Aside from the compressive sampling matrix, an US RF image was modelled as the convolution product between a TRF and a PSF. The objective of our work was then to estimate the TRF from compressed measurements.

We first assumed the PSF known or estimated in a precede step and formulated the inverse problem as a regularized unconstrained optimization problem. Compared to a standard compressive sampling reconstruction that operates in the sparse domain, our minimization problem combined the data attachment and two regularization terms. One of the regularizers promoted minimal ℓ_1-norm of the target image transformed by 2D convolution with a bandlimited ultrasound PSF. The second one is seeking for imposing GGD statistics on the TRF to be reconstructed. To obtain the optimal solution, we proposed an ADMM-based approach to split these three awkward terms and solve them in three sub-problems separately and iteratively. Simulation results on the standard Shepp-Logan phantom showed the superiority of our method, both in accuracy and in computational time, over a recently published compressive deconvolution approach. Moreover, we showed that the proposed joint CS and deconvolution approach is more robust than an intuitive technique consisting of first reconstructing the RF data and second deconvolving it. Promising results on *in vivo* data have also been obtained to demonstrate the effectiveness of our approach in practical situations.

In a second step, we proposed an SDMM-based algorithm to improve the reconstruction in the compressive deconvolution framework. Compared to the ADMM-based method, this method split the three terms completely and required one less hyperparameter since one of the optimization subproblems can be solved without any approximation. Moreover, simulation results on both simulated US images and *in vivo* data have proven that the proposed variable splitting scheme made possible by SDMM allows faster convergence compared to ADMM. Additionally, an alternative to compressed measurements obtained with non-orthogonal matrices is provided, thus extending the practical interest of the compressive deconvolution approach.

Our last contribution was to develop an algorithm to jointly estimate the TRF and PSF. Compared to the methods proposed previously, the PSF is supposed to be unknown. We employed an additional ℓ_2-norm term for PSF regularization in the corresponding optimization problem. Starting from an initial guess of PSF, we proposed an AM-based method to iteratively estimate the TRF and PSF. The TRF estimation step could be done by either ADMM-based or SDMM-based algorithm and the PSF was updated using an efficient implementation of an analytical solution. Simulation results on the standard Shepp-Logan phantom showed its superiority over an existing method. We have also investigated this method on a simulated US image and obtained encouraging results.

6.2 Perspectives

Our research on the feasibility of compressive deconvolution in US imaging has however some limitations and thus opens several research perspectives.

One of the limitations comes from the assumption of an invariant PSF. The 2D convolution model may not be valid over the entire image because of the spatially variant PSF. While in our work we focused on compressive image deconvolution based on spatially invariant PSF, a more complicated global model combining several local shift invariant PSFs represents an interesting perspective of our approach.

The second limitation concerns the validation of the compressive blind deconvolution algorithm. More experimental data should be processed in the future in order to further validate the efficiency of our methods in practical situations. In addition, different regularization for the PSF may be adopted and tested. It will become more attractive if we can extend it to 3D ultrasound imaging.

Moreover, an automatic choice of the optimal value of the regularization parameter p would be of great interest in practice. This optimal choice may be considered through statistical assumptions on the US images, such as the heavy-tailed distributions discussed in [Achim 2014]. While in this thesis we focused on p values larger than or equal to 1, the case $p < 1$ may be of interest in practical situations involving sparse US images. To handle both situations, we will mainly focus on an automatic selection of p embedded into both convex and non-convex optimization routines.

Finally, evaluating our reconstruction method with other existing setups for generating the compressed measurements, having a practical interest in decreasing the acquisition time instead of only reducing the amount of acquired data, is also of great interest. As an example, an interesting future research track will be to evaluate the compressive deconvolution with specific compressed measurements, such as those obtained by Xampling [Chernyakova 2014] or with optimized sparse arrays [Diarra 2013].

Appendix

Appendix A

Construction of the P matrix

For online PSF estimation, we write the convolution model as below [Morin 2013a]:

$$\boldsymbol{r} = XP\boldsymbol{h} + \boldsymbol{n} \tag{A.1}$$

where $\boldsymbol{r}, \boldsymbol{h}, \boldsymbol{n}$ are the observation, the PSF and the noise in vector forms respectively, $\boldsymbol{r}, \boldsymbol{n} \in \mathbb{R}^N$, $\boldsymbol{h} \in \mathbb{R}^n$. We should note that $n << N$. $X \in \mathbb{R}^{N \times N}$ is the BCCB matrix representing the original image $\boldsymbol{x}$ and $P \in \mathbb{R}^{N \times n}$ is a matrix defined to extend $\boldsymbol{h}$ to N. Let us denote the size of $\boldsymbol{x}$ and $\boldsymbol{r}$ as $N = S \times T$, and the size of the PSF kernel $\boldsymbol{h}$ as $n = s \times t$.

X has exactly the same structure with H, classically used in deconvolution problems. The P could be written by

$$P = \begin{bmatrix} P' \\ \bigcirc \end{bmatrix}$$

where $\bigcirc \in \mathbb{R}^{S(T-t) \times n}$ is a zero matrix and $P' \in \mathbb{R}^{St \times n}$ can be written like

$$P' = \begin{bmatrix} I_s & \boldsymbol{O}_s & \dots & \boldsymbol{O}_s \\ \boldsymbol{O}_{(S-s)s} & \boldsymbol{O}_{(S-s)s} & \dots & \boldsymbol{O}_{(S-s)s} \\ \boldsymbol{O}_s & I_s & \dots & \boldsymbol{O}_s \\ \boldsymbol{O}_{(S-s)s} & \boldsymbol{O}_{(S-s)s} & \dots & \boldsymbol{O}_{(S-s)s} \\ \vdots & \vdots & \ddots & \vdots \\ \boldsymbol{O}_s & \boldsymbol{O}_s & \dots & I_s \\ \boldsymbol{O}_{(S-s)s} & \boldsymbol{O}_{(S-s)s} & \dots & \boldsymbol{O}_{(S-s)s} \end{bmatrix}$$

where $\boldsymbol{O}_s$ represents a zero square matrix of size $s \times s$ and $\boldsymbol{O}_{(S-s)s}$ is a zero matrix of size $(S - s) \times s$, I_s is an identity square matrix of size $s \times s$.

Appendix B

Implementation of the analytical solution for PSF estimation

In Chapter 5, the analytical solution for PSF estimation is

$$\boldsymbol{h}^{k+1} = [(X^{k+1}P)^t X^{k+1}P + \gamma I_n]^{-1}(X^{k+1}P)^t \Psi \boldsymbol{a} \tag{B.1}$$

To simplify the notations, we will ignore the iteration number k and denote the $\boldsymbol{z} = \Psi\boldsymbol{a}$. The key to solve this equation is to find an efficient way to compute $(XP)^t XP$ and $(XP)^t\boldsymbol{z}$.

Firstly, for the term of $(XP)^t\boldsymbol{z}$, X^t is actually the circular matrix of the transformed $\boldsymbol{x}$. Let us denote the transformed $\boldsymbol{x}$ as $\boldsymbol{x}'$. $X^t\boldsymbol{z}$ is then the convolution between $\boldsymbol{x}'$ and $\boldsymbol{z}$. While $\boldsymbol{x}$ represents the 2D image $\boldsymbol{x}_{2D}$ in a vectorized version, $\boldsymbol{x}'$ corresponds to the transformed 2D image $\boldsymbol{x}'_{2D}$. We define $\boldsymbol{x}$ in 2D as:

$$\boldsymbol{x}_{2D} = \begin{bmatrix} x_{11} & x_{12} & x_{13} & \cdots & x_{1T} \\ x_{21} & x_{22} & x_{23} & \cdots & x_{2T} \\ x_{31} & x_{32} & x_{33} & \cdots & x_{3T} \\ \vdots & \vdots & \vdots & \ddots & \vdots \\ x_{S1} & x_{S2} & x_{S3} & \cdots & x_{ST} \end{bmatrix}$$

The transformation from $\boldsymbol{x}_{2D}$ to $\boldsymbol{x}'_{2D}$ usually includes flips both in horizontal and vertical directions. However, the exact details of these flips depend also on the way how we define the convolution, including its boundary condition and which part we take from the full convolution result. Here we will detail about the transformation in the case of circular convolution with periodic boundary extensions, and we take the center part of the full convolution. Then the $\boldsymbol{x}_{2D}$ can be obtained by flipping $\boldsymbol{x}$ twice: the first row to the last second and first column to the last second, which is equal to

$$\boldsymbol{x}'_{2D} = \begin{bmatrix} x_{(S-1)(T-1)} & x_{(S-1)(T-2)} & \cdots & x_{(S-1)1} & x_{(S-1)T} \\ x_{(S-2)(T-1)} & x_{(S-2)(T-2)} & \cdots & x_{(S-2)1} & x_{(S-2)T} \\ \vdots & \vdots & \ddots & \vdots & \vdots \\ x_{1(T-1)} & x_{1(T-2)} & \cdots & x_{11} & x_{1T} \\ x_{S(T-1)} & x_{S(T-2)} & \cdots & x_{S1} & x_{ST} \end{bmatrix}$$

According to the analysis about P above, P^t multiplying a vector is actually equivalent to choose several elements from a vector. In our case, P^t aims picking up the first s elements from every S elements until we get n elements.

Secondly, concerning the term P^tX^tXP, its result is actually a matrix of size $n \times n$. To avoid constructing the big matrix P or X during implementation, we can find a way to compute these $n \times n$ elements instead.

Let us denote $U = X^tX$, U is a symmetric matrix and has the structure:

$$U = \begin{bmatrix} U_1 & U_2 & U_3 & \dots & U_T \\ U_2 & U_1 & U_2 & \dots & U_{T-1} \\ U_3 & U_2 & U_1 & \dots & U_{T-2} \\ \vdots & \vdots & \vdots & \ddots & \vdots \\ U_T & U_{T-1} & U_{T-2} & \dots & U_1 \end{bmatrix}$$

where $U_i(i = 1, 2...T)$ is a matrix sized by $S \times S$. Let us analyse the elements in this relative small matrix.

We know that every column in X is a transformed $\boldsymbol{x}$. This kind of transformation includes circulation both in horizontal and vertical directions. Let us denote the image which is circulated i times in horizontal direction and j times in vertical direction as $\boldsymbol{x}_{2D}^{(ij)}$. Take an example, $\boldsymbol{x}_{2D}^{(12)}$ is equal to

$$x^{(12)} = \begin{bmatrix} x_{(S-1)T} & x_{(S-1)1} & x_{(S-1)2} & \cdots & x_{(S-1)(T-1)} \\ x_{ST} & x_{S1} & x_{S2} & \cdots & x_{S(T-1)} \\ x_{1T} & x_{11} & x_{12} & \cdots & x_{1(T-1)} \\ \vdots & \vdots & \vdots & \ddots & \vdots \\ x_{(S-2)T} & x_{(S-2)1} & x_{(S-2)2} & \cdots & x_{(S-2)(T-1)} \end{bmatrix}$$

As a result, every element in X^tX is an inner product between two $\boldsymbol{x}^{(ij)}$ (vectorized image $\boldsymbol{x}_{2D}^{(ij)}$). Now we can present every detail of U_i. Here we use $\boldsymbol{x}^{(ij)}$ as the vectorized image.

$$U_i = \begin{bmatrix} \boldsymbol{x}^{(00)}\boldsymbol{x}^{(i0)} & \boldsymbol{x}^{(00)}\boldsymbol{x}^{(i1)} & \dots & \boldsymbol{x}^{(00)}\boldsymbol{x}^{(i(S-1))} \\ \boldsymbol{x}^{(01)}\boldsymbol{x}^{(i0)} & \boldsymbol{x}^{(01)}\boldsymbol{x}^{(i1)} & \dots & \boldsymbol{x}^{(01)}\boldsymbol{x}^{(i(S-1))} \\ \vdots & \vdots & \ddots & \vdots \\ \boldsymbol{x}^{(0(S-1))}\boldsymbol{x}^{(i0)} & \boldsymbol{x}^{(0(S-1))}\boldsymbol{x}^{(i1)} & \dots & \boldsymbol{x}^{(0(-1)S)}\boldsymbol{x}^{(i(S-1))} \end{bmatrix}$$

As we can see, U_i is also a symmetric matrix. Moreover, since $x^{00}x^{ij} = x^{00}x^{i(S-j)}$, there are several elements with the same values even in the same row.

After understanding every detail about the X^tX, now we can try to choose several elements out of the matrix to get the final result of P^tX^tXP. According to the definition of P we mentioned before, the structure of P^tX^tXP can be written as

$$P^T X^T X P = \begin{bmatrix} U'_1 & U'_2 & U'_3 & \dots & U'_t \\ U'_2 & U'_1 & U'_2 & \dots & U'_{t-1} \\ U'_3 & U'_2 & U'_1 & \dots & U'_{t-2} \\ \vdots & \vdots & \vdots & \ddots & \vdots \\ U'_t & U'_{t-1} & U'_{t-2} & \dots & U'_1 \end{bmatrix}$$

where $U'_i \in R^{s \times s}$ is

$$U'_i = \begin{bmatrix} x^{(00)} x^{(i0)} & x^{(00)} x^{(i1)} & \dots & x^{(00)} x^{(i(s-1))} \\ x^{(01)} x^{(i0)} & x^{(01)} x^{(i1)} & \dots & x^{(01)} x^{(i(s-1))} \\ \vdots & \vdots & \ddots & \vdots \\ x^{(0(s-1))} x^{(i0)} & x^{(0(s-1)} x^{(i1)} & \dots & x^{(0(s-1))} x^{(i(s-1))} \end{bmatrix}$$

So an efficient way to solve $P^t X^t X P$ is to compute the $t \times t$ matrix U'_i. Since both $P^t X^t X P$ and U'_i are symmetric, the amount of calculations can be further reduced.

List of publications

International Journal Papers

[J1] Zhouye Chen, Adrian Basarab, and Denis Kouamé, ”Reconstruction of Enhanced Ultrasound Images From Compressed Measurements Using Simultaneous Direction Method of Multipliers,” in *IEEE Transactions on Ultrasonics, Ferroelectrics and Frequency Control*, 2016, accepted.

[J2] Zhouye Chen, Adrian Basarab, and Denis Kouamé, ”Compressive deconvolution in medical ultrasound imaging,” in *IEEE Transactions on Medical Imaging*, Vol. 35 N. 3, p. 728-737, march 2016.

International Conference Papers

[C1] Zhouye Chen, Adrian Basarab, and Denis Kouamé, ”Joint compressive sampling and deconvolution in ultrasound medical imaging,” in *Proc. IEEE International Ultrasonics Symposium (IUS)*, 2015, p. 1-4. (**Best Student Paper Finalist**)

[C2] Zhouye Chen, Adrian Basarab, and Denis Kouamé, ”A simulation study on the choice of regularization parameter in l2-norm ultrasound image restoration,” in *Proc. IEEE Engineering in Medicine and Biology Society Conference (EMBC)*, 2015, p. 6346-6349.

[C3] Zhouye Chen, Ningning Zhao, Adrian Basarab, and Denis Kouamé, ”Ultrasound compressive deconvolution with lp-norm prior ,” in *Proc. European Signal and Image Processing Conference (EUSIPCO)*, 2015, p. 2841-2845.

Bibliography

[Abeyratne 1995] Udantha R Abeyratne, Athina P Petropulu and John M Reid. *Higher order spectra based deconvolution of ultrasound images.* Ultrasonics, Ferroelectrics, and Frequency Control, IEEE Transactions on, vol. 42, no. 6, pages 1064–1075, 1995.

[Achim 2010] Alin Achim, Benjamin Buxton, George Tzagkarakis and Panagiotis Tsakalides. *Compressive sensing for ultrasound RF echoes using a-stable distributions.* In Engineering in Medicine and Biology Society (EMBC), 2010 Annual International Conference of the IEEE, pages 4304–4307. IEEE, 2010.

[Achim 2014] Alin Achim, Adrian Basarab, George Tzagkarakis, Panagiotis Tsakalides and Denis Kouamé. *Reconstruction of compressively sampled ultrasound images using dual prior information.* In Image Processing (ICIP), 2014 IEEE International Conference on, pages 1283–1286. IEEE, 2014.

[Achim 2015] Alin Achim, Adrian Basarab, George Tzagkarakis, Panagiotis Tsakalides and Denis Kouamé. *Reconstruction of ultrasound RF echoes modelled as stable random variables.* IEEE Transactions on Computational Imaging, vol. 1, no. 2, pages 86–95, juin 2015.

[Alessandrini 2011a] M. Alessandrini. *Statistical methods for analysis and processing of medical ultrasound: applications to segmentation and restoration.* PhD thesis, University of Bologna, 2011.

[Alessandrini 2011b] Martino Alessandrini, Simona Maggio, Jonathan Porée, Luca De Marchi, Nicolo Speciale, Emilie Franceschini, Olivier Bernard and Olivier Basset. *A restoration framework for ultrasonic tissue characterization.* Ultrasonics, Ferroelectrics, and Frequency Control, IEEE Transactions on, vol. 58, no. 11, pages 2344–2360, 2011.

[Almeida 2010] Mariana SC Almeida and Luis B Almeida. *Blind and semi-blind deblurring of natural images.* Image Processing, IEEE Transactions on, vol. 19, no. 1, pages 36–52, 2010.

[Amizic 2013] Bruno Amizic, Leonidas Spinoulas, Rafael Molina and Aggelos K Katsaggelos. *Compressive blind image deconvolution.* Image Processing, IEEE Transactions on, vol. 22, no. 10, pages 3994–4006, 2013.

[Babacan 2009] S Derin Babacan, Rafael Molina and Aggelos K Katsaggelos. *Variational Bayesian blind deconvolution using a total variation prior.* Image Processing, IEEE Transactions on, vol. 18, no. 1, pages 12–26, 2009.

[Babacan 2010] S Derin Babacan, Rafael Molina and Aggelos K Katsaggelos. *Bayesian compressive sensing using Laplace priors.* Image Processing, IEEE Transactions on, vol. 19, no. 1, pages 53–63, 2010.

[Baraniuk 2007] Richard Baraniuk and Philippe Steeghs. *Compressive radar imaging.* In 2007 IEEE Radar Conference, pages 128–133. IEEE, 2007.

[Baraniuk 2008] Richard Baraniuk, Mark Davenport, Ronald DeVore and Michael Wakin. *A simple proof of the restricted isometry property for random matrices.* Constructive Approximation, vol. 28, no. 3, pages 253–263, 2008.

[Baraniuk 2011] Richard Baraniuk, Mark A Davenport, Marco F Duarte and Chinmay Hegde. *An introduction to compressive sensing.* Connexions e-textbook, 2011.

[Basarab 2008] Adrian Basarab. *Estimation du mouvement dans des séquences d'images échographiques : application à l'élastographie de la thyroide.* Thèse de doctorat, INSA-Lyon, septembre 2008.

[Basarab 2013] Adrian Basarab, Hervé Liebgott, Olivier Bernard, Denis Friboulet and Denis Kouamé. *Medical ultrasound image reconstruction using distributed compressive sampling.* In 2013 IEEE 10th International Symposium on Biomedical Imaging, pages 628–631. IEEE, 2013.

[Beaton 1974] Albert E Beaton and John W Tukey. *The fitting of power series, meaning polynomials, illustrated on band-spectroscopic data.* Technometrics, vol. 16, no. 2, pages 147–185, 1974.

[Beck 2009a] Amir Beck and Marc Teboulle. *Fast gradient-based algorithms for constrained total variation image denoising and deblurring problems.* Image Processing, IEEE Transactions on, vol. 18, no. 11, pages 2419–2434, 2009.

[Beck 2009b] Amir Beck and Marc Teboulle. *Fast gradient-based algorithms for constrained total variation image denoising and deblurring problems.* Image Processing, IEEE Transactions on, vol. 18, no. 11, pages 2419–2434, 2009.

[Blumensath 2009] Thomas Blumensath and Mike E Davies. *Iterative hard thresholding for compressed sensing.* Applied and Computational Harmonic Analysis, vol. 27, no. 3, pages 265–274, 2009.

[Bolte 2010] Jérôme Bolte, Patrick L Combettes and J-C Pesquet. *Alternating proximal algorithm for blind image recovery.* In Image Processing (ICIP), 2010 17th IEEE International Conference on, pages 1673–1676. IEEE, 2010.

[Bolte 2014] Jérôme Bolte, Shoham Sabach and Marc Teboulle. *Proximal alternating linearized minimization for nonconvex and nonsmooth problems.* Mathematical Programming, vol. 146, no. 1-2, pages 459–494, 2014.

[Boyd 2011] Stephen Boyd, Neal Parikh, Eric Chu, Borja Peleato and Jonathan Eckstein. *Distributed optimization and statistical learning via the alternating direction method of multipliers.* Foundations and Trends® in Machine Learning, vol. 3, no. 1, pages 1–122, 2011.

[Cai 2009] T Tony Cai, Guangwu Xu and Jun Zhang. *On recovery of sparse signals via minimization.* Information Theory, IEEE Transactions on, vol. 55, no. 7, pages 3388–3397, 2009.

[Campisi 2007] Patrizio Campisi and Karen Egiazarian. Blind image deconvolution: theory and applications. CRC press, 2007.

[Candès 2005] Emmanuel J Candès and Terence Tao. *Decoding by linear programming.* Information Theory, IEEE Transactions on, vol. 51, no. 12, pages 4203–4215, 2005.

[Candès 2006a] Emmanuel J Candès, Justin Romberg and Terence Tao. *Robust uncertainty principles: Exact signal reconstruction from highly incomplete frequency information.* Information Theory, IEEE Transactions on, vol. 52, no. 2, pages 489–509, 2006.

[Candès 2006b] Emmanuel J Candès, Justin K Romberg and Terence Tao. *Stable signal recovery from incomplete and inaccurate measurements.* Communications on pure and applied mathematics, vol. 59, no. 8, pages 1207–1223, 2006.

[Candès 2006c] Emmanuel J Candès and Terence Tao. *Near-optimal signal recovery from random projections: Universal encoding strategies?* Information Theory, IEEE Transactions on, vol. 52, no. 12, pages 5406–5425, 2006.

[Candès 2007a] Emmanuel Candès and Justin Romberg. *Sparsity and incoherence in compressive sampling.* Inverse problems, vol. 23, no. 3, page 969, 2007.

[Candès 2007b] Emmanuel J Candès. *ℓ_1-magic.* Technical report, 2007.

[Candès 2008] Emmanuel J Candès and Michael B Wakin. *An introduction to compressive sampling.* Signal Processing Magazine, IEEE, vol. 25, no. 2, pages 21–30, 2008.

[Chambolle 2004] Antonin Chambolle. *An algorithm for total variation minimization and applications.* Journal of Mathematical imaging and vision, vol. 20, no. 1-2, pages 89–97, 2004.

[Chan 1998] Tony F Chan and Chiu-Kwong Wong. *Total variation blind deconvolution.* Image Processing, IEEE Transactions on, vol. 7, no. 3, pages 370–375, 1998.

[Chan 2011] Vincent Chan and Anahi Perlas. Basics of ultrasound imaging, pages 13–19. Springer, 2011.

[Chartrand 2007] Rick Chartrand. *Exact reconstruction of sparse signals via nonconvex minimization.* Signal Processing Letters, IEEE, vol. 14, no. 10, pages 707–710, 2007.

[Chartrand 2008a] Rick Chartrand. *Nonconvex compressive sensing and reconstruction of gradient-sparse images: random vs. tomographic Fourier sampling.* In Image Processing, 2008. ICIP 2008. 15th IEEE International Conference on, pages 2624–2627. IEEE, 2008.

[Chartrand 2008b] Rick Chartrand and Valentina Staneva. *Restricted isometry properties and nonconvex compressive sensing.* Inverse Problems, vol. 24, no. 3, page 035020, 2008.

[Chartrand 2008c] Rick Chartrand and Wotao Yin. *Iteratively reweighted algorithms for compressive sensing.* In Acoustics, speech and signal processing, 2008. ICASSP 2008. IEEE international conference on, pages 3869–3872. IEEE, 2008.

[Chen 2001] Scott Shaobing Chen, David L Donoho and Michael A Saunders. *Atomic decomposition by basis pursuit.* SIAM review, vol. 43, no. 1, pages 129–159, 2001.

[Chen 2015a] Z Chen, N Zhao, A Basarab and D Kouamé. *Ultrasound compressive deconvolution with lp-norm prior (regular paper).* In European Signal and Image Processing Conference (EUSIPCO), Nice, France, volume 31, pages 2841–2845, 2015.

[Chen 2015b] Zhouye Chen, Adrian Basarab and Denis Kouamé. *Joint compressive sampling and deconvolution in ultrasound medical imaging.* In Ultrasonics Symposium (IUS), 2015 IEEE International, pages 1–4. IEEE, 2015.

[Chen 2015c] Zhouye Chen, Adrian Basarab and Denis Kouame. *A simulation study on the choice of regularization parameter in ℓ_2-norm ultrasound image restoration.* In Engineering in Medicine and Biology Society (EMBC), 2015 37th Annual International Conference of the IEEE, pages 6346–6349. IEEE, 2015.

[Chen 2016a] Zhouye Chen, Adrian Basarab and Denis Kouamé. *Compressive deconvolution in medical ultrasound imaging.* IEEE transactions on medical imaging, vol. 35, no. 3, pages 728–737, 2016.

[Chen 2016b] Zhouye Chen, Adrian Basarab and Denis Kouamé. *Reconstruction of Enhanced Ultrasound Images From Compressed Measurements Using Simultaneous Direction Method of Multipliers.* IEEE Transactions on Ultrasonics, Ferroelectrics and Frequency Control, 2016.

[Chernyakova 2014] Tanya Chernyakova and Yonina Eldar. *Fourier-domain beamforming: the path to compressed ultrasound imaging.* Ultrasonics, Ferroelectrics, and Frequency Control, IEEE Transactions on, vol. 61, no. 8, pages 1252–1267, 2014.

[Chouzenoux 2013] Emilie Chouzenoux, Jean-Christophe Pesquet and Audrey Repetti. *A block coordinate variable metric forward–backward algorithm.* Journal of Global Optimization, pages 1–29, 2013.

[Chouzenoux 2014] Emilie Chouzenoux, Jean-Christophe Pesquet and Audrey Repetti. *Variable metric forward–backward algorithm for minimizing the sum of a differentiable function and a convex function.* Journal of Optimization Theory and Applications, vol. 162, no. 1, pages 107–132, 2014.

[Chuo 2013] Yen Chuo, Tsung-Han Chan and Meng-Lin Li. *Ultrasound compressed sensing: Performance study of reconstruction on different ultrasound imaging data.* In Ultrasonics Symposium (IUS), 2013 IEEE International, pages 903–905. IEEE, 2013.

[Cohen 2009] Albert Cohen, Wolfgang Dahmen and Ronald DeVore. *Compressed sensing and best k-term approximation.* Journal of the American mathematical society, vol. 22, no. 1, pages 211–231, 2009.

[Coifman 2001] Ronald Coifman, F Geshwind and Yves Meyer. *Noiselets.* Applied and Computational Harmonic Analysis, vol. 10, no. 1, pages 27–44, 2001.

[Combettes 2005] Patrick L Combettes and Valérie R Wajs. *Signal recovery by proximal forward-backward splitting.* Multiscale Modeling & Simulation, vol. 4, no. 4, pages 1168–1200, 2005.

[Combettes 2007] Patrick L Combettes and Jean-Christophe Pesquet. *Proximal thresholding algorithm for minimization over orthonormal bases.* SIAM Journal on Optimization, vol. 18, no. 4, pages 1351–1376, 2007.

[Combettes 2011] Patrick L Combettes and Jean-Christophe Pesquet. *Proximal splitting methods in signal processing.* In Fixed-point algorithms for inverse problems in science and engineering, pages 185–212. Springer, 2011.

[Daubechies 2004] Ingrid Daubechies, Michel Defrise and Christine De Mol. *An iterative thresholding algorithm for linear inverse problems with a sparsity constraint.* Communications on pure and applied mathematics, vol. 57, no. 11, pages 1413–1457, 2004.

[Daubechies 2010] Ingrid Daubechies, Ronald DeVore, Massimo Fornasier and C Sinan Güntürk. *Iteratively reweighted least squares minimization for sparse recovery.* Communications on Pure and Applied Mathematics, vol. 63, no. 1, pages 1–38, 2010.

[Deng 2013] Wei Deng, Wotao Yin and Yin Zhang. *Group sparse optimization by alternating direction method.* In SPIE Optical Engineering+ Applications, pages 88580R–88580R. International Society for Optics and Photonics, 2013.

[Diarra 2013] Bakary Diarra, Marc Robini, Piero Tortoli, Christian Cachard and Hervé Liebgott. *Design of optimal 2-D nongrid sparse arrays for medical ultrasound.* IEEE Transactions on Biomedical Engineering, vol. 60, no. 11, pages 3093–3102, 2013.

[Do 2012] Thong T Do, Lu Gan, Nam H Nguyen and Trac D Tran. *Fast and efficient compressive sensing using structurally random matrices.* Signal Processing, IEEE Transactions on, vol. 60, no. 1, pages 139–154, 2012.

[Dobigeon 2012] Nicolas Dobigeon, Adrian Basarab, Denis Kouamé and Jean-Yves Tourneret. *Regularized Bayesian compressed sensing in ultrasound imaging (regular paper).* In European Signal and Image Processing Conference (EUSIPCO), Bucharest, Romania, 27/08/2012-31/08/2012, pages 2600–2604, http://www.eurasip.org/, août 2012. EURASIP.

[Donoho 2001] David L Donoho and Xiaoming Huo. *Uncertainty principles and ideal atomic decomposition.* Information Theory, IEEE Transactions on, vol. 47, no. 7, pages 2845–2862, 2001.

[Donoho 2006] David L Donoho. *Compressed sensing.* Information Theory, IEEE Transactions on, vol. 52, no. 4, pages 1289–1306, 2006.

[Donoho 2009] David L Donoho, Arian Maleki and Andrea Montanari. *Message-passing algorithms for compressed sensing.* Proceedings of the National Academy of Sciences, vol. 106, no. 45, pages 18914–18919, 2009.

[Donoho 2012] David L Donoho, Yaakov Tsaig, Iddo Drori and Jean-Luc Starck. *Sparse solution of underdetermined systems of linear equations by stagewise orthogonal matching pursuit.* Information Theory, IEEE Transactions on, vol. 58, no. 2, pages 1094–1121, 2012.

[Duarte-Carvajalino 2008] Julio M Duarte-Carvajalino and Guillermo Sapiro. *Learning to sense sparse signals: Simultaneous sensing matrix and sparsifying dictionary optimization.* Technical report, DTIC Document, 2008.

[Eckstein 1994] Jonathan Eckstein and Masao Fukushima. *Some reformulations and applications of the alternating direction method of multipliers.* In Large scale optimization, pages 115–134. Springer, 1994.

[Edler 2004] Inge Edler and Kjell Lindström. *The history of echocardiography.* Ultrasound in Medicine & Biology, vol. 30, no. 12, pages 1565 – 1644, 2004.

[Eldar 2009] Yonina C Eldar. *Generalized SURE for exponential families: Applications to regularization.* Signal Processing, IEEE Transactions on, vol. 57, no. 2, pages 471–481, 2009.

[Eldar 2012] Yonina C Eldar and Gitta Kutyniok. Compressed sensing: theory and applications. Cambridge University Press, 2012.

[Esser 2009] Ernie Esser. *Applications of Lagrangian-based alternating direction methods and connections to split Bregman.* CAM report, vol. 9, page 31, 2009.

[Fatemi 1980] Mostafa Fatemi and Avinash C Kak. *Ultrasonic B-scan imaging: Theory of image formation and a technique for restoration.* Ultrasonic Imaging, vol. 2, no. 1, pages 1–47, 1980.

[Figueiredo 2007] Mário AT Figueiredo, Robert D Nowak and Stephen J Wright. *Gradient projection for sparse reconstruction: Application to compressed sensing and other inverse problems.* Selected Topics in Signal Processing, IEEE Journal of, vol. 1, no. 4, pages 586–597, 2007.

[Flandrin 2004] Patrick Flandrin, Gabriel Rilling and Paulo Goncalves. *Empirical mode decomposition as a filter bank.* Signal Processing Letters, IEEE, vol. 11, no. 2, pages 112–114, 2004.

[Fortin 2000] Michel Fortin and Roland Glowinski. Augmented lagrangian methods: applications to the numerical solution of boundary-value problems, volume 15. Elsevier, 2000.

[Friboulet 2010] D Friboulet, H Liebgott and R Prost. *Compressive sensing for raw RF signals reconstruction in ultrasound.* In Ultrasonics Symposium (IUS), 2010 IEEE, pages 367–370. IEEE, 2010.

[Fukushima 1992] Masao Fukushima. *Application of the alternating direction method of multipliers to separable convex programming problems.* Computational Optimization and Applications, vol. 1, no. 1, pages 93–111, 1992.

[Gabay 1976] Daniel Gabay and Bertrand Mercier. *A dual algorithm for the solution of nonlinear variational problems via finite element approximation.* Computers & Mathematics with Applications, vol. 2, no. 1, pages 17–40, 1976.

[Galatsanos 1992] Nikolas P Galatsanos and Aggelos K Katsaggelos. *Methods for choosing the regularization parameter and estimating the noise variance in image restoration and their relation.* Image Processing, IEEE Transactions on, vol. 1, no. 3, pages 322–336, 1992.

[Gedalyahu 2011] Kfir Gedalyahu, Ronen Tur and Yonina C Eldar. *Multichannel sampling of pulse streams at the rate of innovation.* Signal Processing, IEEE Transactions on, vol. 59, no. 4, pages 1491–1504, 2011.

[Goldstein 2009] Tom Goldstein and Stanley Osher. *The split Bregman method for L1-regularized problems.* SIAM Journal on Imaging Sciences, vol. 2, no. 2, pages 323–343, 2009.

[Golub 1979] Gene H Golub, Michael Heath and Grace Wahba. *Generalized cross-validation as a method for choosing a good ridge parameter.* Technometrics, vol. 21, no. 2, pages 215–223, 1979.

[Hale 2007] Elaine T Hale, Wotao Yin and Yin Zhang. *A fixed-point continuation method for l1-regularized minimization with applications to compressed sensing.* CAAM TR07-07, Rice University, vol. 43, page 44, 2007.

[Hall 1987] Peter Hall and DM Titterington. *Common structure of techniques for choosing smoothing parameters in regression problems.* Journal of the Royal Statistical Society. Series B (Methodological), pages 184–198, 1987.

[He 2002] Bingsheng He, Li-Zhi Liao, Deren Han and Hai Yang. *A new inexact alternating directions method for monotone variational inequalities.* Mathematical Programming, vol. 92, no. 1, pages 103–118, 2002.

[Hegde 2009] Chinmay Hegde and Richard G Baraniuk. *Compressive sensing of streams of pulses.* In Communication, Control, and Computing, 2009. Allerton 2009. 47th Annual Allerton Conference on, pages 44–51. IEEE, 2009.

[Hegde 2011] Chinmay Hegde and Richard G Baraniuk. *Sampling and recovery of pulse streams.* Signal Processing, IEEE Transactions on, vol. 59, no. 4, pages 1505–1517, 2011.

[Hunt 1973] B R_ Hunt. *The application of constrained least squares estimation to image restoration by digital computer.* Computers, IEEE Transactions on, vol. 100, no. 9, pages 805–812, 1973.

[Jensen 1991] Jørgen Arendt Jensen. *A model for the propagation and scattering of ultrasound in tissue.* Acoustical Society of America. Journal, vol. 89, no. 1, pages 182–190, 1991.

[Jensen 1992] Jørgen Arendt Jensen. *Deconvolution of ultrasound images.* Ultrasonic imaging, vol. 14, no. 1, pages 1–15, 1992.

[Jensen 1993] Jørgen Arendt Jensen, Jan Mathorne, Torben Gravesen and Bjarne Stage. *Deconvolution of in vivo ultrasound B-mode images.* Ultrasonic Imaging, vol. 15, no. 2, pages 122–133, 1993.

[Jensen 1994a] Jørgen Arendt Jensen. *Estimation of in vivo pulses in medical ultrasound.* Ultrasonic imaging, vol. 16, no. 3, pages 190–203, 1994.

[Jensen 1994b] Jorgen Arendt Jensen and Sidney Leeman. *Nonparametric estimation of ultrasound pulses.* Biomedical Engineering, IEEE Transactions on, vol. 41, no. 10, pages 929–936, 1994.

[Jensen 1996] Jørgen Arendt Jensen. *Field: A program for simulating ultrasound systems.* In 10TH NORDICBALTIC CONFERENCE ON BIOMEDICAL IMAGING, VOL. 4, SUPPLEMENT 1, PART 1: 351–353. Citeseer, 1996.

[Jensen 2006] Jørgen Arendt Jensen, Svetoslav Ivanov Nikolov, Kim Løkke Gammelmark and Morten Høgholm Pedersen. *Synthetic aperture ultrasound imaging.* Ultrasonics, vol. 44, pages e5–e15, 2006.

[Ji 2008] Shihao Ji, Ya Xue and Lawrence Carin. *Bayesian compressive sensing.* Signal Processing, IEEE Transactions on, vol. 56, no. 6, pages 2346–2356, 2008.

[Jiřík 2006] Radovan Jiřík and Torfinn Taxt. *High-resolution ultrasonic imaging using two-dimensional homomorphic filtering.* Ultrasonics, Ferroelectrics, and Frequency Control, IEEE Transactions on, vol. 53, no. 8, pages 1440–1448, 2006.

[Jirik 2008] Radovan Jirik and Torfinn Taxt. *Two-dimensional blind Bayesian deconvolution of medical ultrasound images.* Ultrasonics, Ferroelectrics, and Frequency Control, IEEE Transactions on, vol. 55, no. 10, pages 2140–2153, 2008.

[Kim 2007] Seung-Jean Kim, Kwangmoo Koh, Michael Lustig, Stephen Boyd and Dimitry Gorinevsky. *An interior-point method for large-scale ℓ_1-regularized least squares.* Selected Topics in Signal Processing, IEEE Journal of, vol. 1, no. 4, pages 606–617, 2007.

[Kontogiorgis 1998] Spyridon Kontogiorgis and Robert R Meyer. *A variable-penalty alternating directions method for convex optimization.* Mathematical Programming, vol. 83, no. 1-3, pages 29–53, 1998.

[Kouamé 2015] Denis Kouamé. Ultrasound imaging: Systems, signals and image processing. 2015.

[Lawson 1961] C.L. Lawson. *Contributions to the theory of linear least maximum approximations.* PhD thesis, UCLA, 1961.

[Liebgott 2012] Hervé Liebgott, Adrian Basarab, Denis Kouame, Olivier Bernard and Denis Friboulet. *Compressive sensing in medical ultrasound.* In 2012 IEEE International Ultrasonics Symposium, pages 1–6. IEEE, 2012.

[Liebgott 2013] Hervé Liebgott, Rémy Prost and Denis Friboulet. *Pre-beamformed RF signal reconstruction in medical ultrasound using compressive sensing.* Ultrasonics, vol. 53, no. 2, pages 525–533, 2013.

[Liu 1983] CN Liu, Mostafa Fatemi and RC Waag. *Digital processing for improvement of ultrasonic abdominal images.* Medical Imaging, IEEE Transactions on, vol. 2, no. 2, pages 66–75, 1983.

[Lorintiu 2014] Oana Lorintiu, Hervé Liebgott, Martino Alessandrini, Olivier Bernard and Denis Friboulet. *Compressed sensing reconstruction of 3d ultrasound data using dictionary learning.* In Image Processing (ICIP), 2014 IEEE International Conference on, pages 1317–1321. IEEE, 2014.

[Lorintiu 2015a] O. Lorintiu. *Compressed sensing reconstruction for 3D and Doppler medical ultrasound.* PhD thesis, INSA-Lyon, Lyon, 2015. Jury: M. Davies(rapporteur), D. Friboulet (directeur), D. Kouamé (rapporteur), H. Liebgott (co-directeur), J.-P. Thiran (président).

[Lorintiu 2015b] Oana Lorintiu, Hervé Liebgott, Martino Alessandrini, Olivier Bernard and Denis Friboulet. *Compressed sensing reconstruction of 3D ultrasound data using dictionary learning and line-wise subsampling.* Medical Imaging, IEEE Transactions on, vol. 34, no. 12, pages 2467–2477, 2015.

[Lyshchik 2005] A Lyshchik, T Higashi, R Asato, S Tanaka, J Ito, M Hiraoka, AB Brill, Tsuneo Saga and K Togashi. *Elastic moduli of thyroid tissues under compression.* Ultrasonic imaging, vol. 27, no. 2, pages 101–110, 2005.

[Ma 2009] Jianwei Ma and Francois-Xavier Le Dimet. *Deblurring from highly incomplete measurements for remote sensing.* Geoscience and Remote Sensing, IEEE Transactions on, vol. 47, no. 3, pages 792–802, 2009.

[Mallat 1993] Stéphane G Mallat and Zhifeng Zhang. *Matching pursuits with time-frequency dictionaries.* Signal Processing, IEEE Transactions on, vol. 41, no. 12, pages 3397–3415, 1993.

[Mallat 1999] Stéphane Mallat. A wavelet tour of signal processing. Academic press, 1999.

[Mendelson 2008] Shahar Mendelson, Alain Pajor and Nicole Tomczak-Jaegermann. *Uniform uncertainty principle for Bernoulli and subgaussian ensembles.* Constructive Approximation, vol. 28, no. 3, pages 277–289, 2008.

[Michailovich 2003] Oleg Michailovich and Dan Adam. *Robust estimation of ultrasound pulses using outlier-resistant de-noising.* Medical Imaging, IEEE Transactions on, vol. 22, no. 3, pages 368–381, 2003.

[Michailovich 2004] Oleg Michailovich and Dan Adam. *Phase unwrapping for 2-D blind deconvolution of ultrasound images.* Medical Imaging, IEEE Transactions on, vol. 23, no. 1, pages 7–25, 2004.

[Michailovich 2005] Oleg V Michailovich and Dan Adam. *A novel approach to the 2-D blind deconvolution problem in medical ultrasound.* Medical Imaging, IEEE Transactions on, vol. 24, no. 1, pages 86–104, 2005.

[Michailovich 2007] Oleg Michailovich and Allen Tannenbaum. *Blind deconvolution of medical ultrasound images: a parametric inverse filtering approach.* Image Processing, IEEE Transactions on, vol. 16, no. 12, pages 3005–3019, 2007.

[Mishali 2011] Moshe Mishali, Yonina C Eldar, Oleg Dounaevsky and Eli Shoshan. *Xampling: Analog to digital at sub-Nyquist rates.* Circuits, Devices & Systems, IET, vol. 5, no. 1, pages 8–20, 2011.

[Molina 2006] Rafael Molina, Javier Mateos and Aggelos K Katsaggelos. *Blind deconvolution using a variational approach to parameter, image, and blur estimation.* Image Processing, IEEE Transactions on, vol. 15, no. 12, pages 3715–3727, 2006.

[Morin 2012] Renaud Morin, Adrian Basarab and Denis Kouamé. *Alternating direction method of multipliers framework for super-resolution in ultrasound imaging.* In Biomedical Imaging (ISBI), 2012 9th IEEE International Symposium on, pages 1595–1598. IEEE, 2012.

[Morin 2013a] Renaud Morin. *Amélioration de la résolution en imagerie ultrasonore.* Thèse de doctorat, Université de Toulouse, Toulouse, France, novembre 2013. (Soutenance le 29/11/2013).

[Morin 2013b] Renaud Morin, Stéphanie Bidon, Adrian Basarab and Denis Kouamé. *Semi-blind deconvolution for resolution enhancement in ultrasound imaging.* In Image Processing (ICIP), 2013 20th IEEE International Conference on, pages 1413–1417. IEEE, 2013.

[Naidu 2015] R Ramu Naidu, Phanindra Jampana and CS Sastry. *Deterministic compressed sensing matrices: Construction via Euler Squares and applications.* IEEE Transactions on Signal Processing, vol. 64, no. 14, pages 3566–3575, 2015.

[Needell 2009a] Deanna Needell and Joel A Tropp. *CoSaMP: Iterative signal recovery from incomplete and inaccurate samples.* Applied and Computational Harmonic Analysis, vol. 26, no. 3, pages 301–321, 2009.

[Needell 2009b] Deanna Needell and Roman Vershynin. *Uniform uncertainty principle and signal recovery via regularized orthogonal matching pursuit.* Foundations of computational mathematics, vol. 9, no. 3, pages 317–334, 2009.

[Needell 2010] Deanna Needell and Roman Vershynin. *Signal recovery from incomplete and inaccurate measurements via regularized orthogonal matching pursuit.* Selected Topics in Signal Processing, IEEE Journal of, vol. 4, no. 2, pages 310–316, 2010.

[Ng 2007a] James Ng, Richard Prager, Nick Kingsbury, Graham Treece and Andrew Gee. *Wavelet restoration of medical pulse-echo ultrasound images in an EM framework.* IEEE Transactions on Ultrasonics Ferroelectrics and Frequency Control, vol. 54, no. 3, page 550, 2007.

[Ng 2007b] James Kee Huat Ng. *Restoration of medical pulse-echo ultrasound images.* PhD thesis, Citeseer, 2007.

[Ng 2010] Michael K Ng, Pierre Weiss and Xiaoming Yuan. *Solving constrained total-variation image restoration and reconstruction problems via alternating direction methods.* SIAM journal on Scientific Computing, vol. 32, no. 5, pages 2710–2736, 2010.

[Pati 1993] Yagyensh Chandra Pati, Ramin Rezaiifar and PS Krishnaprasad. *Orthogonal matching pursuit: Recursive function approximation with applications to wavelet decomposition.* In Signals, Systems and Computers, 1993. 1993 Conference Record of The Twenty-Seventh Asilomar Conference on, pages 40–44. IEEE, 1993.

[Pesquet 2012] Jean-Christophe Pesquet and Nelly Pustelnik. *A parallel inertial proximal optimization method.* Pacific Journal of Optimization, vol. 8, no. 2, pages 273–305, 2012.

[Prince 2006] Jerry L Prince and Jonathan M Links. Medical imaging signals and systems. Pearson Prentice Hall Upper Saddle River, NJ, 2006.

[Pustelnik 2011] Nelly Pustelnik, Caroline Chaux and Jean-Christophe Pesquet. *Parallel proximal algorithm for image restoration using hybrid regularization.* Image Processing, IEEE Transactions on, vol. 20, no. 9, pages 2450–2462, 2011.

[Pustelnik 2012] Nelly Pustelnik, Jean-Christophe Pesquet and Caroline Chaux. *Relaxing tight frame condition in parallel proximal methods for signal restoration.* Signal Processing, IEEE Transactions on, vol. 60, no. 2, pages 968–973, 2012.

[Quinsac 2010a] Céline Quinsac, Adrian Basarab, Jean-Marc Girault and Denis Kouamé. *Compressed sensing of ultrasound images: sampling of spatial and frequency domains (regular paper).* In IEEE Workshop on Signal Processing Systems, San Francisco, 06/10/2010-08/10/2010, pages 231–236, http://www.ieee.org/, octobre 2010. IEEE.

[Quinsac 2010b] Céline Quinsac, Adrian Basarab, Jean-Marc Gregoire and Denis Kouamé. *3D compressed sensing ultrasound imaging (regular paper).* In IEEE International Ultrasonic Symposium, San Diego, 11/10/2010-14/10/2010, pages 363–366, http://www.ieee.org/, octobre 2010. IEEE.

[Quinsac 2012] Céline Quinsac, Adrian Basarab and Denis Kouamé. *Frequency domain compressive sampling for ultrasound imaging.* Advances in Acoustics and Vibration, Advances in Acoustic Sensing, Imaging, and Signal Processing, vol. 12, pages 1–16, 2012.

[Raguet 2013] Hugo Raguet, Jalal Fadili and Gabriel Peyré. *A generalized forward-backward splitting.* SIAM Journal on Imaging Sciences, vol. 6, no. 3, pages 1199–1226, 2013.

[Rao 1999] Bhaskar D Rao and Kenneth Kreutz-Delgado. *An affine scaling methodology for best basis selection.* Signal Processing, IEEE Transactions on, vol. 47, no. 1, pages 187–200, 1999.

[Rasmussen 1994] Klaus Bolding Rasmussen. *Maximum likelihood estimation of the attenuated ultrasound pulse.* Signal Processing, IEEE Transactions on, vol. 42, no. 1, pages 220–222, 1994.

[Repetti 2015] Audrey Repetti, Mai Quyen Pham, Laurent Duval, Emilie Chouzenoux and J-C Pesquet. *Euclid in a Taxicab: Sparse Blind Deconvolution with Smoothed Regularization.* Signal Processing Letters, IEEE, vol. 22, no. 5, pages 539–543, 2015.

[Robinson 1984] DE Robinson and M Wing. *Lateral deconvolution of ultrasonic beams.* Ultrasonic imaging, vol. 6, no. 1, pages 1–12, 1984.

[Schiffner 2011] Martin F Schiffner and Georg Schmitz. *Fast pulse-echo ultrasound imaging employing compressive sensing.* In Ultrasonics Symposium (IUS), 2011 IEEE International, pages 688–691. IEEE, 2011.

[Schiffner 2012] MF Schiffner, T Jansen and G Schmitz. *Compressed sensing for fast image acquisition in pulse-echo ultrasound.* Biomedical Engineering/Biomedizinische Technik, vol. 57, no. SI-1 Track-B, pages 192–195, 2012.

[Schniter 2008] Philip Schniter, Lee C Potter and Justin Ziniel. *Fast Bayesian matching pursuit.* In Information Theory and Applications Workshop, 2008, pages 326–333. IEEE, 2008.

[Setzer 2010] Simon Setzer, Gabriele Steidl and Tanja Teuber. *Deblurring Poissonian images by split Bregman techniques.* Journal of Visual Communication and Image Representation, vol. 21, no. 3, pages 193–199, 2010.

[Spinoulas 2012] Leonidas Spinoulas, Bruno Amizic, Miguel Vega, Rafael Molina and Aggelos K Katsaggelos. *Simultaneous bayesian compressive sensing and blind deconvolution.* In Signal Processing Conference (EUSIPCO), 2012 Proceedings of the 20th European, pages 1414–1418. IEEE, 2012.

[Szabo 2004] Thomas L Szabo. Diagnostic ultrasound imaging: inside out. Academic Press, 2004.

[Tanter 2014] Mickael Tanter and Mathias Fink. *Ultrafast imaging in biomedical ultrasound.* Ultrasonics, Ferroelectrics, and Frequency Control, IEEE Transactions on, vol. 61, no. 1, pages 102–119, 2014.

[Taxt 1995] Torfinn Taxt. *Restoration of medical ultrasound images using two-dimensional homomorphic deconvolution.* Ultrasonics, Ferroelectrics, and Frequency Control, IEEE Transactions on, vol. 42, no. 4, pages 543–554, 1995.

[Taxt 1997] Torfinn Taxt. *Comparison of cepstrum-based methods for radial blind deconvolution of ultrasound images.* Ultrasonics, Ferroelectrics, and Frequency Control, IEEE Transactions on, vol. 44, no. 3, pages 666–674, 1997.

[Taxt 2001a] Torfinn Taxt. *Three-dimensional blind deconvolution of ultrasound images.* Ultrasonics, Ferroelectrics, and Frequency Control, IEEE Transactions on, vol. 48, no. 4, pages 867–871, 2001.

[Taxt 2001b] Torfinn Taxt and Jarle Strand. *Two-dimensional noise-robust blind deconvolution of ultrasound images.* Ultrasonics, Ferroelectrics, and Frequency Control, IEEE Transactions on, vol. 48, no. 4, pages 861–866, 2001.

[Tipping 2001] Michael E Tipping. *Sparse Bayesian learning and the relevance vector machine.* The journal of machine learning research, vol. 1, pages 211–244, 2001.

[Tropp 2007] Joel A Tropp and Anna C Gilbert. *Signal recovery from random measurements via orthogonal matching pursuit.* Information Theory, IEEE Transactions on, vol. 53, no. 12, pages 4655–4666, 2007.

[Tur 2011] Ronen Tur, Yonina C Eldar and Zvi Friedman. *Innovation rate sampling of pulse streams with application to ultrasound imaging.* Signal Processing, IEEE Transactions on, vol. 59, no. 4, pages 1827–1842, 2011.

[Van Den Berg 2008] Ewout Van Den Berg and Michael P Friedlander. *Probing the Pareto frontier for basis pursuit solutions.* SIAM Journal on Scientific Computing, vol. 31, no. 2, pages 890–912, 2008.

[Wagner 2012] Noam Wagner, Yonina C Eldar and Zvi Friedman. *Compressed beamforming in ultrasound imaging.* Signal Processing, IEEE Transactions on, vol. 60, no. 9, pages 4643–4657, 2012.

[Wahba 1983] Grace Wahba. *Bayesian "confidence intervals" for the cross-validated smoothing spline.* Journal of the Royal Statistical Society. Series B (Methodological), pages 133–150, 1983.

[Wang 2004] Zhou Wang, Alan Conrad Bovik, Hamid Rahim Sheikh and Eero P Simoncelli. *Image quality assessment: from error visibility to structural similarity.* Image Processing, IEEE Transactions on, vol. 13, no. 4, pages 600–612, 2004.

[Wang 2008] Yilun Wang, Junfeng Yang, Wotao Yin and Yin Zhang. *A new alternating minimization algorithm for total variation image reconstruction.* SIAM Journal on Imaging Sciences, vol. 1, no. 3, pages 248–272, 2008.

[Wipf 2004] David P Wipf and Bhaskar D Rao. *Sparse Bayesian learning for basis selection.* Signal Processing, IEEE Transactions on, vol. 52, no. 8, pages 2153–2164, 2004.

[Wipf 2007] David P Wipf and Bhaskar D Rao. *An empirical Bayesian strategy for solving the simultaneous sparse approximation problem.* Signal Processing, IEEE Transactions on, vol. 55, no. 7, pages 3704–3716, 2007.

[Xiao 2011] Liang Xiao, Jun Shao, Lili Huang and Zhihui Wei. *Compounded regularization and fast algorithm for compressive sensing deconvolution.* In Image and Graphics (ICIG), 2011 Sixth International Conference on, pages 616–621. IEEE, 2011.

[Yang 2011] Junfeng Yang and Yin Zhang. *Alternating direction algorithms for ℓ_1-problems in compressive sensing.* SIAM journal on scientific computing, vol. 33, no. 1, pages 250–278, 2011.

[Yin 2008] Wotao Yin, Stanley Osher, Donald Goldfarb and Jerome Darbon. *Bregman iterative algorithms for ℓ_1-minimization with applications to compressed sensing.* SIAM Journal on Imaging Sciences, vol. 1, no. 1, pages 143–168, 2008.

[Yu 2012] Chengpu Yu, Cishen Zhang and Lihua Xie. *A blind deconvolution approach to ultrasound imaging.* Ultrasonics, Ferroelectrics, and Frequency Control, IEEE Transactions on, vol. 59, no. 2, pages 271–280, 2012.

[Zayyani 2009] Hadi Zayyani, Massoud Babaie-Zadeh and Christian Jutten. *Bayesian pursuit algorithm for sparse representation.* In Acoustics, Speech and Signal Processing, 2009. ICASSP 2009. IEEE International Conference on, pages 1549–1552. IEEE, 2009.

[Zhao 2010] Manqi Zhao and Venkatesh Saligrama. *On compressed blind de-convolution of filtered sparse processes.* In Acoustics Speech and Signal Processing (ICASSP), 2010 IEEE International Conference on, pages 4038–4041. IEEE, 2010.

[Zhao 2014] Ningning Zhao, Adrian Basarab, Denis Kouamé and Jean-Yves Tourneret. *Restoration of Ultrasound Images Using A Hierarchical Bayesian Model with A Generalized Gaussian Prior (regular paper).* In IEEE International Conference on Image Processing (ICIP), Paris, France, 27/10/2014-30/10/2014, pages 4577–4581, http://www.ieee.org/, octobre 2014. IEEE.

[Zhao 2015] Ningning Zhao, Adrian Basarab, Denis Kouame and Jean-Yves Tourneret. *Joint Bayesian deconvolution and pointspread function estimation for ultrasound imaging.* In Biomedical Imaging (ISBI), 2015 IEEE 12th International Symposium on, pages 235–238. IEEE, 2015.

[Zhao 2016] Ningning Zhao, Adrian Basarab, Denis Kouamé and Jean-Yves Tourneret. *Joint Segmentation and Deconvolution of Ultrasound Images Using a Hierarchical Bayesian Model based on Generalized Gaussian Priors.* IEEE Transactions on Image Processing, 2016.